TUM School of Engineering and Design

Technische Universität München

Heat Transfer Predictions in Hydrogen/Oxygen and Methane/Oxygen Rocket Engines

Christof Roth

Acknowledgments

Abstract

Recent research and development efforts in rocket engine design have been focused on methane/oxygen as propellants due to their many advantages, e.g. performance, cooling properties, and low toxicity. The Chair of Space Propulsion (Professur für Raumfahrtantriebe) at the Technical University of Munich (TUM) operates an experimental rocket combustor facility to improve the fundamental knowledge of the physical phenomena using this propellant combination. The present work contributes to the advancement of the numerical predictions of the flow, combustion, and heat transfer in methane/oxygen and hydrogen/oxygen rocket engines using data available from this test facility. A computational model based on CFD is developed for a lab-scale single-element rocket combustor. The goal of this effort is the prediction of performance and heat transfer characteristics in the test setup. To this end, several model extensions are developed to deal with the different requirements identified for the two propellant combinations. A focus herein are the recombination reactions in the strongly cooled wall boundary layer seen in detailed chemistry simulations with finite rate reactions.

Zusammenfassung

Die Forschung und Entwicklung im Bereich der Flüssigkeitsraketenantriebe fokussierte sich in den letzten Jahren aufgrund diverser Vorteile wie beispielsweise hoher Leistungsfähigkeit, guter Kühlungseigenschaften und geringer Toxizität auf die Treibstoffkombination Methan und Sauerstoff. Die Professur für Raumfahrtantriebe der Technischen Univerität München betreibt einen experimentellen Raketenprüfstand zur Untersuchung der dominierenden physikalischen Phänomene dieser Treibstoffkombination. In der vorliegenden Arbeit werden numerische Methoden zur Vorhersage von Strömung, Verbrennung und Wärmeübergang in Raketenantrieben weiterentwickelt. Diese werden an Hand von Testdaten für Methan und Sauerstoff sowie Wasserstoff und Sauerstoff validiert, welche am oben genannten Prüfstand generiert wurden. Es wird ein Berechnungsmodell für eine Raketenbrennkammer mit einem einzelnen Einspritzelement entwickelt. Dieses basiert auf CFD Methoden. Ziel ist die Vorhersage von Leistung und Wärmeübergangscharakteristika. Dafür werden mehrere Modellerweiterungen implementiert, welche die identifizierten Anforderungen für beide Treibstoffkombinationen berücksichtigen. Der Fokus liegt auf der Modellierung der Rekombinationreaktionen in der stark gekühlten wandnahen Strömung, sichtbar in Simulationen mit detaillierter Chemiemodellierung.

Contents

List of Figures

List of Tables

Nomenclature

Symbols

A Area

c Species Concentration

c^* Characteristic Velocity

c_e Effective Exhaust Velocity

c_F Thrust Coefficient

c_p Specific Heat Capacity

D_Y Species Diffusion Coefficient

D_Z Mixture Fraction Diffusion Coefficient

Da Damköhler Number

E_a Activation Energy

e Total Energy

F Thrust

g_0 Standard Gravity Acceleration

H Enthalpy

h Specific Enthalpy

I_{sp} Specific Impulse

k Turbulent Kinetic Energy

$k_{f,b}$ Forward/Backward Rate Constant

l Length

l^* Characteristic Length

Le Lewis Number

$\dot{m}$ Mass Flow Rate

M_w Molecular Weight

O/F Oxidizer to Fuel Ratio

p Pressure

Pr Prandtl Number

R_m Universal Gas Constant

Re Reynolds Number

S Source Term/Mean Rate-of-Strain

s Specific Entropy

Sc Schmidt Number

T Temperature

t Time

U Unmixedness

u Flow Velocity

Q Heat Load

q Wall Heat Flux

V Volume

v Velocity

Y Species Mass Fraction

Z Mixture Fraction

Greek Symbols

δ_{ij} Kronecker Delta

ε Expansion Ratio/Turbulent Kinetic Energy Dissipation

ε_c Contraction Ratio

η_{c^*} Combustion Efficiency

κ Isentropic Exponent

Λ Normalized Variable

λ Thermal Conductivity

μ Dynamic Viscosity

ν Stoichiometric Coefficient

ρ Density

τ_{ij} Viscous Stress Tensor

ϕ Scalar Quantity

ω Specific Turbulent Kinetic Energy Dissipation

Indices

a Ambient

c	Combustion/Chamber
$chem$	Chemical
e	Exit/Exhaust
Fu	Fuel
id	Ideal
Mix	Mixture
n	Normalized
Ox	Oxidizer
t	Turbulent
th	Throat
w	Wall

Acronyms

ATLLAS Aerodynamic and Thermal Load Interactions with Lightweight Advanced Materials for High Speed Flight.

CAD Computer Aided Design.

CEA Chemical Equilibrium with Applications.

CFD Computational Fluid Dynamics.

ECM Equilibrium Chemistry Model.

FRC Finite Rate Chemistry.

LES Large Eddy Simulations.

LRE Liquid Rocket Engine.

MMH Monomethylhydrazine.

MoRaP Mobile Rocket Test Bench (Mobiler Raketenprüfstand).

NTO Nitrogen Tetroxide.

PSRM Perfectly Stirred Reactor Model.

RANS Reynolds-averaged Navier-Stokes.

RFA Chair of Space Propulsion (Professur für Raumfahrtantriebe).

SSME Space Shuttle Main Engine.

SST Shear-Stress Transport.

TUM Technical University of Munich.

UDMH Unsymmetrical Dimethylhydrazine.

URANS Unsteady Reynolds-averaged Navier-Stokes.

1 Introduction

1.1 Motivation

Liquid Rocket Engines (LREs) burn high-energy propellants in thrust chambers with small installation volume. This leads to very high temperatures in the core flow of the combustion gas (for hydrogen/oxygen up to 3500 K). These high temperatures induce severe thermal loads on the combustor walls, which exceed even the thermal load capacity of modern high-temperature-resistant materials and therefore need to be addressed by a dedicated cooling system.

In addition, requirements for high performance and high thrust in modern rocket engines, such as the Space Shuttle Main Engine (SSME) and the first stage engine Vulcain 2 of Europe's Ariane 5 launcher, have led to high combustion pressures exceeding 100 bar. These elevated pressure levels have advantages in performance and allow engine builds with smaller installation volumes. However, they further increase the demands on the cooling system because the maximum wall heat flux in a rocket combustor (typically appearing in the nozzle throat) scales with the chamber pressure approximately according to the relation $q_{w,th} \sim p_c^{0.8}$ [1]. Figure 1.1 shows this relation for selected rocket engines and thrust levels.

Different cooling methods are usually employed to prevent overheating the combustor, which can compromise the structural integrity and lifetime of the thrust chamber. Regenerative cooling has long been the standard method and is often applied in combination with
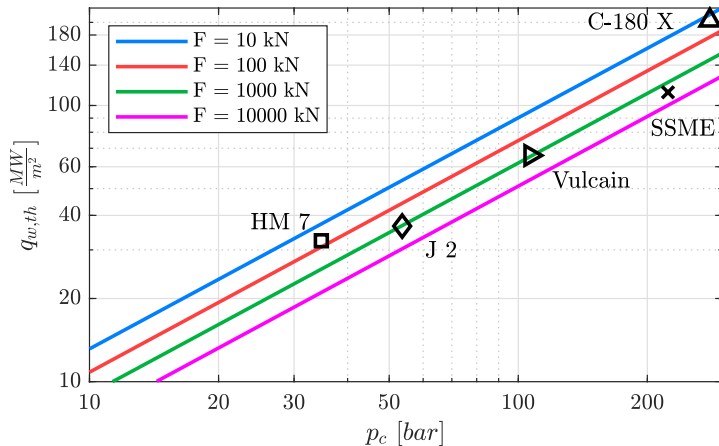
Figure 1.1: Wall heat flux in the nozzle throat as a function of chamber pressure for selected rocket engines (modified from *Schmidt* [1]).

film and radiative cooling. As an additional measure, an appropriate design of the injector head and the injector elements can help reduce the maximum thermal loads by distributing the overall heat flux evenly over the combustor wall. As discussed by *Lin et al.* [2], the injector design has a direct impact on the combustor thermal environment. Therefore, to derive an appropriate design for the injection and cooling subsystem and determine crucial engine characteristics such as combustion efficiency, heat transfer, and performance, an accurate prediction of the flow and temperature field inside the engine is necessary. Numerical design tools are often used alongside experimental test campaigns to accomplish this. *Knab et al.* [3] link the capabilities of the employed tools directly to the quality of a LRE design regarding reliability and life.

Historically simple engineering tools have been used in the layout process of rocket engines to calculate relevant design parameters and

allow the elaboration of margins and the optimization of thrust chamber components. *Sozer* [4] gives a good overview of these traditional design approaches and tools. They typically focus on predicting performance, while the calculation of heat transfer processes is included by Nusselt-type correlations. They have several shortcomings as they do not resolve critical underlying physical phenomena but rather include them by empirical formulations. This makes them unable to be applied to novel design concepts without extensive adaption work.

An alternative to these legacy tools, which has gained popularity with the increase in the computational capacity of modern personal computers, are Computational Fluid Dynamics (CFD) codes. In CFD codes, the underlying physical phenomena of the fluid flow and combustion are modeled numerically according to their governing equations. This promises an improved prediction of the thermal environment in a rocket combustor, including thermal stratifications and three-dimensional effects. These effects can hardly be included in empirical tools but are critical to local failure mechanisms found in rocket engines, as is evident by the blanching and cracking in the SSME shown in Figure 1.2.

The semi-empirical in-house code THERMTEST [5] has been the primary tool in the design and research efforts on LREs at the Chair of Space Propulsion (Professur für Raumfahrtantriebe) (RFA) of the Technical University of Munich (TUM). It was developed within the national research program ATLLAS for the test preparation and analysis of a single element lab-scale rocket engine operated with kerosene and gaseous oxygen. It is able to predict the heat transfer in capacitively- and water-cooled combustion chambers. The thermal environment inside the combustor is calculated based on the assumptions of one-dimensional flow and chemical equilibrium. The convective heat transfer on the hot gas side, as well as the coolant side, is modeled using classical empirical correlations, such as the
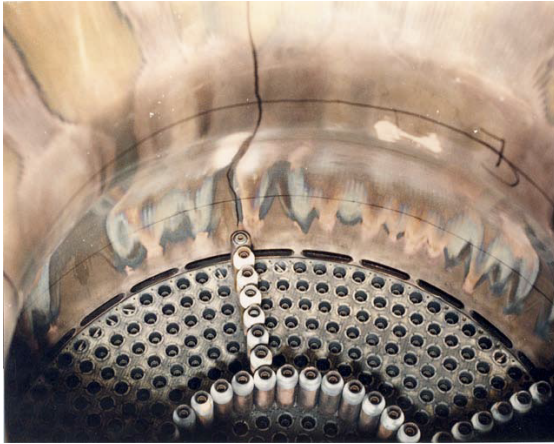
Figure 1.2: Three-dimensional blanching and cracking in the SSME (from *Lin et al.* [2]).

correlations developed by *Bartz* [6], *Sinjarev* [7], and *Kraussold* [8]. These correlations have been investigated and adapted by the partners involved in the test activities and are subsequently used as the so-called "Common Approach". In order to reproduce test results and enable the predictive capabilities of THERMTEST, an optimization involving 30 load points was performed on several of the Nusselt correlation parameters. This leads to the fact that "the optimized correlation has no physical meaning in a close sense" according to *Kirchberger* [9] and therefore likely needs adaption for new chamber designs and propellant combinations.

As the focus of the research at the RFA has shifted towards gaseous methane and gaseous oxygen as fuel combinations, an effort was taken to add additional numerical prediction capabilities based on CFD to support the design and analysis of new experimental combustor configurations. The CFD tools shall be employed alongside the legacy

tools and enable additional insight into the physics of the new combustor designs, which involve different fuel and injector types (e.g. coaxial, swirl, and pintle). The data for the validation of these tools is produced in-house as part of the research program SFB-TRR40 "Technological Foundations for the Design of Thermally and Mechanically Highly Loaded Components of Future Space Transportation Systems" [10, 11]. The present work deals with the development and validation of a numerical model based on CFD to predict performance and heat transfer characteristics in a single-element experimental rocket combustor with hydrogen/oxygen or methane/oxygen as propellants and a shear-coaxial injector.

In the past, the research on numerical simulations of LREs using CFD was focused on the combustion of hydrogen. One test case, for which exists a great number of publications, is the so-called "Penn-State Test Case" by *Pal et al.* [12] presented at the 3rd International Workshop on Rocket Combustion Modeling in 2006. The test case was conducted as part of NASA's research on "Focused Validation Data for Full Flow Staged Combustion Injectors". The objective of the experiments was to characterize the wall heat flux for fully pre-burned hydrogen/oxygen injection. Therefore, wall heat flux measurements are available as validation data. In addition, the wall pressure was measured in a single location near the injection plane. *Tucker et al.* [13] present a study comparing five different simulations of this test case. The simulations range from Reynolds-averaged Navier-Stokes (RANS) and Unsteady Reynolds-averaged Navier-Stokes (URANS) to Large Eddy Simulations (LES) with a significant computational expense. The authors conclude that "there are significant inconsistencies in the evaluation of the five simulations" and that "in terms of accurate heat flux predictions, it seems that any credible simulation must be time accurate". The latter is disputed by *Riedmann et al.* [14] showing an excellent agreement of

a RANS simulation with the experimental data. *Daimon et al.* [15] and *Sozer et al.* [16], [17] are also able to predict the experimental data within reasonable accuracy using a RANS approach. While the combustion models vary between the authors, *Daimon et al.* [15] and *Riedmann et al.* [14] show that the turbulence modeling approach has a significant impact in this test case. This is due to a large recirculation zone in the injector-near region, which leads to a stagnation point at the wall that is difficult to predict correctly for some RANS models.

Recently, rocket engine development has shifted to methane/oxygen as an alternative for traditional rocket propellants [18]. Due to its properties, it is attractive for performance, reliability, and sustainability reasons [19]. Efforts are ongoing to develop the technologies to exploit the advantages of this propellant combination [20]. While the American space exploration company SpaceX is working on their Raptor engine [21] featuring a full-flow staged combustion cycle for launcher applications, NASA developed an engine with throttling capability for a vertical takeoff and vertical landing test vehicle called the Morpheus Lander [22]. This led to an increased effort for numerical tools to be adapted and validated for this "new" propellant combination. With the availability of experimental data from a single-element rocket combustor [23], the SRF-TRR40 partners made a cooperative effort to progress on this topic. The effort focused on turbulence modelling [24] and combustion modelling [25] and presented the findings in a comparative manner [26]. The simulations showed quite a wide range in deviations between the predictions of the wall heat flux. At the same time, all underestimated the wall pressure available for multiple locations in this test case. In 2017 a subscale combustor using seven injector elements of the same type was tested, and the results were published by *Silvestri et al.* [27]. The combustor uses calorimetric data from water-cooled segments to measure the

average heat flux. The test case was simulated by *Perakis et al.* [28], *Eiringhaus et al.* [29] and *Daimon et al.* [30]. The authors are able to reproduce the heat flux reasonably well in the cylindrical part of the chamber. However, the heat transfer in the nozzle section is predicted significantly too low. *Eiringhaus et al.* [29] attribute this to an overcooling of the nozzle segments in the experiments, which leads to a non-negligible axial heat flux between the combustor segments and thus an increased heat intake by the cooling fluid in the nozzle.

A third methane test case is the so-called "ISP-1" presented by *Suslov et al.* [31]. The authors present the test data for the case in conjunction with numerical simulations by two different groups. The calculated heat flux of both groups is in line with the experimental data. The Sapienza University of Rome group uses a very simplified approach for injecting the propellants, which does not resolve the injector elements at all but uses a hot gas inlet at chemical equilibrium. Since the ISP-1 test case introduces film cooling at the wall, the approach yields good results. However, as shown in simulations without the film cooling [32], the method leads to unrealistically high wall heat fluxes in the faceplate region. The second group from Airbus DS (formerly Astrium Space Transportation) uses their in-house tool Rocflam-II [33], which can capture the characteristics of this test case quite well.

As can be seen from the listed publication, a wide variety of numerical codes implementing different approaches for turbulence and combustion modeling exist and are used to simulate the combustion process in LREs. They vary strongly in their degree of fidelity and computational expense. There is often disagreement between the results when the codes are employed for the first time to a new configuration or propellant combination. The research in this area is therefore still ongoing. The critical factors for an accurate prediction seemingly are turbulence and combustion modeling. It should

be noted that the focus in this thesis is on the prediction of wall heat transfer and performance parameters. Significantly more literature is available for cases where these aspects are only of secondary interest and other aspects, e.g. combustion instabilities or supercritical injection, are in the foreground [34, 35, 36, 37].

1.2 Objective

The objective of this thesis is the development of a numerical model based on CFD, which is able to predict the flow and combustion in a LRE. The focus is on engines using gaseous methane or hydrogen with gaseous oxygen as propellants. For this purpose, the commercial CFD solver ANSYS Fluent [38] is adapted and enhanced. A commercial solver is attractive because it is typically highly efficient in terms of computational expense with proven scalability and comes with various models implemented "out of the box". However, the complex and sometimes fringe physical phenomena occurring in rocket engines make various adaptions and enhancements to the base solver necessary. In addition, with the wide range of models available, a fitting setup needs to be found for a specific application. This model setup then needs to be validated against experimental data to improve the confidence level in the prediction results. The goal of this thesis is to achieve this for a single-element rocket combustor operated at the RFA. Validation data is available in the form of wall heat flux and pressure measurements, which should be an outcome of the numerical simulations. The model shall be able to produce results within a reasonable time frame (1-3 days is suggested by *Knab et al.* [39]) to support the design and optimization of new hardware. Where possible, the model enhancements should be standalone to enable them to be used within other engineering tools. The model shall be adaptable to future configurations, e.g. different combustion chamber geome-

tries and supercritical injection.

1.3 Overview

This thesis contains five chapters. The current chapter gives the
motivation for the present work and states the objectives aimed to
achieve. The second chapter introduces the fundamentals and defini-
tions of rocket propulsion, focusing on those relevant to understand-
ing the results presented in the later chapters. Chapter three focuses
on the numerical methods behind the model developed as part of
this thesis. The chapter is sectioned into turbulence modeling, com-
bustion modeling, and modeling of thermodynamic and transport
properties. Chapter four presents the experimental data and the nu-
merical simulations. The results of different models for turbulence
and combustion are compared and discussed. Chapter five concludes
the findings of this thesis and reviews the objectives laid out in Sec-
tion 1.2. Possibilities for future work and improvements are discussed
as well.

2 Fundamentals and Definitions of Rocket Propulsion

The following chapter gives a general overview of the fundamental principles of liquid rocket propulsion engines. Quantities and expressions that characterize the design and the performance of such engines are defined and discussed. The chapter focuses on definitions that are important to interpreting the experimental and numerical data presented in this thesis. The interested reader can find further details on the topic of liquid rocket engine design in the publications by *Sutton & Biblarz* [40], *Huzel and Huang* [41], *Schmidt* [1], and *Haidn* [42].

2.1 Rocket Engine Working Principle

A liquid rocket engine is a class of jet propulsion engines. Jet propulsion engines produce thrust by imparting a reaction force onto a vehicle by ejecting matter, called the propellant, with a high velocity. Because momentum is conserved, as implied by Newton's third law of motion, the vehicle is propelled in the opposite direction of the expelled mass. While air-breathing jet engines, such as turbojets and ramjets, use the surrounding medium as the oxidizer to be

burned together with onboard stored fuel, rocket engines carry both propellant components on the vehicle.

In bi-propellant liquid rocket engines, which are the focus of this thesis, the energy that ultimately propels the rocket is stored as chemical energy of the propellants. During operation, the energy is released in a high-pressure combustion reaction. The heat of the reaction raises the temperature of the reaction product gases to very high values of up to 3500 K. The thermal energy of these gases is now converted into kinetic energy of the exhaust flow by the expansion process in the convergent-divergent nozzle. The engine thrust is produced by the pressure the combustion gases exert onto the surface of the rocket thrust chamber.

Figure 2.1 presents a schematic overview of this principle. An equation for the produced thrust of a rocket engine can now be derived by applying a force balance in the y-direction, i.e. the velocity direction. For this purpose, all pressures are integrated over the respective areas they are acting on. The resulting force components acting radially outwards do not contribute to the production of axial thrust and cancel each other out due to the symmetry of the system. Force components acting on planes normal to the chamber axis propel the engine forward. For a steadily operating rocket engine, the force balance leads to the following expression:

$$F = \dot{m}v_e + (p_e - p_a)A_e = \dot{m}c_e, \tag{2.1}$$

where $\dot{m}$ is the total mass flow rate of the propellants, v_e is the exit velocity of the exhaust gas, p_e is the average pressure over the nozzle exit, p_a is the ambient pressure, and A_e is the cross-section area of the nozzle exit. The first term on the right-hand side is the momentum thrust. The second term represents the pressure thrust. By introducing the effective exhaust velocity c_e, the equation can
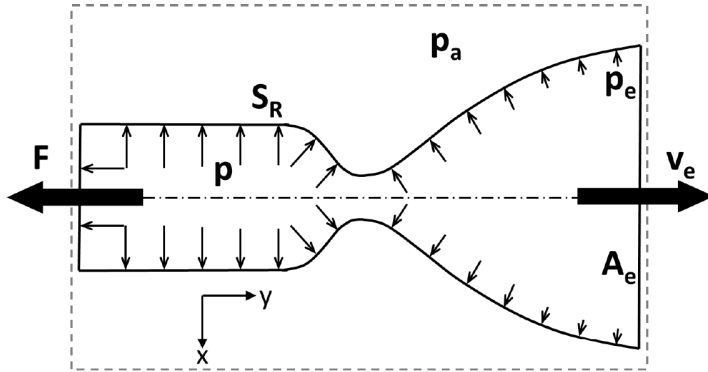
Figure 2.1: Schematic overview of the working principle of a rocket engine (modified from *Kirchberger* [9]).

be further simplified. Equation 2.1 shows that a high thrust can be achieved with either a high mass flow rate or a high velocity of the exhaust flow. A detailed derivation of this equation is presented in the work of *Sutton & Biblarz* [40].

2.2 Specific Impulse

From the principle equation for rocket engine thrust, equation 2.1, it follows that thrust can either be produced by a high propellant mass flow rate or a high exit velocity of the exhaust gases. The latter is more efficient, as the mass saved for the propellant ultimately results in a higher payload transport capability of the rocket. This leads to the following definition of the specific impulse:

$$I_{sp} = \frac{F}{\dot{m}g_0},$$

(2.2)

where g_0 is the standard gravity acceleration of 9.81 m/s^2. Therefore, the specific impulse is a measure for the energy content of the propellant combination, as higher energetic propellants infer a higher exhaust velocity. It is also an engine characteristic that indicates the efficiency of the energy conversion in the system. A higher specific impulse generates a higher thrust at the same propellant mass flow rate. The specific impulse is the primary measure for rocket engine performance.

2.3 Mixture Ratio

Figure 2.2 shows the ideal specific impulse as a function of the oxidizer to fuel ratio for a variety of propellant combinations commonly used in a liquid rocket engine. The oxidizer to fuel ratio, also called mixture ratio, is herein defined by the following relation:

$$O/F = \frac{\dot{m}_{Ox}}{\dot{m}_{Fu}},\qquad(2.3)$$

where $\dot{m}_{Fu}$ is the fuel mass flow rate and $\dot{m}_{Ox}$ is the oxidizer mass flow rate.

As Figure 2.2 shows, hydrogen/oxygen is by far the most efficient propellant combination among the most commonly used. From the hydrocarbon family, methane/oxygen is the most efficient one, followed by propane/oxygen and kerosene/oxygen, all displaying a higher specific impulse than the hypergolic combination NTO/UDMH. All presented propellants have their maximum in specific impulse at mixture ratios lower than the stoichiometric ratio. This is because the exhaust velocity is roughly proportional to $(T_c/M_w)^{0.5}$ [43], where T_c is the combustion temperature and M_w the hot gas molecular weight. Excess fuel typically leads to a lower molecular weight because it is rich in hydrogen. Note that here only the ideal specific impulse is
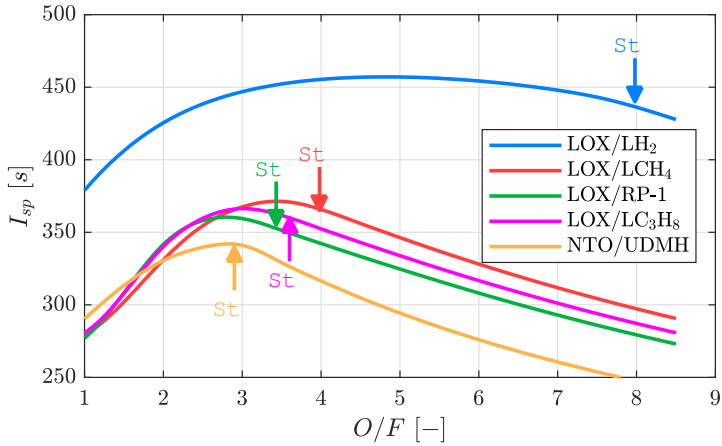
Figure 2.2: Ideal specific vacuum impulse as a function of the mixture ratio for commonly used rocket propellant combinations (p_c=100 bar, ε=45). The stoichiometric mixture ratios are indicated by arrows.

shown. Actual engines experience losses to the ideal value depending on their design characteristics. Typical sources of performance losses are incomplete mixing or incomplete vaporization, reaction kinetics, boundary layer losses, and two-dimensional exhaust flow phenomena.

2.4 Characteristic Velocity and Combustion Efficiency

Injector design directly impacts the performance of a liquid rocket engine. The injection system is responsible for efficiently processing the propellants, ultimately leading to complete combustion and thereby maximizing energy release and produced thrust. The primary mea-

sure of a rocket engine's performance related to the injection system is the characteristic velocity c^*. It describes the impulse of the engine before expansion but beyond the choked flow conditions in the nozzle throat. The following relation defines the characteristic velocity:

$$c^* = \frac{p_c A_{th}}{\dot{m}}, \tag{2.4}$$

where p_c is the effective stagnation pressure at the throat, A_{th} is the nozzle throat area, and $\dot{m}$ the total mass flow rate of oxidizer and fuel combined. This means that the characteristic velocity defines the nozzle throat area needed to achieve a certain chamber pressure at a given propellant mass flow rate. By relating the chamber pressure to the propellant mass flow rate, the characteristic velocity effectively measures the efficiency of the propellant processing by the injection system. Fully mixed and reacted propellants will generally have a higher characteristic velocity than only partially mixed and reacted propellants.

For a "perfect injector", the characteristic velocity is mainly a function of the propellant combination. A perfect injector is characterized by mixing, gasifying, and reacting the propellants to equilibrium before entering the combustion chamber. As shown by *Kirchberger* [9], applying further simplifying assumptions yields the following expression for the characteristic velocity of an idealized rocket engine system:

$$c_{id}^* = \sqrt{\frac{R_m T_c}{M_w \kappa} \left(\frac{2}{\kappa+1}\right)^{\frac{\kappa+1}{\kappa-1}}}, \tag{2.5}$$

where T_c, M_w, κ are the combustion temperature, the molecular weight, and the isentropic exponent of the combustion products respectively.

This relation shows that the characteristic velocity depends strongly on the characteristics of the propellant combination (T_c, M_w, κ) and

is only weekly dependent on the combustion pressure, as a higher pressure suppresses dissociation of the combustion products and thereby increases the combustion temperature.

In a real, i.e. non-ideal, rocket engine system, the characteristic velocity is generally less than in the ideal system due to incomplete energy release, caused by insufficient vaporization and mixing of the propellants, and insufficient combustion chamber length. The injector-related energy release efficiency (or combustion efficiency) is then defined as the ratio of the characteristic velocity of the real injector compared to the characteristic velocity of the "perfect" or "ideal" injector:

$$\eta_{c^*} = \frac{c^*}{c_{id}^*}. \tag{2.6}$$

2.5 Thrust Coefficient

The thrust coefficient gives the ratio of the total thrust produced by the engine to the virtual thrust in the throat. It is defined by the following equation:

$$c_F = \frac{F}{p_c A_{th}}. \tag{2.7}$$

The thrust coefficient defines the factor by which the nozzle increases the virtual thrust of the combustion chamber. Therefore it is a performance measure for converting the chamber energy into kinetic energy in the nozzle.

Combining equation 2.1 and equation 2.4 yields the following expression.

$$c_e = c_F \cdot c^*, \tag{2.8}$$

This indicates that the effective velocity can be found from a value representing combustion chamber characteristics, i.e. the characteristic velocity, and an increment factor representing nozzle character-

istics, i.e. the thrust coefficient.

2.6 Geometric Engine Characteristics

A critical parameter for dimensioning a liquid rocket engine is the nozzle expansion ratio. It is defined by the following relation between the throat area and the nozzle exit area:

$$\varepsilon = \frac{A_e}{A_{th}}. \tag{2.9}$$

A high expansion ratio increases the pressure thrust. For first-stage engines, the maximum value is limited by flow separation inside the nozzle due to overexpanded flow on the ground [44]. Additional limiting parameters are mass and volume.

Another important characteristic parameter for a liquid rocket engine is the contraction ratio, i.e. the ratio of the combustion chamber cross-section area to the throat area, defined by the relation:

$$\varepsilon_c = \frac{A_c}{A_{th}}. \tag{2.10}$$

It is typically determined by considerations regarding the layout of the cooling system as well as the overall thrust chamber mass and the injector design, as is explained by *Schmidt* [1]. Its final value is a point for optimization. The contraction ratio also determines the Mach number in the combustion chamber, i.e. engines with similar contraction ratios will have similar Mach numbers in the combustion chamber independent of the actual size.

The characteristic length of a rocket combustor is defined as the ratio of the combustion chamber volume until the throat to the cross-

section area of the throat:

$$l^* = \frac{V_c}{A_{th}}.$$

(2.11)

This ratio determines the dwell time of the propellants inside the combustor and implicitly impacts the combustion efficiency. Figure 2.3 shows the combustion efficiency as a function of the characteristic length for selected rocket engine thrust chambers. If the volume is too small, propellants leave the combustion chamber unreacted. The maximum characteristic length is in general restricted by mass consideration and part of a trade-off and optimization. Value recommendations for the typically required characteristic length are given in table 2.1. Required for the sufficiency of these values is also a good mixing characteristic of the injection system. Since the chemical time scales differ for the respective propellant combinations, different characteristic lengths are recommended.

Table 2.1: Recommended characteristic length for commonly used propellant combinations (from *Hagemann* [45]).

Propellant Combination	l^* [m]
LOX/GH$_2$	0.6-0.7
LOX/LH$_2$	0.7-1.0
LOX/Kerosin	1.0-1.3
NTO/MMH	0.8-1.0
NTO/UDMH	1.2
NTO/Aerozin	0.9

Table 2.2 summarizes values of the geometric engine characteristics for selected thrust chambers from literature. It includes experimental combustors as well as flight hardware. These values show that some of the experimental combustors do not have representative geomet-
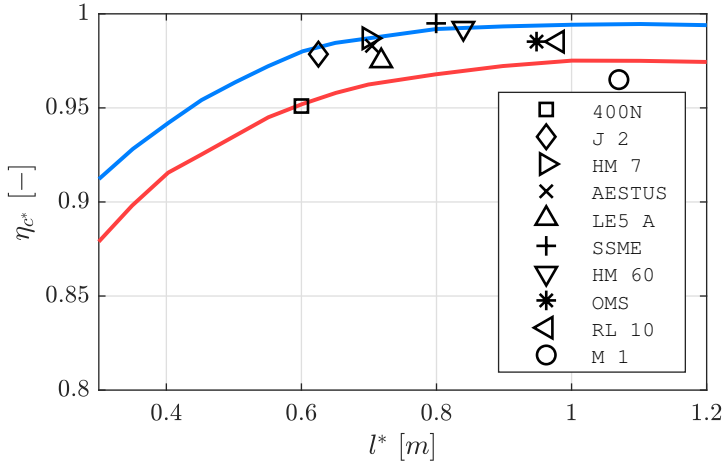
Figure 2.3: Combustion efficiency as a function of the characteristic length for selected rocket engines (modified from *Schmidt* [1]).

rical characteristics. Especially a deviating contraction ratio leads to Mach numbers not representative for actual flight hardware. The combustor that is the focus of this thesis, the MoRaP single-element round chamber, however, has a representative contraction ratio and characteristic length.

Table 2.2: Geometric characteristics for selected rocket engines (from *Schmidt* [1], *Riedmann* [46], *Silvestri* [47]).

Thrust chamber	Propellant combination	ε [-]	ε_c [-]	l^* [m]
F-1 (Saturn V)	Kerosin/O_2	16	1.26	1.220
J-2 (Saturn V)	H_2/O_2	39.8	1.58	0.625
SSME (Space Shuttle)	H_2/O_2	77.5	2.96	0.8
Vulcain (Ariane 5)	H_2/O_2	45	2.5	0.84
Aestus (Ariane 5)	MMH/NTO	84.9	2.38	0.705
Penn State (Experimental)	H_2/O_2	6.1	21.8	6.5
Mascotte (Experimental)	H_2/O_2	2	14.1	6.6
MoRaP single-element round (Experimental)	H_2/O_2 CH_4/O_2	3.1	2.5	0.75

3 Numerical Model

Liquid rocket engine thrust chamber flows typically involve complex phenomena, such as propellant mixing, high-speed turbulent flow, and combustion. The following chapter presents the physical and chemical fundamentals underlying the mathematical model employed in this thesis to simulate these processes. The chapter also introduces their numerical treatment. It presents general aspects necessary for understanding and interpreting the numerical simulation results in the later chapters. The focus is the modeling of turbulence and combustion and the thermophysical properties of the high-temperature, high-pressure gas flow in a rocket combustor. The ability of a numerical model to treat these aspects is regarded as integral to thrust chamber performance and heat load analysis.

The interested reader can find additional details on computational fluid dynamics as well as combustion modelling in the publications by *Ferziger & Peric* [48], *Poinsot & Veynante* [49] as well as *Gerlinger* [50]. *Gardiner & Burcat* [51] as well as *Bird et al.* [52] give a good overview on methods for calculating thermophysical properties.

3.1 Governing Equations of Turbulent Fluid Flow

In general, the fluid flow in a technical application is described by a set of partial differential equations. These equations are derived

from balance equations for mass, momentum, energy, and species in a rocket engine combustor. This set of equations is referred to as Navier-Stokes equations.

Due to the low viscosity and high fluid speed in a rocket combustor, and therefore high Reynolds numbers, the flow is strongly turbulent. Turbulent flows are characterized by irregular statistical fluctuations of the velocity field in time and three-dimensional space [53]. These fluctuations have a mixing effect on all transported quantities and induce fluctuations of the transported quantities themselves. The scale of these fluctuations extends from large eddies, limited in size by the physical geometry of the combustor, to small, high-frequency eddies at the Kolmogorov micro-scale, at which viscosity dominates, and the turbulent kinetic energy is dissipated into heat. Even though the Navier-Stokes equations, in principle, describe the turbulence field, the direct resolution of all scales is typically not feasible for relevant technical applications since it is extremely computationally expensive.

For this reason, an averaging procedure is applied here, which eliminates the need to simulate the wide range of the turbulent spectrum directly by modeling the influence of turbulence on the mean flow. The procedure is based on Reynolds-averaging (which, in principle, is temporal averaging) of the instantaneous Navier-Stokes equations. It is the most widely applied method for technical applications and results in the Reynolds-Averaged Navier-Stokes (RANS) equations.

This method takes the formal average of the exact equations introducing the following averages:

- The simple average (Reynolds average)

$$\phi = \bar{\phi} + \phi',$$

  where $\bar{\phi}$ is the average and ϕ' is the fluctuation.

- The mass weighted average (Favre average)

$$\phi = \tilde{\phi} + \phi'',$$

where $\tilde{\phi} = \frac{\overline{\rho\phi}}{\bar{\rho}}$ is the average and ϕ'' is the fluctuation.

Applying this method to the conservation equation for mass yields the continuity equation:

$$\frac{\partial \bar{\rho}}{\partial t} + \frac{\partial (\bar{\rho}\tilde{u}_i)}{\partial x_i} = 0, \tag{3.1}$$

where $\bar{\rho}$ is the Reynolds-averaged density of the fluid mixture and $\tilde{u}_i$ is the Favre-averaged velocity component in the spatial direction of x_i. Note that the Einstein summation convention is used here for simplicity.

Averaging the momentum equations in three-dimensional space leads to the RANS equations describing the velocity field:

$$\frac{\partial (\bar{\rho}\tilde{u}_i)}{\partial t} + \frac{\partial (\bar{\rho}\tilde{u}_i\tilde{u}_j)}{\partial x_j} = -\frac{\partial \bar{p}}{\partial x_i} + \frac{\partial}{\partial x_j}\left(\bar{\tau}_{ij} - \overline{\rho u_i'' u_j''}\right), \tag{3.2}$$

where $\bar{p}$ is the Reynolds-averaged pressure and $\bar{\tau}_{ij}$ the viscous stress tensor. The term $\overline{\rho u_i'' u_j''}$ is the Reynolds stress tensor and represents the momentum transport due to the turbulent motion of the fluid. The Reynolds stress tensor is an unclosed term that needs to be treated by an appropriate turbulence model. The methods applied in this thesis for modeling turbulence are described in section 3.2.

The same procedure is applied to the energy equation. However, the energy equation can be cast in different forms. The form used usually depends on the combustion model employed. There are two different forms of energy equations employed in the subsequent studies. The first one is the enthalpy form:

$$\frac{\partial (\bar{\rho}\tilde{h})}{\partial t} + \frac{\partial (\bar{\rho}\tilde{u}_i\tilde{h})}{\partial x_i} = \frac{\partial}{\partial x_i}\left(\frac{\bar{\lambda}}{\bar{c}_p}\frac{\partial \tilde{h}}{\partial x_i} - \overline{\rho u_i'' h''}\right), \tag{3.3}$$

where $\tilde{h}$ is the Favre-averaged enthalpy, and $\bar{\lambda}$ and $\bar{c}_p$ are the Reynolds-averaged thermal conductivity and specific heat capacity of the mixture, respectively. The term $\overline{\rho u_i'' h''}$ is the turbulent enthalpy flux. It is also an unclosed term, and its treatment is detailed in Section 3.2.1. This form is used when simulating combustion with a tabulated chemistry approach.

The second one is the total energy form:

$$\frac{\partial(\bar{\rho}\tilde{e})}{\partial t} + \frac{\partial(\tilde{u}_i(\bar{\rho}\tilde{e} + \bar{p}))}{\partial x_i} = \frac{\partial}{\partial x_i}\left(\bar{\lambda}\frac{\partial \tilde{T}}{\partial x_i} - \overline{\rho u_i'' e''}\right) + S_e, \qquad (3.4)$$

where $\tilde{e}$ is the Favre-averaged total energy and $\tilde{T}$ is the flow temperature. The term S_e is a source term that equals the heat of chemical reaction. This form is used when employing finite rate chemistry. *Poinsot & Veynante* [49] present a good overview of the different forms of the energy equation.

There also exist two different forms of the species transport equation. The first form yields a set of equations following directly from averaging the species balance equations of each individual species:

$$\frac{\partial(\bar{\rho}\tilde{Y}_k)}{\partial t} + \frac{\partial(\bar{\rho}\tilde{u}_i\tilde{Y}_k)}{\partial x_i} = \frac{\partial}{\partial x_i}\left(\bar{\rho}\bar{D}_{Yk}\frac{\partial \tilde{Y}_k}{\partial x_i} - \overline{\rho u_i'' Y_k''}\right) + S_{Y_k}, \qquad (3.5)$$

where $\tilde{Y}_k$ is the Favre-averaged species mass fraction of the species k and $\tilde{D}_{Y_k}$ is its laminar diffusion coefficient. The term S_{Y_k} is a source term that equals the net rate of production of the species by chemical reaction. This form is used when employing finite rate chemistry.

Under certain assumptions it is possible to reduce the thermo-chemistry of a particular flow to a single variable called the mixture fraction. The mixture fraction will be defined in section 3.3.1. Its

conservation equation is introduced here for completeness as:

$$\frac{\partial(\bar{\rho}\tilde{Z})}{\partial t} + \frac{\partial(\bar{\rho}\tilde{u}_i\tilde{Z})}{\partial x_i} = \frac{\partial}{\partial x_i}\left(\bar{\rho}\bar{D}_Z\frac{\partial \tilde{Z}}{\partial x_i} - \widetilde{\bar{\rho}u_i''Z''}\right), \qquad (3.6)$$

where $\tilde{Z}$ is the Favre-averaged mixture fraction and $\tilde{D}_Z$ is its laminar diffusion coefficient.

The Reynolds averaging process makes it possible to remove all turbulent fluctuations from the flow. The net effect of the turbulence is kept by modeling its influence on the smooth variations of the averaged quantity fields. However, the introduced unclosed terms, representing the turbulent fluxes, need to be addressed by an appropriate turbulence model. The choice of the turbulence model can have a significant impact on the simulation results and must be chosen according to the specific class of the problem at hand.

3.2 Turbulence Modeling

3.2.1 Treatment of Turbulent Fluxes

Reynolds-averaging of the governing equations, as introduced in section 3.1, leads to unclosed terms in the transport equations. These terms represent the transport of the respective quantity of the equation due to the influence of turbulent eddies present in the mean flow. They cannot be resolved feasibly by calculating them directly for typical technical applications. Therefore the terms are modeled by relating them to the solution variables of the flow field, thereby closing the equations system.

The turbulent momentum flux is modeled by employing the Boussinesq hypothesis [54], which relates the Reynolds stresses to the mean

local velocity gradient in the flowfield:

$$\bar{\rho}\widetilde{u_i'' u_j''} = -\mu_t \left(\frac{\partial \tilde{u}_i}{\partial x_j} + \frac{\partial \tilde{u}_j}{\partial x_i} - \frac{2}{3}\delta_{ij}\frac{\partial \tilde{u}_k}{\partial x_k} \right) + \frac{2}{3}\bar{\rho}\tilde{k}, \qquad (3.7)$$

where μ_t is the turbulent viscosity and k the turbulent kinetic energy. δ_{ij} is the Kronecker delta.

Now, to close the momentum equation, the turbulent viscosity needs to be determined. The turbulent viscosity is proportional to two characteristic turbulence scales, a velocity scale u_t and a length scale l_t:

$$\mu_t \sim u_t \cdot l_t. \qquad (3.8)$$

There are several different approaches found in literature to determine these scales. A good overview is given by *Versteeg* [55]. The most commonly used, and the one adopted here, is employing a two-equation turbulence model. This approach introduces two new transport equations, which have to be solved in addition to the governing equations. One is representing the transport of the turbulent kinetic energy in the flow, which determines the amount of energy in the turbulence and is related to the velocity scale by $u_t = \sqrt{k}$. The other one can be thought of as a variable that determines the scale of the turbulence (length-scale or time-scale). Details on the two-equation models used in this thesis are presented in Section 3.2.2.

The turbulent enthalpy flux is modeled by introducing a relation to the mean local enthalpy gradient in the flowfield:

$$\bar{\rho}\widetilde{u_i'' h''} = -\frac{\mu_t}{Pr_t}\frac{\partial \tilde{h}}{\partial x_i}, \qquad (3.9)$$

where Pr_t is the turbulent Prandtl number. The treatment of the unclosed term in the total energy equation is equivalent.

The turbulent Prandtl number is a non-dimensional variable de-

fined as:

$$Pr_t = \frac{\mu_t \bar{c}_p}{\lambda_t}, \qquad (3.10)$$

where λ_t is the turbulent conductivity. The turbulent Prandtl number represents the ratio between the turbulent momentum flux and the turbulent enthalpy flux. This analogy is used here to determine the turbulent transport of enthalpy. Typically a constant value for the turbulent Prandtl number is set within the solution domain. Examples listed by *Gerlinger* [50] and *Kays* [56] suggest a range of $0.5 \leq Pr_t \leq 1.0$ for gaseous flow. A value close to 1.0 makes sense from a phenomenological point of view, as the underlying physical mechanism for the transport of momentum and enthalpy is the same, namely the turbulent motion of the fluid. This analogy helps avoid solving additional equations to calculate the turbulent conductivity, as is done for the turbulent viscosity in the momentum equation. However, different models for calculating the turbulent conductivity can be found in literature, ranging from simple algebraic equations [57] to more complex two-equation models [58]. The calculation examples presented in these publications confirm the limited value range of the turbulent Prandtl number.

Even though the value of the turbulent Prandtl number is usually limited to a small range of values, its variation can significantly impact the prediction of the wall heat flux in liquid rocket engines. This is shown by *Riedmann et al.* [14] and *Chemnitz et al.* [24]. Therefore care must be taken when choosing its value. *Riedmann* [46] suggest to choose the value for different propellant combinations independently. The influence of the turbulent Prandtl number on the predictions of performance and heat transfer in this thesis is investigated in Section 4.4.3.

The turbulent species flux is modeled by introducing a relation to the mean local species gradient of each individual species k in the

flowfield:

$$\widetilde{\bar{\rho} u_i'' Y_k''} = -\frac{\mu_t}{Sc_t} \frac{\partial \tilde{Y}_k}{\partial x_i}, \tag{3.11}$$

where Sc_t is the turbulent Schmidt number. The treatment of the unclosed term in the mixture fraction equation is done in the same manner by replacing the mass fraction with the mixture fraction.

The turbulent Schmidt number is a non-dimensional variable defined as:

$$Sc_t = \frac{\mu_t}{\bar{\rho} \bar{D}_k}. \tag{3.12}$$

The turbulent Schmidt number represents the ratio between the turbulent momentum transport and the turbulent species transport.

Like the turbulent Prandtl number, the turbulent Schmidt number is usually set to a constant value throughout the fluid domain. This exploits the same phenomenological analogy to the turbulent transport of momentum as for the turbulent enthalpy. A value of $0.7 \leq Sc_t \leq 1.0$ is recommended by *Gerlinger* [50]. Models for closing the species transport equation without using the analogy to the turbulent momentum transport are also found in literature [58]. The influence of the turbulent Schmidt number on the predictions of performance and heat transfer in this thesis is investigated in Section 4.4.3.

3.2.2 RANS Turbulence Models

There exist several different approaches to determine the turbulent viscosity μ_t, which is needed to calculate the Reynolds stresses in Equation 3.2 and close the momentum equations. They are typically differentiated by the number of additional transport equations that have to be solved [59]. In this thesis, only two-equation models are employed due to their superior accuracy. In total, four different models are used. Two belong to the k-ε family, which uses the dis-

sipation rate ε of the turbulent kinetic energy as the characteristic length-scale. The other two belong to the k-ω family and use the *specific* dissipation rate ω of the turbulent kinetic energy as the characteristic length-scale. The following chapter gives an overview of the theoretical and numerical background of these models.

3.2.2.1 Standard k-ε Model

The standard k-ε model, introduced by *Jones & Launder* [60] in 1972, is one of the most widely used turbulence models in practical engineering flow calculations. It is a two-equation model that solves additional transport equations for the turbulent kinetic energy k and the turbulent dissipation rate ε. The turbulent viscosity μ_t is calculated from these two quantities for the entire velocity field. It can then be substituted into the momentum equations, where it accounts for the additional mixing due to turbulent fluctuations. This closes the system of governing equations for fluid flow and makes the solution of the RANS equations possible.

While the equation for the turbulent kinetic energy is derived from the exact equation, the turbulent dissipation rate is obtained by introducing empirically determined terms and relies on phenomenological considerations. The nature of this model is, therefore, semi-empirical. This is necessary because the exact equation for the turbulent dissipation rate includes many unclosed terms involving higher-order moments, which are hard to resolve. The empirical terms and their coefficients have been fine-tuned based on various classes of flows, making the model reasonably accurate for many practical applications.

The turbulent kinetic energy and the turbulent dissipation rate are

obtained from the following set of equations:

$$\frac{\partial(\bar{\rho}\tilde{k})}{\partial t} + \frac{\partial(\bar{\rho}\tilde{u}_i\tilde{k})}{\partial x_i} = \frac{\partial}{\partial x_i}\left[\left(\mu + \frac{\mu_t}{\sigma_k}\right)\frac{\partial\tilde{k}}{\partial x_i}\right] + P_k - \bar{\rho}\varepsilon, \qquad (3.13)$$

$$\frac{\partial(\bar{\rho}\varepsilon)}{\partial t} + \frac{\partial(\bar{\rho}\tilde{u}_i\varepsilon)}{\partial x_i} = \frac{\partial}{\partial x_i}\left[\left(\mu + \frac{\mu_t}{\sigma_\varepsilon}\right)\frac{\partial\varepsilon}{\partial x_i}\right] + C_{1\varepsilon}\frac{\varepsilon}{\tilde{k}}P_k - C_{2\varepsilon}\bar{\rho}\frac{\varepsilon^2}{\tilde{k}}, \quad (3.14)$$

where σ_k, σ_ε, $C_{1\varepsilon}$ and $C_{2\varepsilon}$ are modelling constants and P_k is the production term for turbulent kinetic energy. The production term is modeled consistent with Boussinesq hypotheses and evaluated as $P_k = \mu_t S^2$, with S being the mean rate-of-strain.

The local turbulent viscosity is then computed from the following relation:

$$\mu_t = \rho C_\mu \frac{\tilde{k}^2}{\varepsilon}, \qquad (3.15)$$

where C_μ is a modeling constant. The turbulent kinetic energy k is a measure for the mean kinetic energy per unit mass present within the eddies in a turbulent flow. The turbulent dissipation rate ε is the rate at which this kinetic energy is converted into thermal energy by the action of viscosity.

The coefficients for this model were firstly introduced by *Jones & Launder* [60], but have been revised later by *Launder & Sharma* [61] to their current default values. The values for the coefficients are summarized in Table 3.1.

Table 3.1: Modeling constants for the standard k-ε model [61].

σ_k	σ_ε	$C_{1\varepsilon}$	$C_{2\varepsilon}$	C_μ
1.0	1.3	1.44	1.92	0.09

The derivation of the standard k-ε model assumes that the flow

is homogeneous, isotropic, and fully turbulent. The effects of the molecular viscosity are negligible. If these assumptions do not apply in certain regions of the flowfield, the model loses its validity, and its predictions become unreliable. This is the case especially for wall-bounded flows, as are present in rocket combustors. Here tangential fluctuations are damped by the wall's presence and become negligible compared to the normal fluctuations. This leads to anisotropic turbulence behavior. The use of wall functions can remedy this drawback. However, wall functions typically have inferior accuracy in heat transfer simulations compared to wall resolved approaches. Since the wall heat flux prediction in rocket combustion chambers is a focus of this thesis, the viscosity-affected near-wall region is resolved all through the viscous sublayer with very fine grid cells. This makes the use of wall functions superfluous, but the need for a specific wall treatment necessary. Two different treatments for the standard k-ε model are applied here to account for the presence of the wall.

The first treatment uses a zonal approach based on a so-called "two-layer" formulation to circumvent the model's validity problem. The flow field is divided into two zones (or layers) in this approach, a fully turbulent core flow, and a viscosity-affected near-wall region. In the core flow, the previously described two-equation model is solved. Close to the wall the one-equation model by *Wolfshtein* [62] is applied. It retains the transport equation for the turbulent kinetic energy but solves for the turbulent viscosity according to the relation:

$$\mu_{t,2layer} = \bar{\rho} C_\mu l_\mu \sqrt{\tilde{k}}, \tag{3.16}$$

where l_μ is the turbulent length scale. The length scale l_μ is defined by an algebraic equation and is by definition damped close to the wall, reducing the effective size of eddies in that region. This gives an improved prediction of the effect of turbulence in the near-wall

region. A blending function is then employed to smoothen the two-layer definition of the turbulent viscosity with the core-flow definition. The start of the transition between the two zones is determined by the turbulent Reynolds number Re_t, which scales with the normal distance to the closest wall. It is defined as:

$$Re_y = \frac{\bar{\rho} y \sqrt{k}}{\bar{\mu}},\tag{3.17}$$

where y is the distance normal to the wall. Further details on the implementation and coefficients of this model are given in [63].

The second treatment uses a so-called "low-Reynolds" modification to predict the correct behavior of wall-bounded flows. Damping functions are added to the transport equation of the turbulent dissipation rate and the definition of the turbulent viscosity (Equation 3.15). These damping functions are only active close to walls, where they damp the effect of the turbulent viscosity compared to the effect of the molecular viscosity. They allow for the correct reproduction of the limiting behaviors of various flow quantities close to the wall. In this thesis, the damping function presented by *Abe, Kondoh & Nagano* [64] are used.

3.2.2.2 Yap-Correction

An implementation of the so-called "Yap-Correction" was added to both k-ε model variants. *Yap* [65] introduced this correction in 1987 to improve his predictions of flows involving separation. A source term is added to the transport equation for turbulent dissipation rate to reduce the departure of the turbulence length scale from its equilibrium value. The correction has also shown improved results in flows with stagnation points. As it seldom causes problems because it is only active in non-equilibrium flows, *Launder* [66] suggests including the correction by default. *Riedmann* [14] showed a strong impact and

improvement for the heat flux prediction of an experimental rocket combustor when employing the Yap-Correction.

The source term that is added to the transport equation for turbulent dissipation rate is defined as:

$$P_{\varepsilon, Yap} = 0.83 \frac{\varepsilon^2}{\tilde{k}} \left(\frac{\tilde{k}^{1.5}}{\varepsilon l_\varepsilon} - 1 \right) \left(\frac{\tilde{k}^{1.5}}{\varepsilon l_\varepsilon} \right)^2, \tag{3.18}$$

where $l_\varepsilon = C_{\mu_t}^{-0.75} \tilde{k} y$. The source term is only used when it is positive however.

3.2.2.3 Standard k-ω Model

The standard k-ω model was introduced by *Wilcox* [67] in 1988 in order to improve the accuracy of predictions involving boundary layers with adverse pressure gradients. It was later adapted by *Wilcox* [68] to its current form by including modifications for low-Reynolds number effects, compressibility, and shear flow spreading. It is a two-equation model that solves additional transport equations for the turbulent kinetic energy k and the specific turbulent dissipation rate ω. The turbulent viscosity is again calculated from these two quantities for the entire velocity field, closing the open terms in the fluid flow equations. The specific turbulent dissipation rate is used as the length scale determining quantity. It is defined by the identity:

$$\omega = \frac{\varepsilon}{C_\mu \tilde{k}}. \tag{3.19}$$

The transport equation for the turbulent kinetic energy is the same that is used for the k-ε model, i.e. Equation 3.13. It has only minor modifications to the dissipation term. However, ω is transported instead of ε as the length scale determining variable. Its transport is modeled empirically, incorporating several fine-tuned modeling coef-

ficients. The transport equation is defined as:

$$\frac{\partial(\bar{\rho}\omega)}{\partial t}+\frac{\partial(\bar{\rho}\tilde{u}_i\omega)}{\partial x_i}=\frac{\partial}{\partial x_i}\left[\left(\mu+\frac{\mu_t}{\sigma_\omega}\right)\frac{\partial\omega}{\partial x_i}\right]+\alpha\frac{\omega}{\tilde{k}}P_k-\bar{\rho}\beta f_\beta\omega^2. \quad (3.20)$$

The modeling coefficients are given in Table 3.2. The additional coefficients for the model (α, β and f_β) and their calculations are presented in [63].

Table 3.2: Modeling constants for the standard k-ω model [68].

σ_k	σ_ω	C_μ
2.0	2.0	0.09

The following relation then calculates the local turbulent viscosity:

$$\mu_t=\bar{\rho}\frac{\tilde{k}}{\omega}. \quad (3.21)$$

The k-ω model is inherently a low-Reynolds turbulence model. This means it can be integrated through the viscous sublayer. Therefore no additional terms or damping functions need to be added to use the model with a wall resolving computational grid.

3.2.2.4 Shear-Stress Transport (SST) k-ω Model

The Shear-Stress Transport (SST) k-ω model developed by *Menter* [69] is a hybrid model that has become popular for a wide variety of engineering flows. The model blends the k-ε model formulation in the freestream with the k-ω model formulation near the wall. For this purpose, the transport equation for the turbulent dissipation rate ε is transformed into a transport equation for the specific turbulent dissipation rate ω by using the identity Equation 3.19. This leads to

the introduction of a cross-diffusion term defined as:

$$D_\omega = 2(1 - F_1)\bar{\rho}\frac{1}{\omega\sigma_{\omega,2}}\frac{\partial k}{\partial x_j}\frac{\partial \omega}{\partial x_j}, \tag{3.22}$$

where F_1 is a blending function. If $F_1 = 0$ the model is equivalent to the k-ε formulation, if $F_1 = 1$ the model is equivalent to the k-ω formulation. The actual value of the blending function depends on the distance from the nearest wall cell.

The transport equations for the turbulent kinetic energy and the specific turbulent dissipation rate have the same form as the equations used in the standard k-ω model, i.e. Equation 3.13 and Equation 3.20 respectively. The exception being the inclusion of the cross-diffusion term 3.22 in the ω-equation. However, the turbulent diffusivity coefficients are calculated according to the following relations:

$$\sigma_k = \frac{1}{F_1/\sigma_{k,1} + (1 - F_1)/\sigma_{k,2}}, \tag{3.23}$$

$$\sigma_\omega = \frac{1}{F_1/\sigma_{\omega,1} + (1 - F_1)/\sigma_{\omega,2}}, \tag{3.24}$$

where F_1 is again the blending function. The modeling coefficients are listed in Table 3.3.

Table 3.3: Modeling constants for the Shear-Stress Transport (SST) k-ω model [69].

$\sigma_{k,1}$	$\sigma_{\omega,1}$	$\sigma_{k,2}$	$\sigma_{\omega,2}$	a_1
1.176	2.0	1.0	1.168	0.31

The local turbulent viscosity is then calculated as follows:

$$\mu_t = \rho \frac{k}{\omega} \frac{1}{\max\left(\frac{1}{\alpha^*}, \frac{SF_2}{a_1\omega}\right)},$$

(3.25)

where the term $1/\max\left(\frac{1}{\alpha^*}, \frac{SF_2}{a_1\omega}\right)$ is a limiter function, which limits the turbulent viscosity near the wall and was added to improve the overprediction of the wall shear stress. The addition of this limiter resulted in better agreement with experimental data in separated flows.

The Shear-Stress Transport (SST) k-ω model can be used as a low-Re turbulence model without the need for additional damping functions or a two-layer approach. The various additional coefficients for the model and the calculation of the blending functions are presented by *Menter* [70].

3.3 Combustion Modeling

In bi-propellant liquid rocket engines, the fuel, and the oxidizer enter the combustion chamber in distinct streams. The propellants are then simultaneously mixed and burned at the molecular level. This type of combustion is called non-premixed combustion. The correct representation of the non-premixed combustion process is essential for predicting an engine's performance and heat transfer characteristics. This encompasses modeling the initial heat release in the flame zone and the post-flame recombination reactions in the strongly cooled boundary layer.

There is a multitude of different methods available for the numerical treatment of reactive flows. They typically differ enormously in their computational expense. Their validity for a given application is dependent on the combustion chemistry of the propellant combina-

tion. The difficulty is describing the reaction progress and the fluid flow evolution, which happen on different time scales.

If the chemical reactions are "fast", in comparison to the mixing process, the combustion is mixing-limited, and the reacting mixture tends to be in local chemical equilibrium. If the mixing time scale is in the same order as the chemical time scale, finite rate chemistry effects occur. This fact is typically expressed by the Damköhler number Da, which is defined as the ratio between the mixing time scale and the chemical time scale:

$$Da = \frac{t_{mix}}{t_{chem}}. \tag{3.26}$$

Therefore, for $Da >> 1$, the mixing time scale is much larger than the chemical time scale, and the reactive flow leans towards chemical equilibrium.

Modeling approaches based on the assumption of chemical equilibrium have been successfully employed for simulations of hydrogen-fueled rocket engines [14, 71, 72], where the chemical time scales are small due to the fast chemistry of the propellants. However, the applicability of this approach to hydrocarbon engines is still debated [73]. To overcome the insufficiency of the equilibrium assumption and incorporate chemical kinetic effects, methods based on the classical Flamelet model developed by *Peters* [74] and applied to turbulent combustion by *Peters* [75] have gained in popularity. However, to capture the effects of heat loss in a rocket combustor near the cooled walls, a non-adiabatic extension to the classical model is necessary. *Lee et al.* [76] use an additional source term in the unsteady Flamelet equations to capture the heat loss process and employ the results for the simulation of a hydrogen/oxygen rocket engine. The source term is determined employing Nusselt-number correlations. In contrast *Proch et al.* [77] reduce the chemical reaction source in the Flamelet equation by a constant factor. *Wu et al.* [78] modify the

boundary condition in the Flamelet equation in the form of a permeable wall. *Frank et al.* [79] summarize these methods. *Perakis et al.* [80] uses a prescribed enthalpy profile method to incorporate heat loss effects into a Flamelet model. The model is then used to simulate one of the experimental rocket combustors that are also part of the investigated configurations of this thesis. The problem which becomes evident from *Perakis et al.* [73] is that the Flamelet model only takes non-equilibrium effects into account where the scalar dissipation rate is high. This is not the case for the strongly cooled boundary layer near the wall. Therefore, *Perakis et al.* [73] conclude "the low magnitude of the scalar dissipation in the boundary layer makes the non-adiabatic Flamelet behave like the ECM" (where ECM is the Equilibrium Chemistry Model discussed in Section 3.3.1.1).

In this thesis, different combustion models varying in degree of fidelity and computational expense are employed and compared. Their theoretical and numerical background is presented in the following sections. Their applicability and validity for liquid rocket engine combustor analysis are discussed in chapter 4.

3.3.1 Tabulated Chemistry Models

For high Damköhler numbers ($Da >> 1$), the mixing time scale is much larger than the chemical time scale, and the reactive flow tends towards local chemical equilibrium. The turbulent mixing of the propellants then limits the combustion progress. This can be used to reduce the combustion progress to a mixing problem. Now the determination of the thermochemistry is decoupled from the calculation of the turbulent flow.

Thermochemical calculations can then be pre-processed and the results stored in look-up tables. These tables are evaluated during the solution of the fluid flow equations, and the relevant variables

are interpolated. This procedure is very efficient and negates the time-consuming computation of stiff chemical systems during the flow solution.

Additionally, the instantaneous thermochemical state of the fluid is now related to only a single parameter, called the mixture fraction. The mixture fraction is defined as the mass fraction originating from the fuel inlet stream:

$$Z = \frac{Z_i - Z_{i,Ox}}{Z_{i,Fu} - Z_{i,Ox}}, \tag{3.27}$$

where Z_i is the elemental mass fraction of the chemical element i, and the subscripts Ox and Fu denote values originating from oxidizer or fuel streams, respectively. If the diffusion coefficients for all species are equal, the definition of the mixture fraction becomes unique. The reaction source terms in the species equations cancel, which makes the mixture fraction a conserved quantity.

Instead of solving a transport equation for each species, only a single equation for the mixture fraction is solved. The species concentrations are then derived from the calculated mixture fraction field. The conservation equation for the mixture fraction is given in Equation 3.6.

Due to the high temperatures in a liquid rocket engine, cooling the combustor walls induces a high convective heat transfer. Accordingly the exhaust gas departs from the adiabatic thermodynamic state. The local thermochemical state is no longer only determined by the mixture fraction, but also by the enthalpy. The enthalpy is a transported quantity in the flow solution, and its conservation is described by Equation 3.3.

Liquid rocket engines typically operate at high pressures in the combustion chamber. The exhaust gas is then expanded in the convergent-divergent nozzle. This accelerates the flow and increases the impulse

that propels the rocket. During the expansion, the pressure drops significantly. This influences the thermodynamic state of the combustion gases and adds a third independent variable to the chemistry look-up table.

Before the flow solution, the thermochemical calculations are repeatedly carried out over the entire range of mixture fraction Z, enthalpy h, and pressure p present in the domain. The resulting thermochemical properties are stored in a multidimensional look-up table and are interpolated during the flow calculation based on the local thermodynamic state in the fluid. This negates the need to perform these time-consuming computations at every iteration of the flow solution.

Here the look-up tables are parameterized using normalized variables. This simplifies the finding process when interpolating values and yields a well-defined parameter space. Now, all the instantaneous quantities such as temperature, density, mass fractions, and thermodynamic as well as transport properties are stored as functions of three independent variables:

$$\tilde{\phi} = \tilde{\phi}(\Lambda_1, \Lambda_2, \Lambda_3). \tag{3.28}$$

The first parameter is the mean mixture fraction $\tilde{Z}$, which is a measure for the local oxidizer to fuel ratio. It is normalized by definition:

$$\Lambda_1 = \tilde{Z}, \quad 0 \leq \Lambda_1 \leq 1. \tag{3.29}$$

Its definition space reaches from all oxidizer $\tilde{Z} = 0$ to all fuel $\tilde{Z} = 1$:

The second parameter takes into account the heat loss at the combustor wall. It is the normalized enthalpy defined as:

$$\Lambda_2 = h_n = \frac{\tilde{h} - h_{min}(\tilde{Z})}{h_{max}(\tilde{Z}) - h_{min}(\tilde{Z})}, \quad 0 \leq \Lambda_2 \leq 1. \tag{3.30}$$

The minimum and the maximum value are varied depending on the local mixture fraction. The maximum value is typically set close to the adiabatic value, i.e. the enthalpy of the propellant mixture at injection. This is reasonable as there is no substantial heat gain in the combustion chamber. The minimum value is based on a minimum temperature, which can be assigned as constant or varying over the mixture fraction space. The value is chosen arbitrarily based on the best guess (e.g. wall temperature measurements or cooling fluid temperatures), and its sufficiency should be checked a posteriori.

The third parameter is the normalized pressure. The dependency of the thermodynamic properties on pressure mainly plays a role in the combustor nozzle, where the flow is strongly expanded. The normalized pressure is defined as:

$$\Lambda_3 = p_n = \frac{\log \bar{p} - \log p_{min}}{\log p_{max} - \log p_{min}}, \quad 0 \le \Lambda_3 \le 1. \tag{3.31}$$

The maximum value for pressure p_{max} is set close to the expected operating pressure. For the minimum, a very low value of 0.1 bar is typically sufficient.

A user-developed extension to the base CFD solver was implemented to enable the use of pre-processed chemistry tables for the combustor flow simulations. The extension reads the prepared tables into the computer memory, ensures a consistent initialization of the flow field, processes the tables, and handles the data input and output with the flow solver.

During the fluid flow solution, the independent variables are passed to the table processor. As in general, the values of the passed independent variables are in-between two of the discretely stored points of the chemistry table, a bisection method by *Press et al.* [81] is used to locate the encompassing table indices. Note that the table has to be ordered, i.e. be either strictly ascending or descending. Once this

search is performed for all independent variables, multidimensional linear interpolation is used to calculate the instantaneous value of the dependent variable. Currently, the table processor can handle tables with up to four independent variables. The program is, however, easily extendable to more dimensions by updating the interpolation routine.

3.3.1.1 Equilibrium Chemistry Model

For the tabulation of the thermochemical variables under the assumption of local chemical equilibrium, an in-house tool was developed as part of this thesis. The tool uses NASA's Chemical Equilibrium with Applications (CEA) code [82, 83] to determine the composition and mixture properties based on the thermodynamic state. The CEA program's chemical equilibrium solver employs a so-called "stoichiometric" method. The method is based on the minimization of free energy, specifically Gibbs energy. In this method, in contrast to "non-stoichiometric" element potential methods, individual species can be treated independently of each other. Therefore no set of reactions has to be specified a priori.

The tool iterates the entire space bounded by the user defined minimum and maximum values of the independent variables ($\tilde{Z}$, h, p). CEA than calculates the following thermochemical variables of based on the individual thermodynamic state:

- mass fractions Y_i,

- temperature T,

- density ρ (based on ideal gas equation of state),

- molecular weight M_w,

- specific heat capacity c_p.
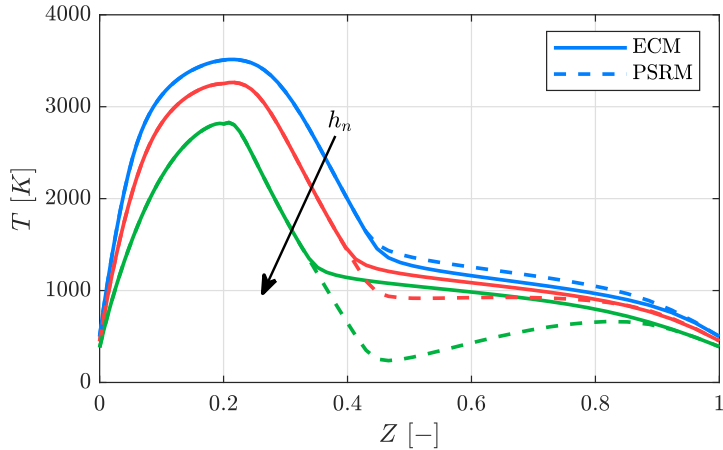
Figure 3.1: Temperature over the mixture fraction range for different values of normalized enthalpy - methane combustion.

The transport properties (viscosity μ, laminar conductivity λ, and species diffusivity D_i) are calculated employing the procedure presented in section 3.5 based on the kinetic theory of gases. The values are normalized and tabulated as described in section 3.3.1. A module is available in the in-house tool to adapt the density according to the generalized cubic equation of state for real gas applications by *Kim et al.* [84]. However, this adaption was not used in this thesis due to the high-temperature injection state in the investigated test cases.

The temperature over the mixture fraction range for different values of normalized enthalpy h_n for a typical methane combustion case is shown in Figure 3.1. The effect of the heat loss on the temperature is clearly visible. The lower the normalized enthalpy is, the lower is the temperature of the mixture. The effect is less pronounced towards the inlet conditions of both oxidizer and fuel.
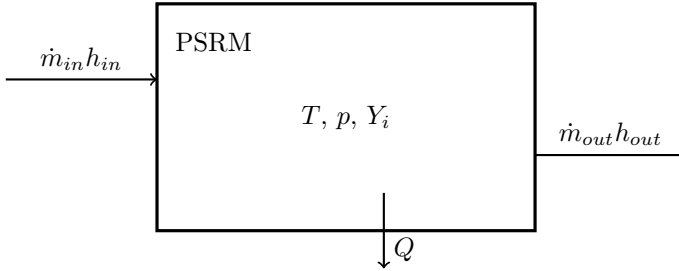
Figure 3.2: Concept of the perfectly stirred reactor model

3.3.1.2 Perfectly Stirred Reactor Model

The second combustion model for the tabulation of thermochemical variables used here is the so-called "Perfectly Stirred Reactor Model (PSRM)". The model was developed as part of this thesis to incorporate chemical kinetic effects in a tabulated chemistry method. The tool uses the open-source combustion code Cantera [85] for all chemical calculations. The basis for this method is a simplified model of a perfectly stirred reactor (or continuously stirred tank reactor). The concept of the PSRM is illustrated in Figure 3.2. The following assumptions are taken for the reactor:

1) The inlet stream is instantly mixed into the fluid in the reactor interior.

2) The fluid leaving through the outlet has the same composition and thermodynamic state as the interior

3) The flow through the reactor is steady-state, i.e. $\dot{m}_{in} = \dot{m}_{out} = \dot{m}$.

   The reactor model than calculates the temperature and composition as a function of the residence time. Here a constant pressure

reactor is used. Its governing equation is:

$$\frac{dH}{dt} = -Q + \dot{m}_{in}h_{in} - \dot{m}_{out}h_{out} \tag{3.32}$$

where H is the reactor enthalpy, $\dot{m}_{in} = \dot{m}_{out}$ is the mass flow rate, h_{in} and h_{out} are the specific enthalpy of the inlet and outlet stream respectively and Q is the heat loss through the reactor wall.

In a steady state the derivative of the reactor enthalpy becomes zero ($\frac{dH}{dt} = 0$). Using assumption 3) stated earlier ($\dot{m}_{in} = \dot{m}_{out} = \dot{m}$) and setting the mass flow rate arbitrarily to 1 kg/s Equation 3.32 can be rearranged to yield:

$$q = h_{in} - h_{out}, \tag{3.33}$$

where q is a mass-specific heat flux in the unit J/kg. The heat flux q can now be calculated based on the desired assigned enthalpy level h_{out} for which the thermochemical properties are to be tabulated. Using the equilibrium composition and the injection enthalpy of the propellants at the inlet (i.e. as h_{in}) and extracting the heat flux q from the stream in the reactor emulates the cooldown process of the exhaust gas in the post-flame. Now values progressing dependent on the residence time can be extracted from the reactor. The evolution of the composition and thermodynamic state is computed based on a detailed chemical kinetic scheme using Arrhenius expressions (discussed in section 3.3.2). The kinetic scheme used in this thesis is the 17-species, and 72-reactions skeletal mechanism by *Sankaran et al.* [86].

Figure 3.3 shows the evolution of temperature and enthalpy in a perfectly stirred reactor for a post-combustion cooldown process comparing hydrogen and methane combustion. In this simulation, the combustion gas enters the reactor inlet in a chemical equilibrium state based on the following injection conditions:

- H_2

    - $O/F = 5.85$

    - $T_{Fu} = 285$ K

    - $T_{Ox} = 280$ K

- CH_4

    - $O/F = 2.2$

    - $T_{Fu} = 270$ K

    - $T_{Ox} = 275$ K

In both cases, enough energy is extracted from the system to cool the combustion gas to 1000 K at the outlet. The temperature at the outlet is then compared to the temperature expected at chemical equilibrium. The temperature goes down to the equilibrium value for the hydrogen reactor as the enthalpy in the reactor reaches its assigned value. For the methane reactor, this is not the case. The temperature drops below the equilibrium value and stays below even as the assigned enthalpy for 1000 K is reached. This implies that the exhaust gas in the methane case is present in a composition different from the chemical equilibrium at the reactor outlet. As will be explained in more detail in section 4.4.5, the main reason for this is that the reaction kinetics suppress the recombination of CO, present in the high-temperature equilibrium state, to CO_2. The impact of this suppression on the temperature tabulated over the mixture fraction space in dependency of the normalized enthalpy h_n is shown in Figure 3.1. In comparison to the chemical equilibrium state, the gas is colder in the fuel-rich mixture fraction space for most enthalpy levels.

(a) H_2 combustion

(b) H_2 combustion

(c) CH_4 combustion
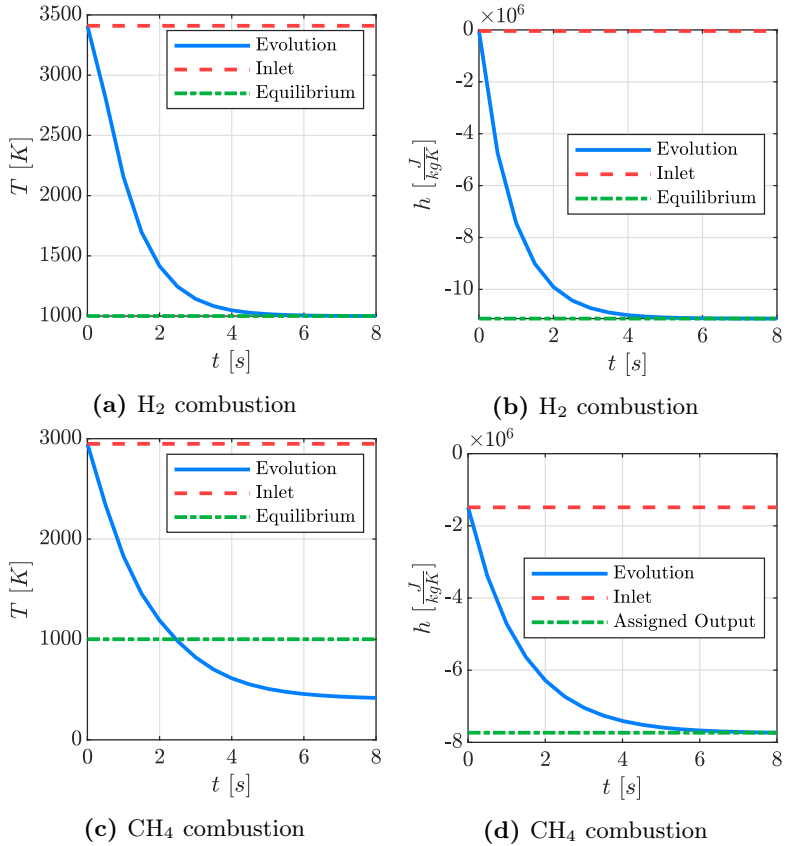
(d) CH_4 combustion

Figure 3.3: Evolution of temperature and enthalpy in a perfectly stirred reactor for a post flame cool down process comparing hydrogen and methane combustion.

3.3.2 Finite Rate Chemistry

When employing finite rate chemistry to resolve the combustion process, conservation Equation 3.5 must be solved for every appearing chemical species. Following the tabulated chemistry models, the mass diffusion coefficient is determined by assuming a unity Lewis number. The finite rate chemistry model computes the source term S_{Y_k} in Equation 3.5 by evaluating Arrhenius expressions provided in a chemical kinetic scheme.

The net production rate of the species i is then determined by the sum of the production rate of that species over all occurring reactions. It can be calculated as follows:

$$S_{Y_i} = M_{w,i} \sum_{r=1}^{N_r} \left[\left(\nu_{i,r}^{''} - \nu_{i,r}^{'} \right) \left(k_{f,r} \sum_{l=1}^{N_k} c_l^{\nu_{l,r}^{'}} - k_{b,r} \sum_{l=1}^{N_k} c_l^{\nu_{l,r}^{''}} \right) \right],$$
(3.34)

where $k_{f,r}$ and $k_{b,r}$ are the forward and backward rate constants for the rth reaction and N_r is the total number of reactions. The molecular weight is $M_{w,i}$ and c_i is the concentration of species i. Lastly, $\nu_{i,r}^{'}$ and $\nu_{i,r}^{''}$ denote the stoichiometric coefficients of species i in reaction r.

The reaction rate constants are obtained from the Arrhenius equation:

$$k_r = A_r T^{\beta_r} \exp\left(-\frac{E_{a,r}}{R_m T} \right),$$
(3.35)

where A_r is the pre-exponential factor, β_r the temperature exponent and $E_{a,r}$ the activation energy for the reaction.

The finite rate chemistry model is computationally expensive because one additional transport equation has to be solved per species in the chemical kinetic scheme. In addition, the schemes typically span a wide range of different time scales and form a set of highly non-linear, stiff equations that have to be solved in parallel to the fluid

flow calculation. This makes finite rate chemistry calculations often-
times lacking in robustness and prone to stall convergence. Additional
details on the finite rate chemistry models are provided in [63].

3.4 Thermodynamic Properties

The determination of thermodynamic properties is an integral part of
computations involving combustion chemistry. To solve the governing
equations for reacting flow, given in section 3.1, the specific heat
capacity c_p, the specific enthalpy h and the specific entropy s must
be computed by appropriate thermodynamic relations.

Here the NASA 7-coefficient polynomial representation, introduced
by *McBride et al.* [87], is used to compute the individual species
thermodynamic properties at the ideal reference state. This repre-
sentation calculates the specific heat capacity c_p with a fourth-order
polynomial. The NASA polynomials then take the following form:

$$\frac{c_p}{R} = a_1 + a_2 T + a_3 T^2 + a_4 T^3 + a_5 T^4, \tag{3.36}$$

$$\frac{h}{RT} = a_1 + \frac{a_2}{2}T + \frac{a_3}{3}T^2 + \frac{a_4}{4}T^3 + \frac{a_5}{5}T^4 + \frac{a_6}{T}, \tag{3.37}$$

$$\frac{s}{R} = a_1 ln(T) + a_2 T + \frac{a_3}{2}T^2 + \frac{a_4}{3}T^3 + \frac{a_5}{4}T^4 + a_7, \tag{3.38}$$

where a_1, a_2, a_3, a_4, a_5, a_6, and a_7 are numerical coefficients provided
in a thermodynamic data file. There are usually two sets of coeffi-
cients given, one for the low-temperature range and one for the high-
temperature range. The respective property for a multi-component
mixture is calculated as the mass fraction average of the individual
species' properties.

The underlying data for these polynomial fits typically originates
from a variety of different sources. One source is the set of JANAF

tables provided by the *National Institute of Standards and Technology* [88]. Another source is the compilation by *Burcat* [51], in which case the data is already pre-fitted in the required form. Data also is oftentimes provided in conjunction with a chemical kinetic scheme. In this case, the data for every species included in the scheme is immediately available.

However, pre-fitted data is often times associated with problems that make a refitting procedure desirable:

1. The low-temperature range is not fully covered. This is especially true for rocket engine applications, which oftentimes have at least one propellant component injected at cryogenic temperatures.

2. The high-temperature range is not fully covered. This is less often a problem but can be a factor if the temperature in the flowfield reaches an overly high temperature during the solution process. These temperatures are not necessarily physical and often not present at convergence.

3. Discontinuities can appear at the point where the low temperature and the high-temperature range connect.

These factors can cause problems for the numerical solver, as polynomials tend to diverge outside their temperature limits, and discontinuities can lead values to "jump" near the connection point. The results are stalling convergence or even solver failure.

Therefore the thermodynamic data used in this thesis is refitted. A constrained least square fitting procedure is applied in a three step process.

1. Coefficients a_1 through a_5 are determined by fitting the specific heat values to equation 3.36, with the following constraints applied:

- C^0 (continuous) $\frac{c_p}{R}$ at range mid point

- C^1 (1st derivative continuous) $\frac{c_p}{R}$ at range mid point

2. Coefficient a_6 is determined by fitting the specific enthalpy to equation 3.37 and keeping a_1 through a_5 fixed, with the following constraints applied:

   - h matches the source data at the reference point of 298 K

   - C^0 (continuous) $\frac{h}{R}$ at range mid point

   - Note that C^1 (1st derivative continuous) $\frac{h}{R}$ at range mid point is implicitly applied by the previous constraints

3. Coefficient a_7 is determined by fitting the specific entropy to equation 3.38 and keeping a_1 through a_6 fixed, with the following constraints applied

   - s matches the source data at the reference point of 298 K

   - C^0 (continuous) $\frac{s}{R}$ at range mid point

   - Note that C^1 (1st derivative continuous) $\frac{h}{R}$ at range mid point is implicitly applied by the previous constraints

An overview of the polynomial fits used in this thesis is given in Appendix A. It should also be noted that the program developed for this thesis has the capability to produce polynomials in the NASA 9-coefficient representation, introduced by *McBride et al.* [89], in addition to the NASA 7-coefficient polynomial representation. This implementation was included to guarantee compatibility and comparability of the thermodynamic data with the rocket analysis codes CEA [82] and THERMTEST [5] used at the RFA.

3.5 Transport Properties

It is necessary to calculate the transport properties of the fluid mixture to evaluate the diffusive fluxes of momentum, energy, and species in the governing equations. For the momentum equation, a relation for the laminar viscosity μ is needed; for the energy equation, a relation for the laminar conductivity λ is needed, and for the species equation, a value for the laminar diffusivity D_i of each individual species i is needed. Empirical correlations typically describe these quantities.

While the turbulent diffusive flux mostly outweighs the laminar diffusive flux in the core flow, laminar transport phenomena become important in the near-wall region where viscous forces are dominant. As pointed out by *Ivancic et al.* [71], this is of particular importance in heat transfer analysis because the predicted wall heat flux directly scales with the laminar fluid mixture conductivity.

The laminar viscosity μ is calculated temperature- and composition-dependent in this thesis. A relation according to the molecular theory of gases at low density is used. As presented by *Bird et al.* [52], for a single component species, the viscosity is then given by:

$$\mu_i = 2.6693 \cdot 10^{-6} \frac{\sqrt{M_{w,i}T}}{\sigma^2 \Omega_\mu}, \tag{3.39}$$

where $\Omega_\mu(T^*)$ is the collision integral for viscosity, which depends on the reduced temperature $T^* = T/(\varepsilon/k_b)$. The values σ and ε/k_b are the Lennard-Jones parameter, given in Table B.1 in Appendix B.

The viscosity of the multi-component mixture is determined according to the semi-empirical mixing rule by *Wilke* [90]:

$$\mu = \sum_i \frac{x_i \mu_i}{\sum_j x_j \Phi_{ij}}, \tag{3.40}$$

where the dimensionless quantities Φ_{ij} are defined as:

$$\Phi_{ij} = \frac{\left[1 + \left(\frac{\mu_i}{\mu_j}\right)^{1/2} \left(\frac{M_{w,j}}{M_{w,i}}\right)^{1/4}\right]^2}{\left[\left(1 + \frac{M_{w,i}}{M_{w,j}}\right)\right]^{1/2}}. \tag{3.41}$$

The laminar conductivity λ for a single species is calculated by the semi-empirical method for polyatomic gases at low density developed by *Eucken* [91]:

$$\lambda_i = \frac{15}{4} \frac{R_m}{M_w} \mu \left(\frac{4}{15} \frac{c_p M_w}{R_m} + \frac{1}{3}\right). \tag{3.42}$$

The same mixing rule (Equation 3.40) is applied as was for the viscosity to compute the composition-dependent thermal conductivity for the mixture. The coefficients Φ_{ij} are identical to those in the viscosity equation.

The laminar species diffusivity D_i is calculated by assuming unity Lewis numbers for all species in the mixture. The single species Lewis number is defined as:

$$Le_i = \frac{k_i}{\rho c_p D_i}. \tag{3.43}$$

Note that k_i and D_i are component values, while ρ and c_p are associated with the overall mixture. Taking unity Lewis numbers for all species implies that the species diffusivity scales according to the species conductivity.

4 Combustor Analysis

In the following chapter, the flow and combustion processes in a single-element rocket combustor are studied numerically. Different modeling approaches for simulating the turbulence and chemical reactions in the combustor flow field are compared. Simulations were performed for hydrogen/oxygen and methane/oxygen hot firing tests at a nominal pressure of approximately 20 bar. The applicability of the different modeling approaches concerning the two propellant combinations is investigated, and the findings are discussed.

In-house test data from the TUM mobile rocket combustor test bench MoRaP is used for the validation of the numerical models. The advantage is that the experimental results for the different fuel types are available from the same combustor test bench (including the same injector element) and measurement setup.

First, in section 4.1, the experimental setup of the MoRaP test bench is described, including the measurement equipment. Then the results from different hot firing tests are presented in section 4.2. They are analysed and discussed in section 4.2.

Subsequently the results of the numerical investigations are presented in section 4.4. Sections 4.4.2 and 4.4.3 are dedicated to turbulence modeling approaches and turbulence modeling parameters respectively. Combustion modeling is discussed in section 4.4.5.

4.1 Test Setup

The rocket combustor, which is studied here numerically, was designed and experimentally investigated at the Technical University of Munich (TUM). It is called Mobile Rocket Test Bench (Mobiler Raketenprüfstand) (MoRaP), which is short for mobile rocket combustor test bench in German. The experiments were conducted within the research program SFB-TRR40 "Technological Foundations for the Design of Thermally and Mechanically Highly Loaded Components of Future Space Transportation Systems" [10].

The performed investigations are part of a larger effort to define heat transfer characteristics and injector design criteria for rocket engines and support the verification and validation of numerical tools in the field of rocket combustion analysis. Details on the experimental setup are reported by *Silvestri* [47]. Here only an overview of the most important features of the experiment is given. The overview focuses on the parts relevant to numerical simulations.

Figure 4.1 shows a CAD model of the TUM round single-element combustor assembly, which can be installed onto the MoRaP. A modular approach was taken in the design of this combustion chamber. The assembly is divided into an injector head, an igniter segment, a nozzle segment, and three chamber segments.

The combustion chamber is lab-scale, with a length of 305 mm. It has a circular cross section to simplify the flow field and enable an axisymmetric analysis of the design. The inner diameter is 12 mm, and the throat diameter of the convergent-divergent nozzle segment is 7.6 mm. This leads to a contraction ratio of 2.5, a value in the range of actual flight hardware, see table 2.2. Therefore a Mach number representative for liquid rocket engines can be expected inside the chamber. With a characteristic length of the assembly of 0.75 m, the combustor is likely to have a high combustion efficiency,
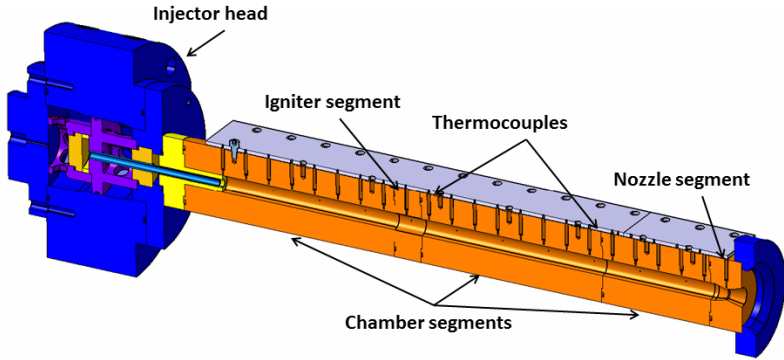
Figure 4.1: CAD model of the MoRaP round single-element combustor.

see section 2.6. The chambers geometric characteristics are compiled in table 4.1.

Table 4.1: Geometric characteristics of the MoRaP single-element round combustor.

Combustor length	[mm]	305
Combustor diameter	[mm]	12
Contraction ratio	[-]	2.5
Expansion ratio	[-]	3.1
Characteristic length	[m]	0.75

A schematic overview of the injector head design is given in figure 4.2. Fuel and oxidizer enter their respective manifolds in gaseous form. Their mass flow rates are regulated via critically flowed orifices. Porous plates are used to homogenize the injection conditions in terms of temperature, pressure, and velocity profile. They also decouple the feed system from the injection system by providing a pres-
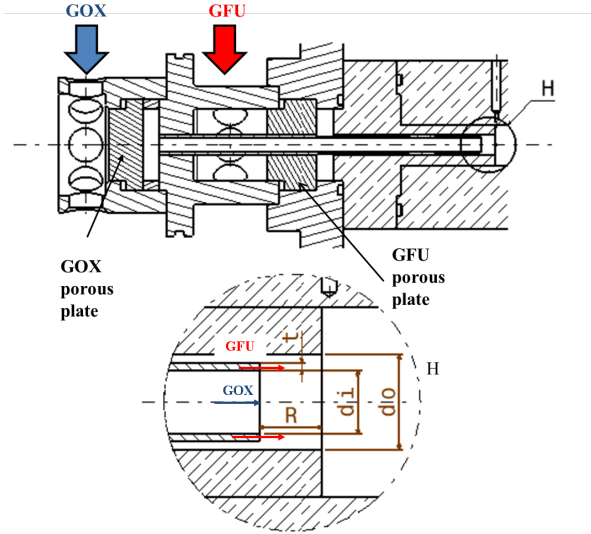
Figure 4.2: Injector schematic of the MoRaP round single-element combustor.

sure drop. The propellants enter the combustion chamber through a single shear-coaxial injector element in line with the symmetry axis of the combustor. As is typical for these injector types, the oxidizer is injected through a central tube, called the oxidizer post. The fuel is injected via the surrounding annulus. The oxidizer post has an inner diameter of 4 mm and a thickness of 0.5 mm. The outer diameter of the fuel annulus is 5 mm. In the investigated configuration, the oxidizer post tip is flush-mounted with the faceplate. Data with different recess variations is available from the publication of *Silvestri et al.* [92].

The combustion chamber is a heat sink design made of oxygen-free high conductivity copper, i.e. it is capacitively cooled only. The wall temperatures are measured using spring-loaded thermocouples

distributed in clusters of three along the length of the chamber. In a single cluster, the thermocouples are spaced 1, 2, and 3 mm from the hot gas side of the combustor wall. This is done to reconstruct the heat flux from the thermocouple readings. To accomplish this an inverse heat transfer method developed at the TUM [93, 94, 95] is used.

The pressure in the chamber is measured with equally spaced static pressure transducers distributed along the wall. The data from the transducers can give valuable information about the evolution of the combustion and can be used for the determination of the combustion efficiency. Due to the heat release of the combustion process, the hot gas mixture accelerates, and the pressure in the chamber drops in the axial direction towards the nozzle segment. The curvature of the axial pressure profile is a direct consequence of the progress of the combustion progress. The possibility to compare the numerically predicted pressure evolution to the experimental one separates this test case from other test cases found in literature [12, 96, 31], where pressure is only measured globally in a single location.

4.2 Test Data

The test data available for selected operating points from the MoRaP round single-element combustor hot firings is presented in the following section. An operating point is characterized by the nominal combustion pressure and the oxidizer to fuel ratio (or mixture ratio) of the propellants. The pressure and the mixture ratio are linked to the propellant mass flow rates by the equations 2.4 and 2.3. Note that the determination of the expected nominal combustion pressure is discussed in section 4.3.

Table 4.2 summarizes the experimental operating conditions for five different test cases. The temperatures of the fuel and oxidizer en-
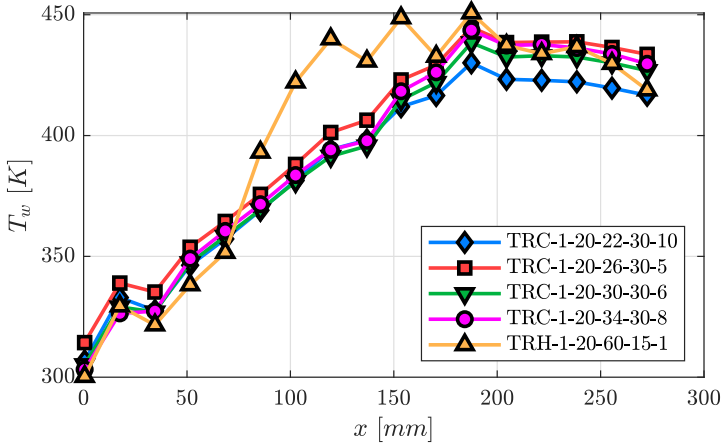
Figure 4.3: Measured wall temperatures for selected MoRaP round single-element combustor test cases.

tering the combustion chamber determine the overall energy content of the system at injection. In addition to four methane combustion tests, a test using hydrogen as a fuel is included in the table. Modeling approaches for the simulation of both propellant combinations' performance and heat transfer characteristics are investigated in the following sections using validation data from two selected cases of these hot firing tests.

Figure 4.3 shows the measured wall temperatures for all thermocouples with a distance of 1 mm from the combustor wall. These are used as boundary conditions for the CFD simulations involving heat transfer. They are applied directly to the hot gas wall side, and their values are linearly interpolated in the cylindrical part of the chamber. In the nozzle, the temperature measurement of the nearest thermocouple is applied, as no reliable data was available at this location.

Table 4.2: Selected operating points of the MoRaP single-element round combustor.

Case reference	Fuel	$\dot{m}_{Fu}$ $[g/s]$	$\dot{m}_{Ox}$ $[g/s]$	$\dot{m}$ $[g/s]$	O/F $[-]$	T_{Fu} $[K]$	T_{Ox} $[K]$
TRC-1-20-22-30-10	Methane	15.268	33.889	49.157	2.22	268	276
TRC-1-20-26-30-5	Methane	13.298	35.062	48.360	2.64	269	275
TRC-1-20-30-30-6	Methane	12.096	36.270	48.366	3.00	270	274
TRC-1-20-34-30-8	Methane	11.327	38.644	49.971	3.41	271	273
TRH-1-20-60-15-1	Hydrogen	5.648	33.016	38.664	5.85	285	280
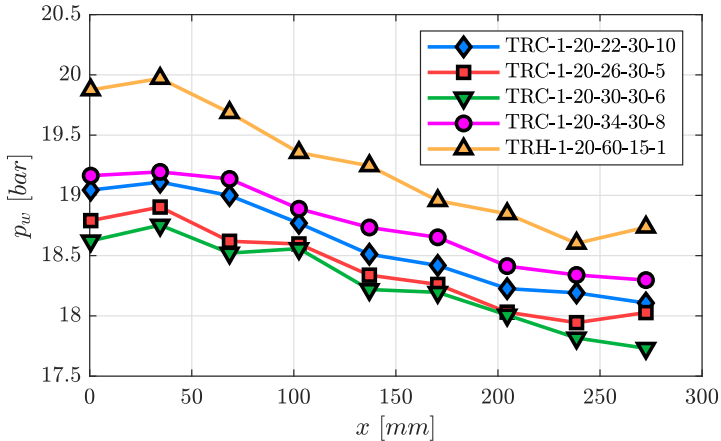
Figure 4.4: Measured wall pressure for selected MoRaP round single-element combustor test cases.

Figure 4.4 shows the wall pressure measurements of the static pressure transducers along the combustor walls. In all CFD simulations, the wall pressure is an outcome and used to validate the numerical model. The measurements are also used to determine the nominal combustion pressure and calculate the experiments' combustion efficiency.

Figure 4.5 shows the experimental wall heat fluxes, which have been reconstructed from thermocouple readings by inverse heat transfer calculations. The wall heat flux is an outcome of all CFD simulations and is used to validate the numerical model. In addition, it is employed as input in the combustion efficiency correction presented in section 4.3. No experimental data is available for the values in the nozzle throat.

No measurement error is given for the investigated test cases, neither for the temperature nor the pressure measurements. While the
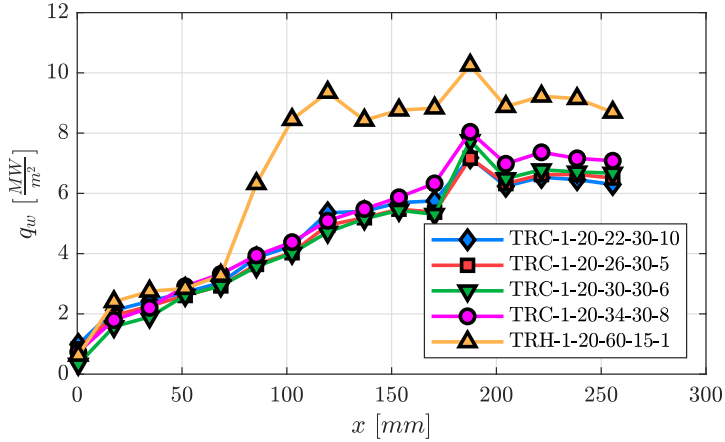
Figure 4.5: Reconstructed wall heat flux for selected MoRaP round single-element combustor test cases.

surface temperature detection is comparatively simple, the reconstruction of the heat flux is substantially more difficult. *Suslov* [97] collected the typical measurement errors from different authors and experiments as a function of heat flux. This relation is shown in Figure 4.6. It can be seen that the measurement error increases significantly with higher heat flux values. With plateau values of approximately $q_{w,c} = 7...9$ MW/m^2 in the cylindrical part of the chamber, the peak value in the throat can be estimated using a Nusselt correlation. As reported by *Sinjarev* [7] the throat heat flux scales with the contraction ratio according to $q_{w,th} = q_{w,c} \cdot \varepsilon_c^{0.91}$. Therefore, with a contraction ratio of 2.5, a peak heat flux of $q_{w,th} = 16...20$ MW/m^2 can be expected. A measurement error of around 14 % is a reasonable assumption for the here presented experimental data. The much more precise pressure measurements are assumed to have a maximum error of 3 %. These values are taken into account
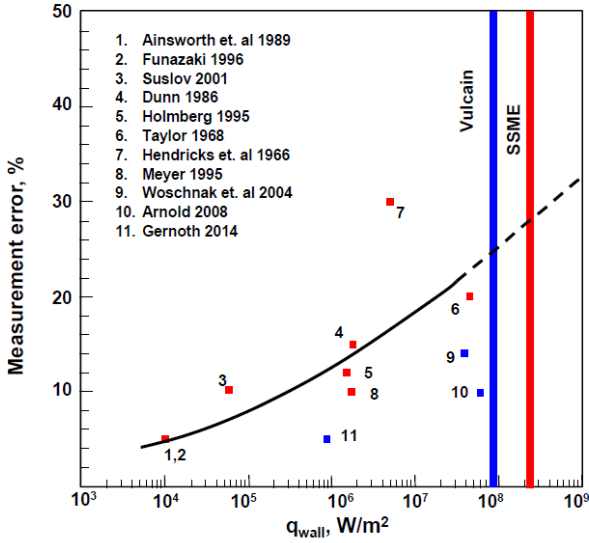
Figure 4.6: Typical measurement error as function of the wall heat flux (from *Suslov* [97]).

when comparing the experimental data to the values predicted by the numerical simulations.

4.3 Performance Analysis

In this section, the experimental performance of the MoRaP round single-element combustor is analyzed. This is accomplished by comparing the theoretical, ideal performances to the measured ones. To analyze the theoretical performance of the combustor at the discussed operating points, the expected pressure at the measured mass flow rate is evaluated together with the ideal characteristic velocity of the system. The values are compared to the values measured in the hot-

firing test. The combustion efficiency is then calculated according to equation 2.6.

The ideal values for characteristic velocity and chamber pressure are calculated using NASA's Chemical Equilibrium with Applications (CEA) code [82]. CEA calculates theoretical rocket performance parameters under the following assumptions:

- One-dimensional flow field in the combustor

- Zero velocity at the combustion chamber inlet

- Complete combustion

- Adiabatic combustion

- Isentropic expansion in the nozzle

- Homogeneous mixing

- Ideal gas law

- No temperature and no velocity lag between condensed and gaseous species

Note that CEA does not take mass flow rates as input since most performance parameters are mass-specific and can be scaled later. A method, which iterates the pressure at the injection point in CEA until equation 2.4 yields the experimentally measured mass flow rate, was implemented to circumvent this problem.

The experimental values for characteristic velocity and chamber pressure are calculated using the so-called simplified JANNAF method according to the *JANNAF Working Group* [98]. This involves a second iterative calculation with CEA. This time the pressure at the combustion endpoint in CEA is matched to the measured pressure of the last pressure transducer in the experiment before the nozzle.

The calculated performance values of the experimental combustor at the discussed operating points are summarized in table 4.3.

One of the assumptions of the calculation of theoretical rocket performance in CEA is adiabatic combustion. This is a reasonable assumption for large-scale rocket engines, such as launcher primary or upper stages. In large-scale engines, the heat loss through the combustor wall is only a fraction of the injected energy, as shown in figure 4.7. It will, therefore, not significantly reduce the combustion temperature. When dealing with substantial heat loss, however, this assumption is no longer valid. The thermal energy lost to the wall does not increase the chamber pressure anymore, and the combustion efficiency decreases. Figure 4.8 shows the influence of the heat loss to the wall on the combustion efficiency for different percentages of heat loss. Here $\Delta\eta_{c*}$ is the difference in combustion efficiency comparing adiabatic values to values including a heat loss correction. The heat loss fraction Ξ is taken as a percentage of the reaction enthalpy of the chemical system. For the experimental data, this is taken into account by subtracting the integrated heat flux up to the throat from the injection enthalpy of the propellants when calculating the ideal characteristic velocity. This results in the non-adiabatic combustion efficiency $\eta_{c*,h}$ given in table 4.3. For the investigated methane test cases, the combustion efficiency decrease is indicated in figure 4.8. The thermal wall losses are in the range of 16%, resulting in an efficiency loss of 3.5-6% depending on the mixture ratio.

4.4 Numerical Investigation

In this section, the MoRaP round single-element combustor is investigated numerically. First, a grid convergence study is presented to quantify the discretization error. Second, the modeling of the turbulent processes is discussed. This includes the comparison of different

Table 4.3: Performance parameters of the MoRaP single-element round combustor.

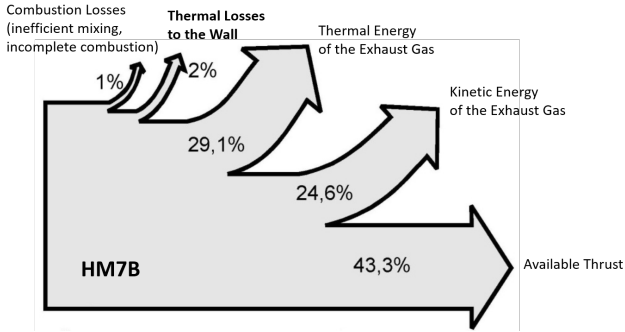| Case reference	$p_{c,id}$ [bar]	$p_{c,id,h}$ [bar]	$p_{c,exp}$ [bar]	c^*_{id} [m/s]	$c^*_{id,h}$ [m/s]	c^*_{exp} [m/s]	η_{c^*} [%]	$\eta_{c^*,h}$ [%]
TRC-1-20-22-30-10	20.22	19.00	18.76	1866	1753	1731	92.8	98.7
TRC-1-20-26-30-5	20.17	19.28	18.66	1892	1809	1751	92.5	96.8
TRC-1-20-30-30-6	20.01	19.31	18.35	1876	1811	1721	91.7	95.0
TRC-1-20-34-30-8	20.29	19.62	18.93	1842	1781	1719	93.3	96.5
TRH-1-20-60-15-1	19.96	19.10	19.39	2341	2241	2275	97.2	101.5

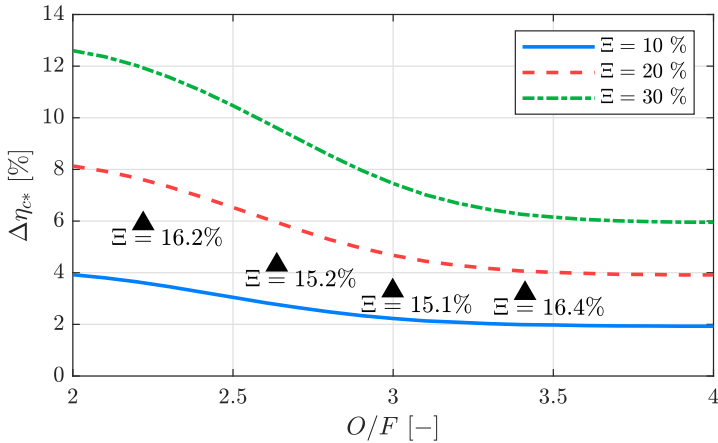**Figure 4.7:** Thermal budget of the HM7B thrust chamber (modified from *Suslov* [97]).

Figure 4.8: Influence of the thermal losses to the wall on the combustion efficiency for different mixture ratios - methane combustion.

turbulence models as well as a sensitivity analysis on turbulence modeling parameters. Third, the modeling of the combustion process is discussed. Different combustion models are applied, and their suitability concerning the used propellant combination is analyzed.

4.4.1 Grid Study

A grid convergence study was conducted to examine the dependence of the numerical solution on the spatial resolution of the computational grid and quantify the discretization error. For this purpose, simulations on two successively finer grids were performed. Table 4.4 compiles the critical parameters of the generated grids. The fine grid consists of 91735 control volumes and the medium grid of 54189. The fine grid, which is subsequently used for all combustor simulations following the grid study, has a maximum axial cell length of 2 mm and a maximum radial cell length of 0.2 mm. The wall nearest cell height in the injector is 3.33 μm in the injector and 0.33 μm in the cylindrical part of the combustor.

Table 4.4: Key parameters of the computational grids.

		Medium grid	Fine grid
Number of control volumes	[-]	54189	91735
Max. axial cell length	[mm]	2.5	2
Max. radial cell length	[mm]	0.3	0.2
Wall nearest cell height injector	[μm]	4.33	3.33
Wall nearest cell height chamber	[μm]	0.43	0.33

Figure 4.9 shows a representative overview of the numerical grid in the critical near-injector and throat region of the computational domain. Note that the figure's cell density was reduced to visualize
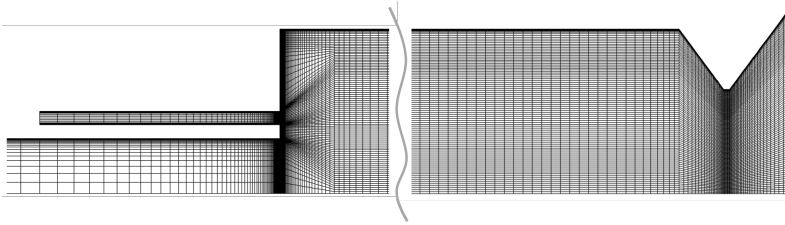
Figure 4.9: Numerical grid for the MoRaP single-element round combustor.

the grid's features better. The oxidizer post and the fuel annulus are both represented in the grid. They are both fully resolved, i.e. their cell heights are chosen small enough to prevent the necessity to use wall functions. This is done to get an accurate velocity profile at the faceplate entrance to the combustor, where the oxidizer and fuel stream begin to mix. The differing cell heights coming from the inlets are then smoothed to have as many as possible equidistant cells in the radial direction in the combustor's cylindrical part.

Simulations were performed on all grids with three different numerical discretization schemes with increasing order of formal accuracy. The employed schemes were:

- 1st Order Upwind Scheme

- 2nd Order Upwind Scheme

- 3rd Order MUSCL Scheme

The numerical background of these schemes is presented in [63].

To estimate the discretization error, i.e. the difference between the converged solution on a specific grid and the "exact" solution, the grid convergence index (GCI) according to the procedure proposed by *Roache* [99] is evaluated. The method is based on comparing

solutions on each grid to the solution determined by Richardson extrapolation [100], which is calculated as

$$\phi_{ext} = \frac{r^p \phi_{fine} - \phi_{medium}}{r^p - 1}, \tag{4.1}$$

where ϕ_{ext}, ϕ_{fine} and ϕ_{medium} are the extrapolated solution, the solution on the fine grid, and the solution on the medium grid, respectively. The variable r is the refinement factor, and p is the apparent order of the method.

The integral wall heat flux over the entire combustion chamber is used to judge the global grid convergence. Table 4.5 comprises the simulation results on the different grids and for all applied discretization methods together with the GCI.

Table 4.5: Estimation of the discretization error.

	Grid	1st O.	2nd O.	3rd O.
	m	92.9	97.1	97.1
$\dot{Q}$ [kW]	f	94.2	97.7	97.6
	ext	98.6	98.0	97.6
GCI [%]	m	24.2	4.6	3.7
	f	7.8	1.1	0.7

4.4.2 Turbulence Modeling Study

The Reynolds number in the cylindrical part of the combustion chamber is around $4.4 \cdot 10^4 ... 5.3 \cdot 10^4$ for the methane test cases and $3.8 \cdot 10^4$ for the hydrogen test case. The flow inside the combustor is therefore highly turbulent. This makes using an appropriate turbulence model necessary to accurately predict the mixing and combustion processes driven by the turbulence in the fluid flow.

Four different turbulence models are assessed as part of this thesis. Two of the four include user-developed model extensions that improve their performance. The following section presents the simulation results obtained with these models for the MoRaP round single-element combustor and compares them to find the most suitable model. Section 3.2 presents the theoretical background to these models.

Two of the four models belong to the k-ε family, and the other two belong to the k-ω family. All models are two-equation models, i.e. they include two additional transport equations to calculate the turbulent viscosity μ_t. They all transport the turbulent kinetic energy k as the first variable. Models of the k-ε family transport the turbulent dissipation ε as the second variable, while models of the k-ω family transport the *specific* turbulence dissipation rate ω. The first variable determines the energy of the turbulence in the flow, whereas the second variable determines the scale of the turbulence (length-scale or time-scale).

Typically k-ε type models are said to give good predictions in the high Reynolds number free stream and are insensitive to the assumed free stream boundary conditions. However, special treatment is necessary to achieve good performance for wall-bounded flows. Models of the k-ω type are suitable in the low Reynolds number region near the wall but tend to be dependent on the assumed free stream value of ω [55].

The two models of the k-ε family used here are the low Reynolds model by *Abe et al.* [64], which employs damping functions in the wall near region to calculate the turbulent viscosity, and a standard two-layer model blending with the one-equation model by *Wolfshtein* [62]. The two models of the k-ω family are the standard model by *Wilcox* [68] and the SST model by *Menter* [70]. The k-ω SST model is a hybrid approach between k-ε and k-ω, which tries to mitigate the drawbacks of the standard approaches for both families and

combine their advantages.

For all test cases, the models of the k-ε family show significantly better results than the ones of the k-ω family. This is true for the prediction of the experimental data as well as the convergence behavior. In some cases, for the k-ω family models, it was challenging to arrive at a converged solution. This made it necessary to run simulations with low under relaxation factors. The following section presents the simulation results for the MoRaP round single-element hydrogen test case. The results for the methane test cases are qualitatively the same. Therefore only an overview of the most important predictions is given at the end of this section.

Figure 4.10 shows the temperature fields, including the stoichiometric isoline and the turbulent viscosity fields overlaid with streamlines for all four turbulence models. The flow field is qualitatively similar, with a counter-rotating corner vortex is visible near the faceplate. The vortex size is largely independent of the choice of the turbulence model. The predicted flame length, indicated by the stoichiometric line (i.e. an isoline indicating the location of the stoichiometric mixture ratio ($O/F_{st,H_2} = 8$)) is influenced heavily by the turbulence model. While the flame length is around 115 mm for the models of the k-ε family, it is 260 mm for the k-ω SST model. For the standard k-ω model, the flame front does not cross the combustor axis inside the chamber, and the reaction zone extends through the combustor exit. This leads to a substantial amount of oxygen leaving the chamber unburned. The radial expansion of the flame is similar in all cases.

The fuel and the oxidizer enter the combustion chamber in distinct streams. This leads to a non-premixed flame. The heat release in the combustion zone is then directly coupled to the mixing of the propellants. Since the flow is of a high Reynolds number, turbulence dominates the mixing process, and its prediction depends on
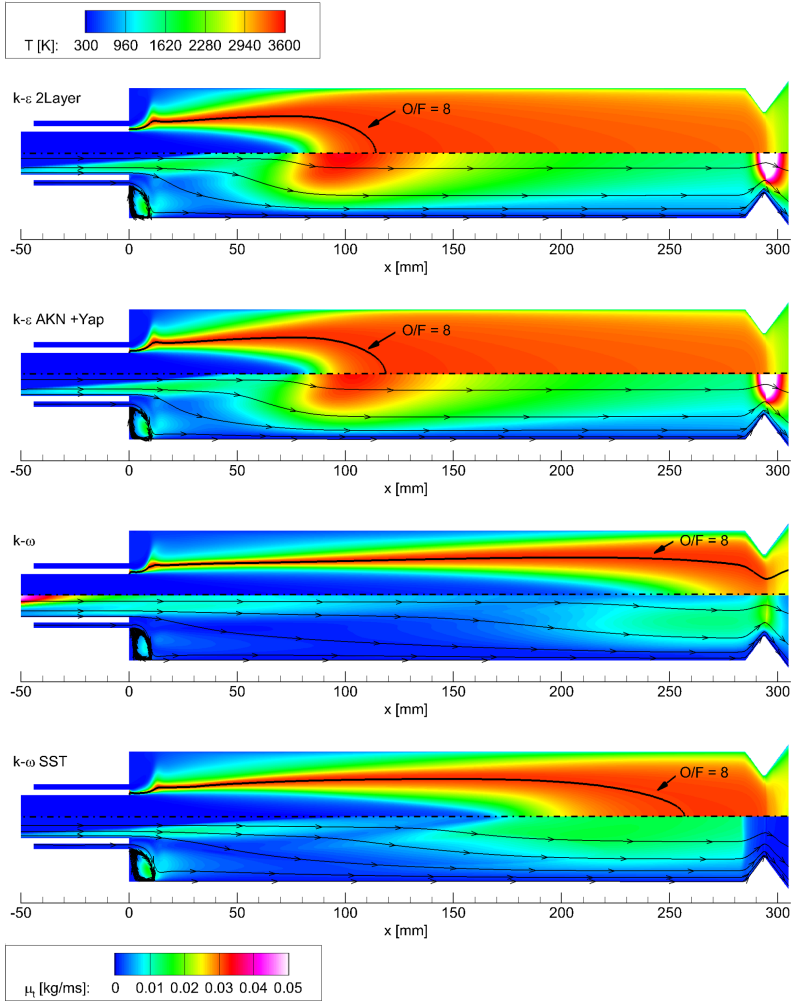
Figure 4.10: Influence of the turbulence model on the predicted temperature (upper half; including stoichiometric isoline) and turbulent viscosity fields (lower half; including streamlines) - hydrogen test case ($O/F = 5.9$).
(Plot is in non-scale division x/y = 0.2).

the turbulence model employed.

Here the so-called "unmixedness" is used for the quantification of the predicted mixing quality. The unmixedness is defined as

$$U = \frac{\bar{Z'^2}}{\bar{Z}(1 - \bar{Z})} \text{ with,} \tag{4.2}$$

$$\bar{Z'^2} = \frac{\sum_i^n (\bar{Z} - Z_i)^2}{n}, \tag{4.3}$$

where $\bar{Z}$ is the cross-sectional average of the mixture fraction, Z_i is the local mixture fraction at a point i in the cross-section and Z' is the variance of the local mixture fraction.

The unmixedness is a normalized quantity, which characterizes the deviation from the fully mixed state at every cross-section of the combustor. A value of one implies a distinct state of oxidizer and fuel. A value of zero implies the propellants are mixed locally, i.e. they are present at the injection mixture ratio at every point in the cross-section.

Figure 4.11 shows the axial evolution of the unmixedness for the investigated turbulence models. A significant discrepancy exists between the models of the k-ε family and the k-ω family. Both ε based models predict of fully mixed state at approximately $x = 150$ mm. The unmixedness drops rapidly for $x < 100$ mm and then asymptotically declines towards zero. The standard k-ω does not lead to a fully mixed state at all, and the k-ω SST model predicts a very late conclusion of the mixing process at approximately $x = 275$ mm. Both ω based models show a more steady decline along the chamber axis with no distinct inflection point.

The reason for the deviation between the turbulence models is evident from the predicted turbulent viscosity fields shown in Figure 4.10. Both ε based models generate a region of high turbulence in the first half of the chamber. In this region, fuel and oxidizer
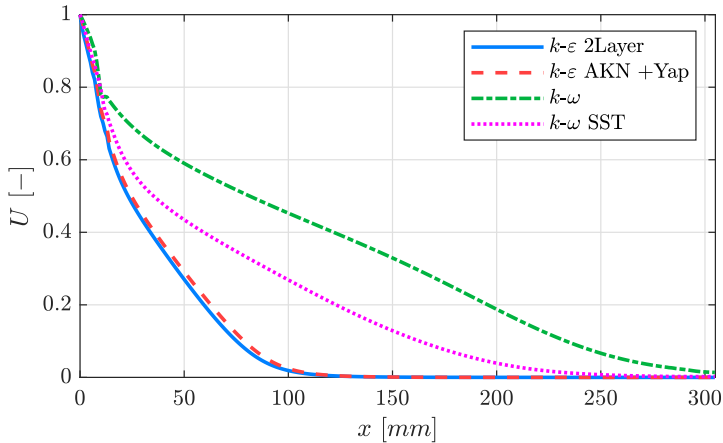
Figure 4.11: Influence of the turbulence model on the axial evolution of the unmixedness - hydrogen test case ($O/F = 5.9$).

are mixed rapidly and combusted by the turbulent flow. The onset of this region is shifted downstream for both ω based models. The magnitude and extent of the high turbulent viscosity range also are significantly lower. This causes slower and weaker mixing progress and a lengthening of the flame front.

The choice of the turbulence model and consequently the predicted mixing quality also directly impacts the prediction of the validation data, i.e. the wall heat flux and the axial pressure distribution. The influence is shown in in Figure 4.12 and Figure 4.13 respectively. The k-ω based models underestimate the turbulent mixing in the early shear layer, leading to a low heat release rate. This leads to an underpredicted heat flux in the first half of the cylindrical chamber part. Subsequently, the heat flux rises gradually to a level above the experimental data towards the nozzle. The test data indicates the end of combustion by the peak heat flux at around $x = 120$ mm
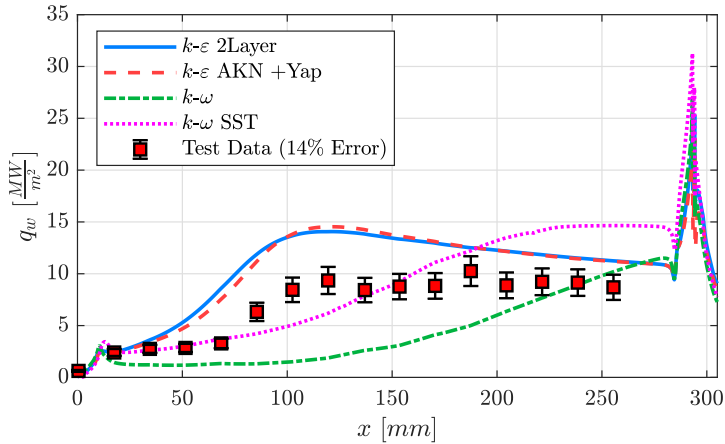
Figure 4.12: Influence of the turbulence model on the predicted wall heat flux - hydrogen test case $(O/F = 5.9)$.

and the flattening of the pressure curve at the same location. The simulations employing either of the k-ω based models quite clearly do not predict the same qualitative trend. The k-ε based models show a good qualitative agreement with the data from the hot firing tests. For the low Reynolds model by *Abe et al.* this was achieved by implementing the so-called Yap-correction [65], as suggested by *Riedmann* [46].

Figure 4.14 shows the influence of the Yap-correction on the wall heat flux. When the Yap-correction is employed, the low Reynolds model by *Abe et al.* is in good agreement with the two-layer k-ε model. The additional source term in the ε equation, defined in section 3.2.2, prevents the over-prediction of turbulent kinetic energy for the low-Reynolds model. This leads to a lower predicted turbulent heat transfer to the combustor wall and a lower wall heat flux. There is only a minor influence of the Yap-correction on the two-layer model.
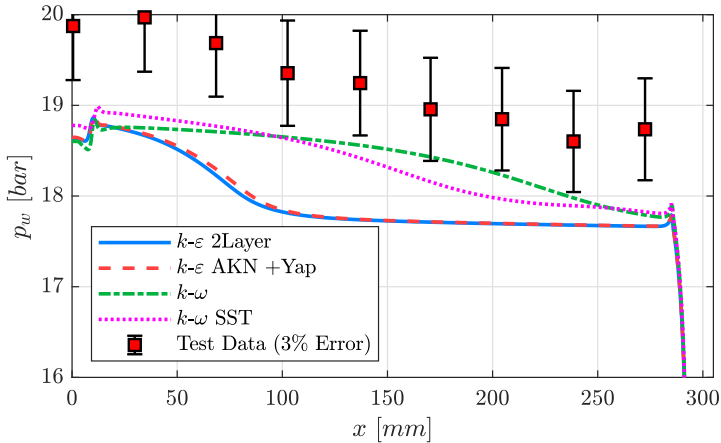
Figure 4.13: Influence of the turbulence model on the predicted wall pressure - hydrogen test case ($O/F = 5.9$).

Due to the excellent performance in qualitatively predicting the wall heat flux and the wall pressure distribution, the two-layer k-ε model is used in all further calculations. It was chosen over the low Reynolds model by *Abe et al.* as it showed a better convergence behavior.

The quantitative prediction of the simulations still needs improvement. However, when looking at Figures 4.12 and Figure 4.13, the underestimation of the wall pressure by the ε based models can be at least partly recovered when the heat flux is reduced, and the energy currently leaving the combustor is kept in the flow to raise the pressure level. This is not true for the predictions by the ω models. Here pressure and heat flux are underestimated due to the poor prediction of the mixing quality.

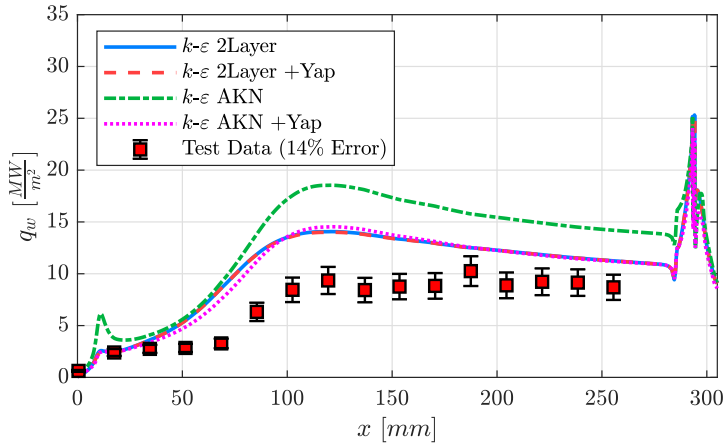All simulations in this section have been performed using a turbu-

Figure 4.14: Influence of the Yap-correction on the predicted wall heat flux - hydrogen test case ($O/F = 5.9$).

lent Prandtl number of 0.9 and a turbulent Schmidt number of 0.6. The influence of these parameters is investigated in the following section.

All previous simulations shown have also been performed for the methane test case with a mixture ratio of 2.2. The results for the wall heat flux and the wall pressure distribution are shown in Figure 4.15 and Figure 4.16 respectively. The predictions follow the same qualitative trend as the ones for the hydrogen case. Therefore, the previously drawn conclusions remain.

4.4.3 Turbulence Modeling Parameter Study

As described in section 3.2, unclosed terms appear in the governing equations of fluid flow when turbulence is modeled using a RANS approach. These terms represent the transfer of a given quantity (e.g. momentum, energy, or species) due to the turbulent fluctuations in
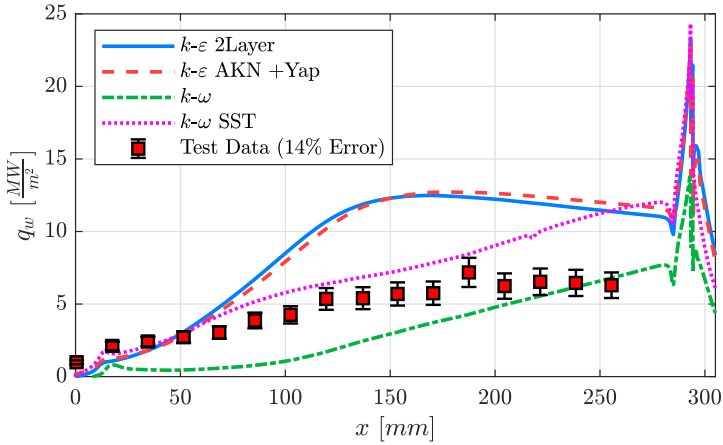
Figure 4.15: Influence of the turbulence model on the predicted wall heat flux - methane test case ($O/F = 2.2$).
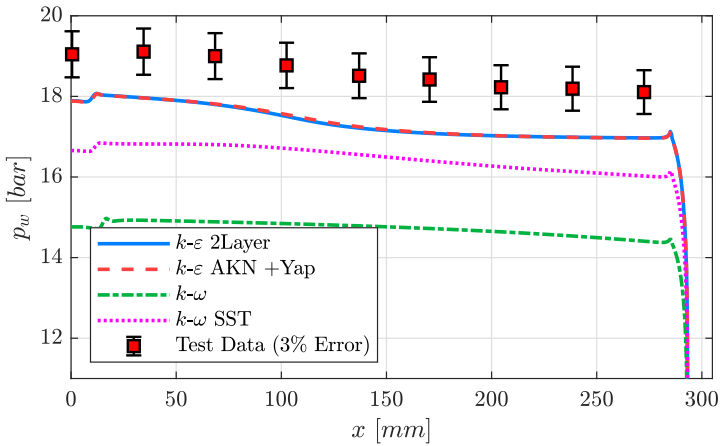

Figure 4.16: Influence of the turbulence model on the predicted wall pressure - methane test case ($O/F = 2.2$).

the fluid flow. They can significantly impact the prediction of the heat transfer and performance in a rocket combustor because turbulence is an essential mode of transport. This is especially true normal to the streamlines of the velocity field because the convective transport is less dominant in this direction. The terms are closed here by a gradient diffusion approach, which introduces a relation between the respective transported quantity and its local gradient in the flow field. This causes an effective mixing of the quantity resembling a diffusive flux.

The two-layer k-ε model discussed in section 3.2.2.1 is applied to determine the diffusion coefficient for the closure of the momentum equation. This approach leads to two additional transport equations, which need to be solved. Typically, for quantities other than momentum, no additional transport equations are added. The assumption is that the turbulent diffusion coefficient is similar to the one calculated for the momentum. This assumption is based on the fact that the same underlying physical process (turbulent fluctuation) is responsible for effectively mixing all quantities. The influence of this modeling assumption is investigated in the following section by a sensitivity analysis varying the turbulent Prandtl and the turbulent Schmidt number introduced in section 3.2.1.

First, the turbulent Prandtl number is varied, while the turbulent Schmidt number is kept constant at a value of 0.6. The turbulent Prandtl number characterizes the ratio between the turbulent transport of momentum and the turbulent transport of energy. Its definition is given in equation 3.10 and repeated here for convenience:

$$Pr_t = \frac{\mu_t \bar{c}_p}{\lambda_t}.$$

The turbulent Prandtl number appears in the energy balances, equation 3.3 and equation 3.4 as part of the turbulent fluxes defined
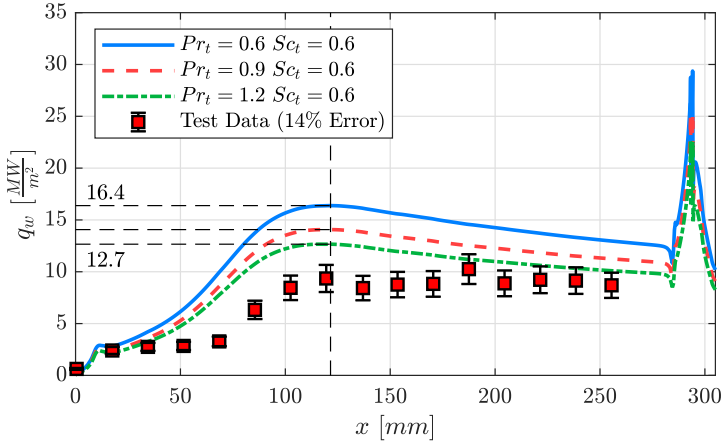
Figure 4.17: Influence of the turbulent Prandtl number on the pre-
dicted wall heat flux - hydrogen test case ($O/F = 5.9$).

by equation 3.9. From the definition of the turbulent Prandtl num-
ber, the turbulent heat conductivity can be calculated. It describes
the transport of heat due to the turbulent motion of the fluid. An
increase in the turbulent Prandtl number leads to a decrease in the
turbulent heat conductivity and a lower turbulent energy transport.

Figure 4.17 shows the influence of the turbulent Prandtl number on
the predicted wall heat flux. Increasing the turbulent Prandtl number
leads to a decrease in the wall heat flux over the whole chamber. This
is because less heat is transported along the temperature gradients
normal to the wall. The peak heat flux in the cylindrical chamber
part remains in its location, but its value decreases 22.5 % when going
from a Prandtl number of 0.6 to 1.2. The lower wall heat flux means
that less energy is leaving the system. This energy is now contributing
to the pressure build-up inside the chamber. This can be observed in
the axial wall pressure distribution shown in Figure 4.18.
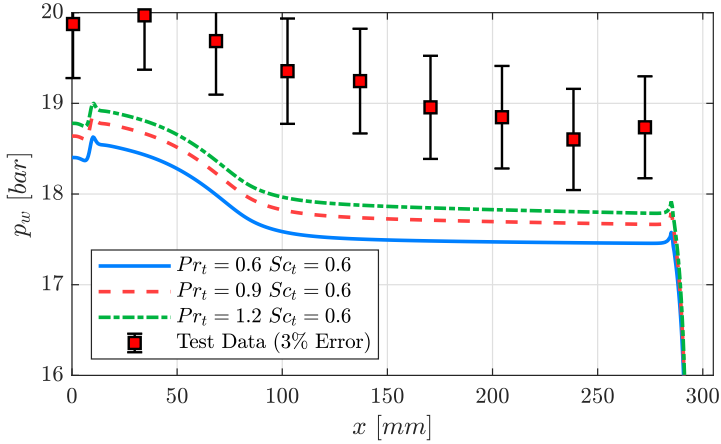
Figure 4.18: Influence of the turbulent Prandtl number on the pre-
dicted wall pressure - hydrogen test case ($O/F = 5.9$).

Since less energy is leaving the system, the average temperature in
the combustor rises. This has no significant impact on the flow field,
however. The flame length is unaffected by the turbulent Prandtl
number. This can be observed in the temperature plots in Fig-
ure 4.19. The flame length is represented in the plot by an isoline of
the mean mixture fraction at the stoichiometric value.

Now the turbulent Schmidt number is varied, while the turbulent
Prandtl number is kept constant at a value of 0.9. The turbulent
Schmidt number characterizes the ratio between the turbulent trans-
port of momentum and the turbulent transport of species. Its defini-
tion is given in equation 3.12 and repeated here for convenience:

$$Sc_t = \frac{\mu_t}{\bar{\rho}\bar{D}_k}.$$

The turbulent Schmidt number appears in the species conservation
equation 3.5 and mixture fraction conservation equation 3.6 as part of

Figure 4.19: Influence of the turbulent Prandtl number on the temperature field and the flame length - hydrogen test case ($O/F = 5.9$).

the turbulent fluxes defined by equation 3.11. From the definition of the turbulent Schmidt number, the turbulent species diffusivity can be calculated. In the same way, as the turbulent heat conductivity describes the turbulent heat transfer, the turbulent species diffusivity describes the transport of species due to the turbulent motion of the fluid. An increase in the turbulent Schmidt number leads to a decrease in the turbulent species diffusivity and a lower turbulent species transport.

Figure 4.20 shows the influence of the turbulent Schmidt number on the predicted wall heat flux. Increasing the turbulent Schmidt number moves the peak heat flux downstream. The peak as well as the integrated heat flux decrease. The peak is about 18 % lower when going from a value of $Sc_t = 0.6$ to 1.2. After the mixing process is completed towards the end of the chamber's cylindrical part, no significant impact of the turbulent Schmidt number can be observed.
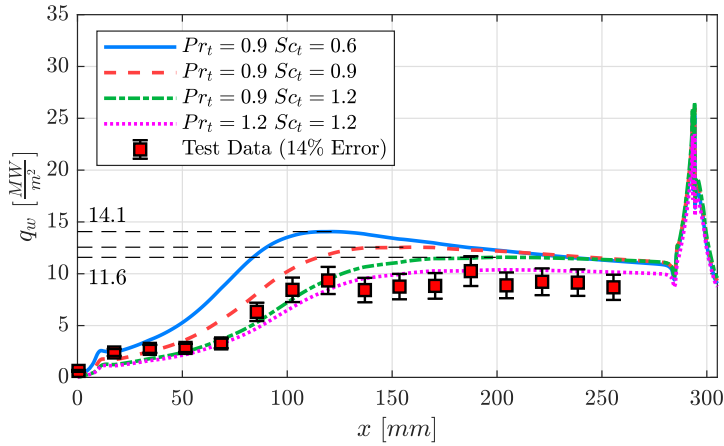
Figure 4.20: Influence of the turbulent Schmidt number on the predicted wall heat flux - hydrogen test case ($O/F = 5.9$).

Similar to the behavior for turbulent Prandtl number increase, the decrease of the turbulent Schmidt number leads to a higher loss of energy to the wall. This energy is now not contributing to the pressure build-up. This is shown in Figure 4.21. However, the Schmidt number also affects the curvature of the axial pressure distribution. Higher values lead to a more gradual decrease in pressure, as heat is released more slowly in the flame due to a lower transport rate of the propellants to the reaction zone.

In Figure 4.22 the unmixedness is plotted along the length of the combustion chamber. Here the enhanced mixing effect due to lowering the turbulent Schmidt number can be seen directly. A homogeneous propellant mixture ratio state is reached significantly earlier in the combustor. Note that when the unmixedness tends towards zero, the mixture ratio tends towards its injection value at each point of a cross section.
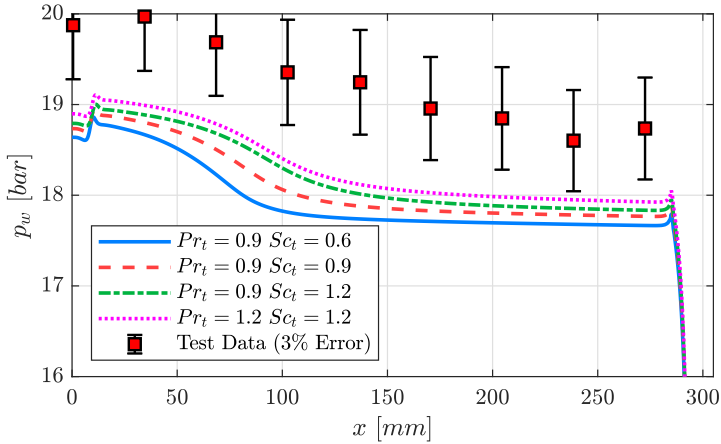
Figure 4.21: Influence of the turbulent Schmidt number on the predicted wall pressure - hydrogen test case ($O/F = 5.9$).

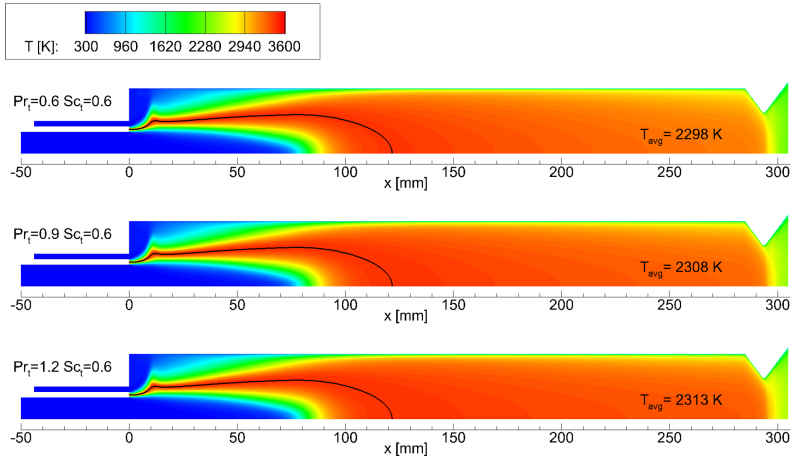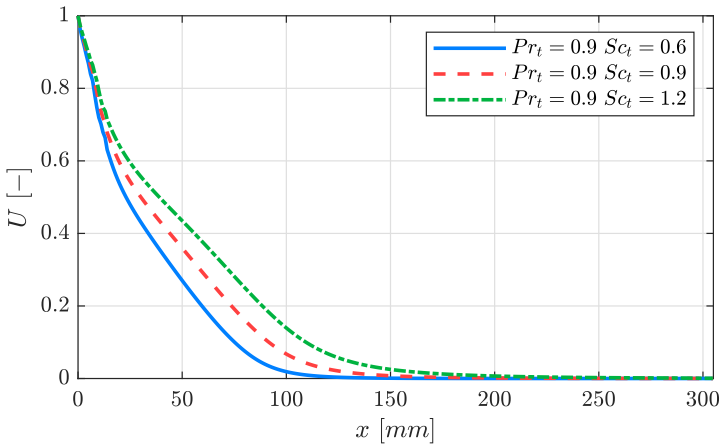**Figure 4.22:** Influence of the turbulent Schmidt number on the unmixedness - hydrogen test case ($O/F = 5.9$).
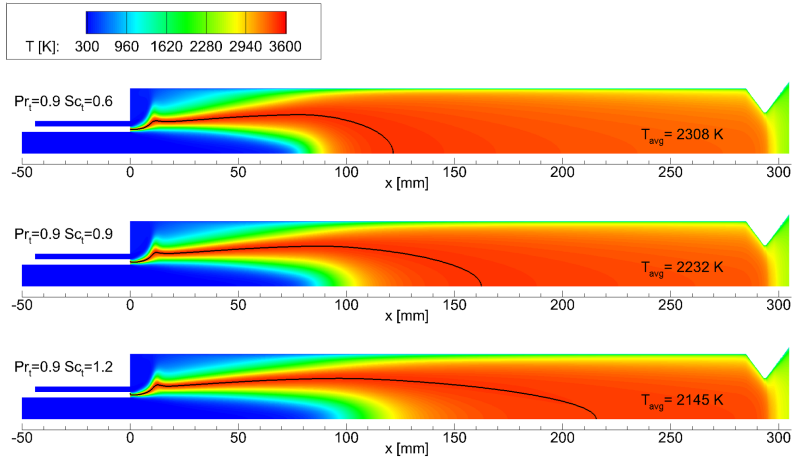
Figure 4.23: Influence of the turbulent Schmidt number on the temperature field and the flame length - hydrogen test case ($O/F = 5.9$).

This faster mixing process also impacts the flame length and the average temperature in the combustor. Figure 4.23 shows the temperature field inside the chamber. The average temperature is indicated in the plot. The higher the turbulent Schmidt number is, the lower is the average temperature. The flame length is again indicated by the stoichiometric line of the mixture fraction crossing the combustor axis. The flame is significantly longer for higher turbulent Schmidt numbers, and the cold oxidizer stream extends farther into the chamber.

Variations of the turbulent Prandtl number and the turbulent Schmidt number, here presented for the hydrogen test case, have the same principle impact on the methane cases. They are therefore not shown here in their entirety. Results for a subset of these variations are shown in the next section.

4.4.4 Turbulence Modeling Conclusion

Four different turbulence models were investigated as part of this thesis. A comparison shows models belonging to the k-ε-family are better suited than the models of the k-ω-family for the MoRaP round single-element test case. Both employed k-ω models underpredict the mixing process and heat release in the combustion zone. This leads to an underprediction of the pressure build-up in the combustor. Both the wall pressure distribution and the wall heat flux show a qualitative trend that differs from the experimental results.

When employing the so-called Yap-correction, both investigated k-ε models yield almost identical results. They show a good qualitative agreement with the experimental data. The quantitative agreement is influenced by varying the turbulent modeling parameters for heat and species fluxes from the default values. The two-layer version of the k-ε models is used for all simulations following the model comparison as it showed a superior convergence behavior.

The variation of the turbulent modeling parameters Pr_t and Sc_t show the expected results. A higher turbulent Prandtl number yields a lower wall heat flux throughout the chamber without having a significant impact on the flame length or mixing quality. As more energy is kept in the chamber, the pressure rises. A lower turbulent Schmidt number enhances the mixing process and produces a shorter flame. This influences the qualitative behavior of the predicted validation quantities. The peak heat flux increases and moves upstream, and the pressure drops consequently.

For the hydrogen combustion test case values of $Pr_t = 1.2$ and $Sc_t = 1.2$ yield a reasonable prediction of the validation data. The qualitative behavior is well captured. The heat flux test data is matched well throughout the chamber; see Figure 4.21. The wall pressure is slightly lower than the experimental data (roughly 5 %);
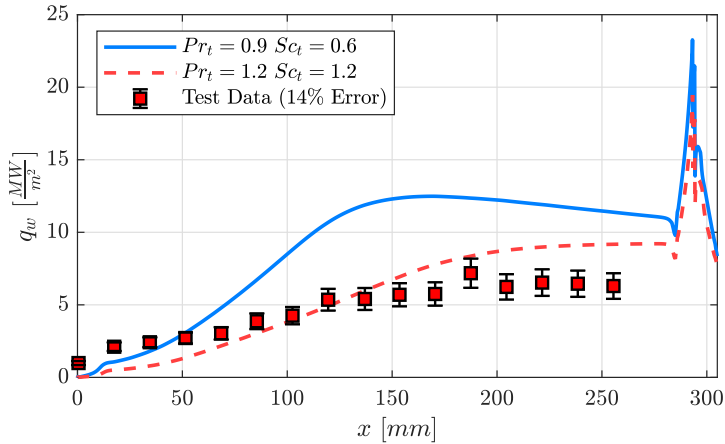
Figure 4.24: Predicted wall heat flux for different turbulent parameter settings - methane test case $(O/F = 2.2)$.

see Figure 4.21.

No parameter set was found for the methane combustion test case, which gives a satisfying prediction of the experimental data. There is still a significant overestimation of the wall heat flux in the cylindrical part of the combustor when using the same numbers that were set for the hydrogen case, see Figure 4.24. In addition, due to the high turbulent Schmidt number, the qualitative trend of the pressure distribution is changed and differs from the one observed in the test, see Figure 4.25. The base setup of $Pr_t = 0.9$ and $Sc_t = 0.6$ yields a much too high wall heat flux. The reason for this overprediction is the assumption of equilibrium chemistry in the cooled boundary layer of the combustion chamber. Combustion models that can mitigate this effect are investigated in the following section.
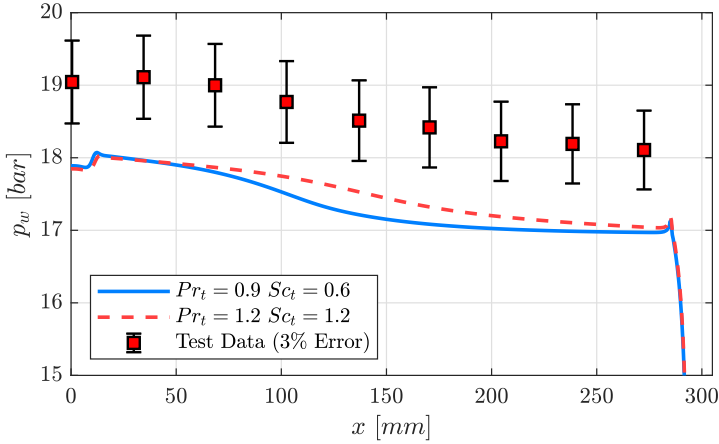
Figure 4.25: Predicted wall pressure for different turbulent parameter settings - methane test case ($O/F = 2.2$).

4.4.5 Combustion Modeling Study

An appropriate combustion model is necessary to accurately predict the performance and heat transfer characteristics of a given rocket combustor setup. The combustion model must simulate the turbulent reactions and the heat release in the flame zone as well as the post-flame recombination reactions in the strongly cooled boundary layer.

Three different combustion models were assessed as part of this thesis. Two of the three include user-developed model extensions to improve their performance. One was developed specifically for the application to the rocket combustor under investigation in this thesis. The following section presents and compares the simulation results obtained with these models to find the most suitable one for the MoRaP round single-element test case. Section 3.3 presents the theoretical background to these models.

Figure 4.26 shows the predicted temperature and mixture fraction

fields obtained with the three different combustion models. The temperature fields have superimposed the isoline of the stoichiometric oxidizer to fuel ratio ($O/F_{st,CH_4} = 4$). The mixture fraction fields have superimposed the streamlines of the velocity fields. Starting from the reference simulation with the equilibrium chemistry model (ECM; Figure 4.26 top) the combustion model was changed, once to finite rate chemistry (FRC; Figure 4.26 middle) and once to the perfectly stirred reactor model (PSRM; Figure 4.26 bottom). All simulations were performed with a turbulent number of $Pr_t = 0.9$ and a turbulent Schmidt number of $Sc_t = 0.6$ and the two-layer k-ε model.

The flow field, indicated by the streamlines and the mixture fraction distribution, is qualitatively similar for all three simulations. The corner vortex in the injector near region is of approximately the same extent. The temperature field and the flame length, indicated by the stoichiometric isoline, are also similar. The flame front shows a comparable width in all simulations and reaches about 180 mm into the combustion chamber, where the stoichiometric isoline crosses the combustor axis.

It should be noted that the isoline of the stoichiometric oxidizer to fuel ratio can be directly extracted from the mixture fraction field through the following relation:

$$\frac{O}{F} = \frac{1}{1 + Z}. \tag{4.4}$$

The mixture fraction is transported in quantity and directly available from the solver for the two tabulated chemistry models. For the finite rate chemistry simulations, the mixture fraction field is determined in a post-processing step based on the elemental mass fraction of the hydrogen atom and normalized by its values at the inlets. It is then

calculated as:

$$Z = \frac{Z_H - Z_{H,Ox}}{Z_{H,Fu} - Z_{H,Ox}}, \qquad (4.5)$$

where Z_H is the local elemental mass fraction of atomic hydrogen and $Z_{H,Fu}$ and $Z_{H,Ox}$ are the respective values at the fuel and oxidizer inlets.

A more quantitative evaluation is achieved by comparing the influence of the combustion models on the radial profiles of the temperature as well as mass fractions of H_2O, CO_2 and CO at three different positions along the combustor axis. Markers indicate the values in the wall nearest cell for better visualization. The first position lies 50 mm from the faceplate into the combustor. Here the oxygen core injected through the single-element centered on the combustor axis is still clearly visible. At the second position, 150 mm into the combustion chamber, the oxygen core has already reacted with the surrounding gaseous methane fuel. The stoichiometric isoline has not yet crossed the combustor axis, however. The third location is located 250 mm into the chamber, just before the nozzle section. It lies shortly behind the flame front. The three positions are marked in Figure 4.26 by dashed white lines for orientation.

Figure 4.27 shows the radial profiles at the first axial evaluation position. All combustion models show a similar qualitative and quantitative behavior of the temperature profile (Figure 4.27a) from the core flow towards the combustor wall. The maximum predicted temperatures are comparable, and the temperature difference in the cell closest to the wall, which is used for the heat flux calculation, is < 7 K. The FRC model displays a slightly more gradual decrease in temperature from the peak in the flame front to the onset of the boundary layer. All models show a steep decrease in temperature very close to the cool wall.

The H_2O mass fraction profiles (Figure 4.27b) follow a similar trend
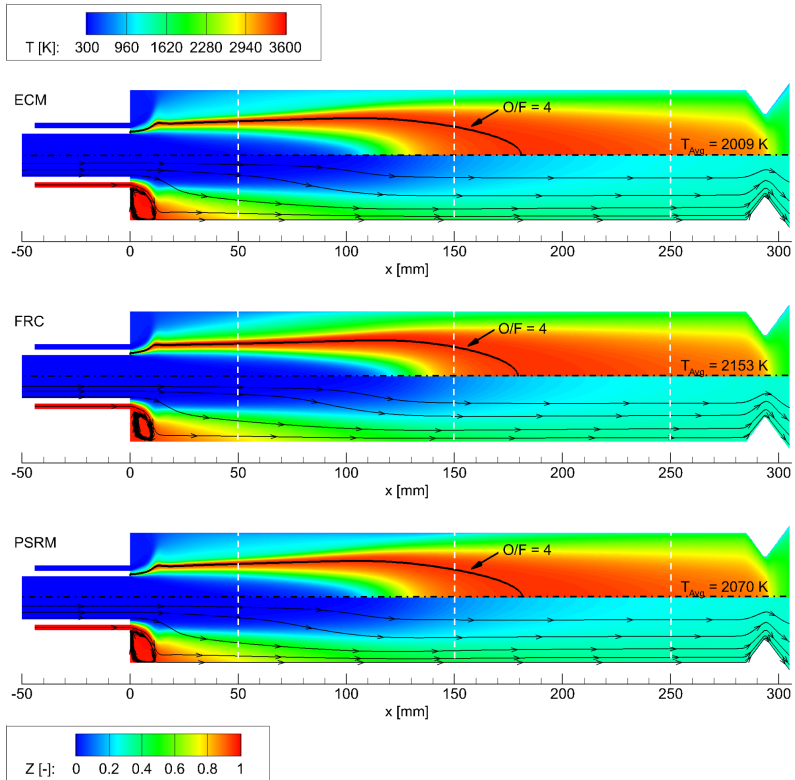
Figure 4.26: Influence of the combustion model on the predicted temperature (upper half; including stoichiometric isoline) and mixture fraction fields (lower half; including streamlines) - methane test case ($O/F = 2.2$).
(Plot is in non-scale division $x/y = 0.2$)

(a) Temperature

(b) H_2O Mass Fraction

(c) CO_2 Mass Fraction

(d) CO Mass Fraction

Figure 4.27: Influence of the combustion model on the radial profiles of the temperature and mass fractions of H_2O, CO_2 and CO at an axial position of $x = 50$ mm - methane test case ($O/F = 2.2$). (Nearest wall cell values are indicated by markers: Circle for the ECM, square for the FRC, cross for the PSRM)

(a) Temperature

(b) H_2O Mass Fraction

(c) CO_2 Mass Fraction
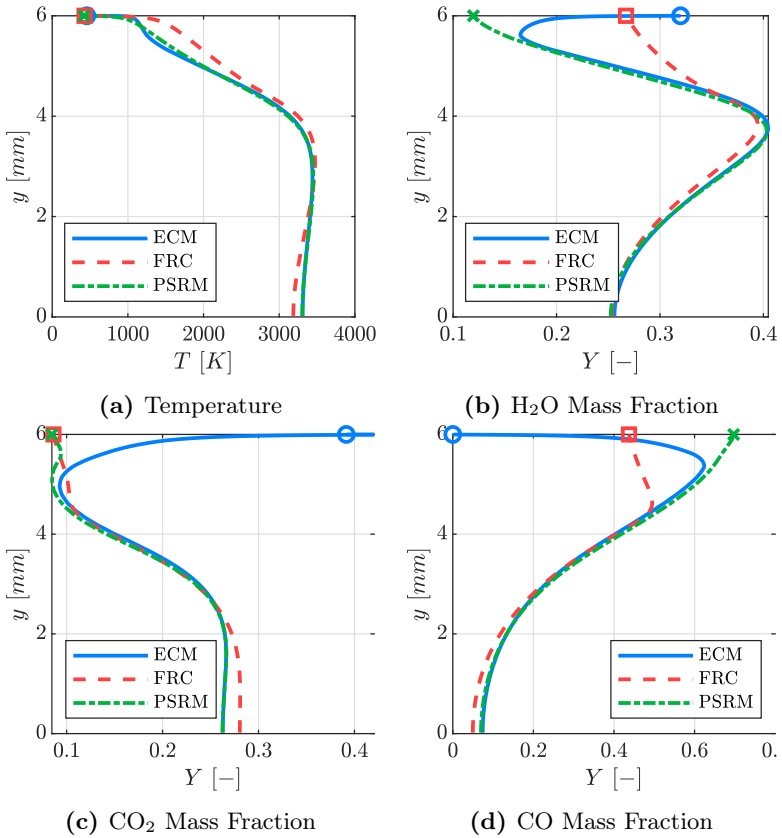
(d) CO Mass Fraction

Figure 4.28: Influence of the combustion model on the radial profiles of the temperature and mass fractions of H_2O, CO_2 and CO at an axial position of $x = 150$ mm - methane test case ($O/F = 2.2$). (Nearest wall cell values are indicated by markers: Circle for the ECM, square for the FRC, cross for the PSRM)

(a) Temperature

(b) H_2O Mass Fraction

(c) CO_2 Mass Fraction

(d) CO Mass Fraction

Figure 4.29: Influence of the combustion model on the radial profiles of the temperature and mass fractions of H_2O, CO_2 and CO at an axial position of $x = 250$ mm - methane test case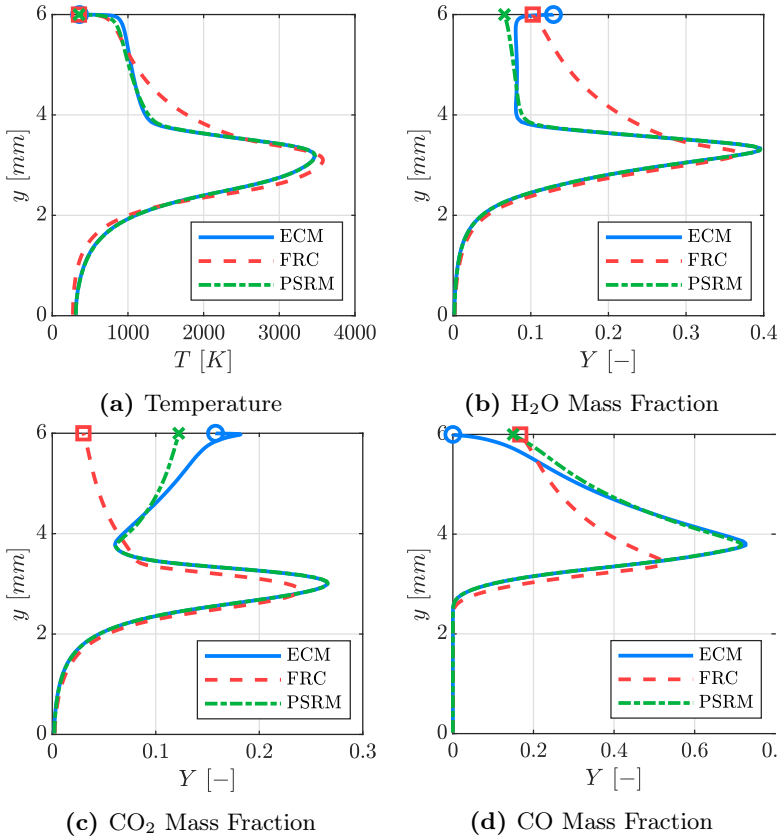 ($O/F = 2.2$). (Nearest wall cell values are indicated by markers: Circle for the ECM, square for the FRC, cross for the PSRM)
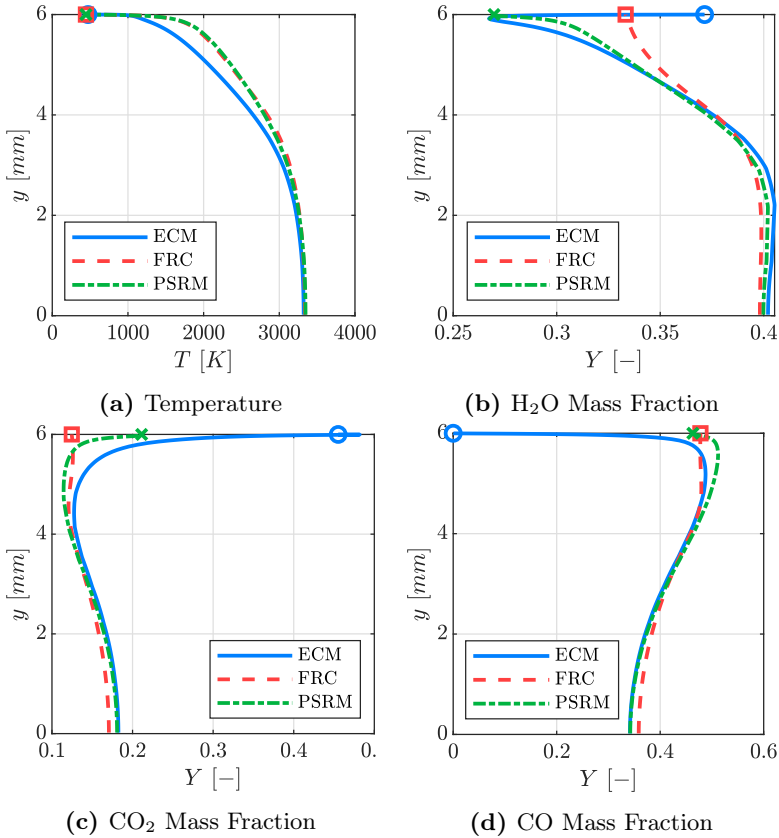
for all combustion models from the combustor axis up until the flame front. Both tabulated chemistry models exhibit a rapid decrease from 0.4 to approximately 0.08, close to the reaction zone. Afterward, in the radial direction, the H_2O mass fraction stays almost constant for the PSRM model. The ECM model, in contrast to both the other models, predicts a recombination reaction that produces H_2O in the boundary layer and thereby increases the mass fraction by roughly 4%. The FRC model predicts a gradual decrease in H_2O concentration from the flame front to the wall, including the near-wall region.

The CO_2 mass fraction profiles (Figure 4.27c) also follow a similar trend towards the flame front as well as close to the reaction zone. While the FRC model predicts a strict decrease of CO_2 in radial direction after its peaks value, both tabulated chemistry models show recombination outside the flame. This recombination leads to a substantial decrease in the concentration of CO, where the ECM model predicts no presence of CO in the near-wall region of the combustor. The PSRM also predicts a substantial decrease in CO. However, because of the lower peak value predicted when using FRC, both PSRM and FRC predict a CO value of approximately 18% at the wall.

The radial profiles at the second and third axial evaluation position are shown in Figure 4.28 and Figure 4.28 respectively. The qualitative and quantitative behavior at both locations is very similar (with some exceptions in the CO and CO_2 mass fractions), but it differs depending on the combustion model employed.

The temperature profile (Figure 4.28a and Figure 4.29a) still looks similar between the different modeling approaches. However, the temperature difference between the FRC model and the PSRM model compared to the ECM model is up to 37 K in the wall region.

The recombination of H_2O is now strongly noticeable in the mass fraction profiles (Figure 4.28b and Figure 4.29b) for the ECM model.

An increase of up to 18% is predicted. Neither the FRC model nor the PSRM model predicts recombination of H_2O. The PSRM predicts the lowest amount of H_2O in the wall nearest cell, followed by the FRC model.

The most significant difference between the combustion models is noticeable between the mass fraction profiles of CO_2 and CO. The differences are mainly restricted to a zone of up to 1 mm distance from the combustor wall. The CO_2 and CO profiles predicted by the ECM model show an opposing trend. The mass fraction of CO is reduced from 60% to zero, and the carbon atoms are present as CO_2 mainly, causing the CO_2 concentration to increase significantly. This behavior is not predicted by the FRC and the PSRM model at the 150 mm axial location. It is also not predicted by the FRC at the 250 mm location. However, it is present here using the PSRM model, but extent of the recombination is much less than in the ECM model. Both the FRC and the PRSM model predict residual amounts of CO in the near-wall region.

The differing predictions by the investigated combustion models in the radial temperature profiles and combustion gas composition directly impact the integral quantities used here for model validation and used in general as design parameters for liquid rocket engines. The results produced by the three combustion models for the wall heat flux distribution are shown in Figure 4.30 together with the experimental data reconstructed from thermocouple readings of the hot firing test.

In the early parts of the combustion chamber, within 50 mm from the injector face, all combustion models underestimate the experimental heat flux. In the experiment, the heat flux rises gradually after x=50 mm until a plateau is reached around 200 mm into the chamber. Both the FRC model and the PSRM model give a good prediction of this behavior. The simulation results agree with the

experimental data within the experimental error for most of the evaluation points. The values at the plateau are slightly overestimated by the PSRM model, while they are still within the measurement error for the FRC model.

The most significant difference is in the predictions of the heat flux rise and plateau value between the FRC and the PSRM model compared to the ECM model. The use of the ECM model results in a significant overestimation of the reconstructed experimental heat flux values. This is a direct consequence of the assumption o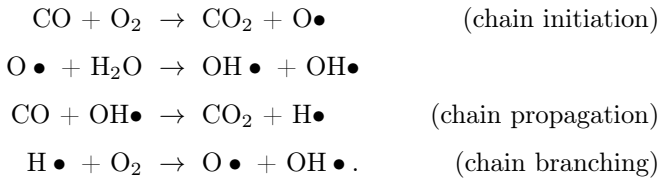f chemical equilibrium in the cooled boundary layer. As is visible in the radial profiles of the temperature and mass fractions, there are significant recombination reactions predicted in equilibrium. These result in the formation of H_2O and CO_2 as well as the destruction of CO. The reactions are associated with a heat release near the combustor wall, directly increasing the near-wall temperature and the wall heat flux.

Looking at the oxidation of CO, as discussed by *Wang* [101], the chemical reaction steps involved in the conversion of CO to CO_2 may be written as

$$CO + O_2 \ \rightarrow \ CO_2 + O\bullet \qquad \text{(chain initiation)}$$
$$CO + O\bullet + M \ \rightarrow \ CO_2 + M \qquad \text{(chain termination)}$$
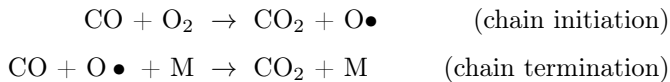
for the dry oxidation of CO. If H_2O is present the following sequence of reaction steps applies

$$CO + O_2 \ \rightarrow \ CO_2 + O\bullet \qquad \text{(chain initiation)}$$
$$O\bullet + H_2O \ \rightarrow \ OH\bullet + OH\bullet$$
$$CO + OH\bullet \ \rightarrow \ CO_2 + H\bullet \qquad \text{(chain propagation)}$$
$$H\bullet + O_2 \ \rightarrow \ O\bullet + OH\bullet. \qquad \text{(chain branching)}$$
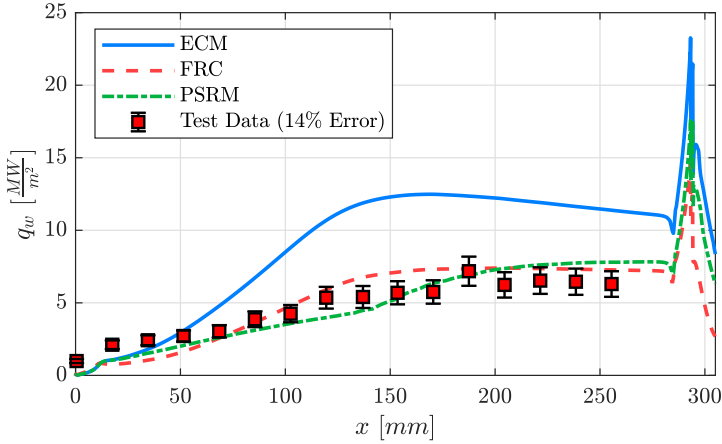
Figure 4.30: Influence of the combustion model on the predicted wall heat flux - methane test case ($O/F = 2.2$).

If H_2 is present in the combustion gas the reactions

$$O \bullet \ + H_2 \ \rightarrow \ OH \bullet \ + H\bullet \qquad \text{(chain branching)}$$

$$OH \bullet \ + H_2 \ \rightarrow \ H_2O + H\bullet \qquad \text{(chain propagation)}$$
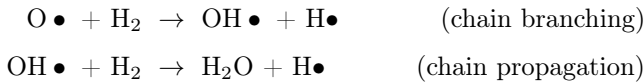
will further facilitate the conversion process.

These reaction steps show that free radicals (e.g. $O\bullet$, $H\bullet$, $OH\bullet$) for chain branching and propagation are critical for continuing oxidation of carbon monoxide and the overall conversion rate. This is true for dry as well as hydrogen-assisted oxidation.

The recombination process occurs in the flow field towards the wall because of the combustion gas cooldown from the cold boundary. As is shown in Figure 4.31 the free radicals vanish entirely before the onset of the wall-flow boundary layer. The strong recombination reactions displayed by the ECM model are therefore unlikely to occur and are not predicted by the two other models, which incorporate

chemical kinetics.

Figure 4.32 shows the predicted wall pressure distribution in the axial direction for all three investigated combustion models in comparison with the experimental data gained from the pressure transducers during the hot firing test. All simulations display an excellent qualitative agreement with the test data. A slight pressure drop is observable in the upstream part of the combustor near the faceplate. This pressure drop is due to the presence of the recirculation zone in this region (see Figure 4.26). The stagnation point, indicated by the maximum wall pressure value, occurs between the first and the second measurement location in the chamber. Afterward, the fluid flow accelerates due to the expansion caused by the heat release in the combustion process.

Consequently, the pressure drops and gradually flattens out towards the downstream region of the cylindrical part of the combustor. The pressure drop shows a distinct concave shape. The almost flat pressure profile is an indication that the end of combustion has occurred. A further decrease in pressure is only due to wall heat losses.

The overall pressure drop from the second to the last measurement location is between 1 to 1.2 bar. This equals 5.5 to 6.2 % of the peak pressure, while the experimental data shows a drop of 1 bar, equalling 5.3 % of the peak pressure. However, the overall pressure level predicted by the ECM model is significantly lower than the values observed in the hot firing test. In contrast, the values predicted by the FRC model and the PSRM model are in good quantitative agreement. There are two main reasons for the underestimation by the ECM model. First, the significant overestimation of the wall heat flux, shown in Figure 4.30, leads to an energy loss in the system. The lost energy does not contribute to the pressure rise any longer. The second reason, partially linked to the first one, is the lower average

(a) O Mass Fraction

(b) H Mass Fraction
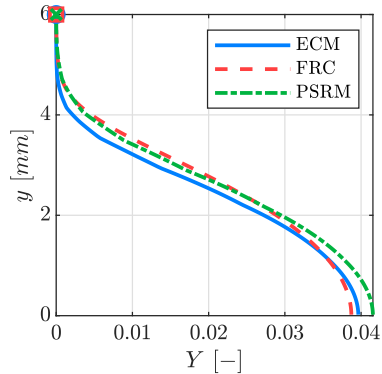
(c) OH Mass Fraction

Figure 4.31: Influence of the combustion model on the radial profiles of the free radical mass fractions of O, H and OH at an axial position of $x = 250$ mm. (Nearest wall cell values are indicated by markers: Circle for the ECM, square for the FRC, cross for the PSRM)
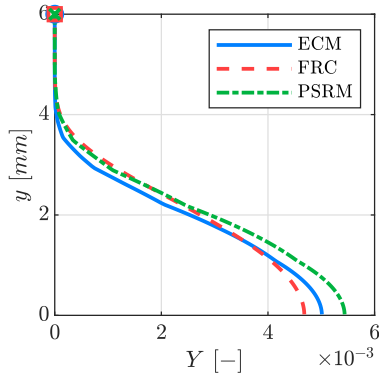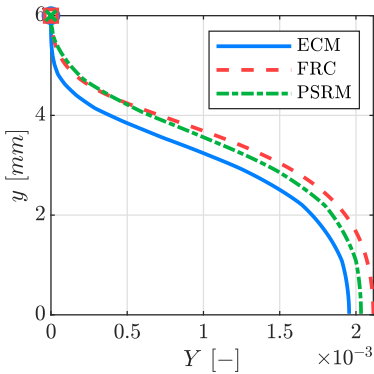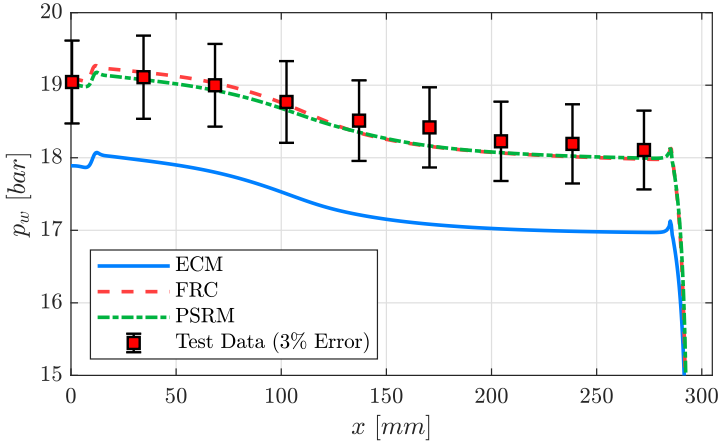
Figure 4.32: Influence of the combustion model on the predicted wall pressure - methane test case ($O/F = 2.2$).

bulk temperature of the hot gas in the ECM model simulation shown in Figure 4.26. It is 2009 K, 2153 K, and 2070 K for the ECM, the FRC, and the PSRM model. Figure 4.33 shows the mean temperature in the axial direction and averaged over the cross-section. The models agree in their prediction to about 120 mm into the combustion chamber. Afterward, the profiles predicted by the FRC and the PSRM model rise to a similar plateau but in a differing slope. However, the use of the ECM model results in a lower plateau value, which directly impacts the overall pressure level.

Table 4.6 lists the predicted combustion efficiencies for all three combustion models as well as the efficiency from the hot firing test. The difference between the experimental value and the FRC and PSRM model values is less than 1 % when comparing the results for the adiabatic combustion efficiencies η_{c^*}. The result from the ECM model simulation deviates by more than 5 %. Note that it can
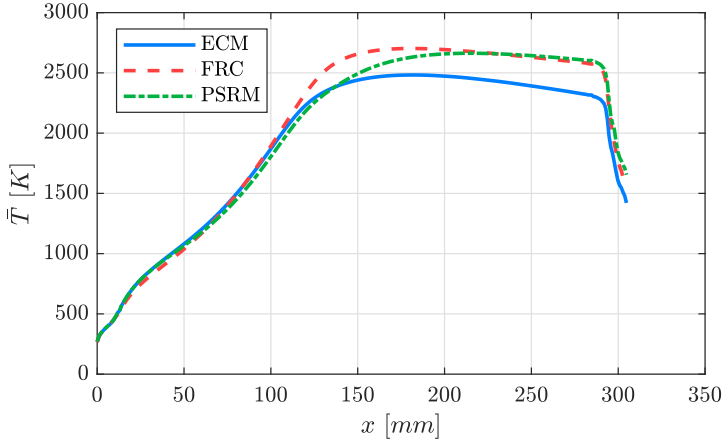
Figure 4.33: Influence of the combustion model on the mean temperature in axial direction and averaged over the cross-section - methane test case ($O/F = 2.2$).

not be determined from the adiabatic combustion efficiency whether the cause of the underprediction is incomplete mixing or increased wall heat loss. Therefore it is unclear if the performance of the combustor can be increased by a redesign of the injector, which is the main driver for the mixing quality. When comparing the results for the enthalpy corrected combustion efficiencies $\eta_{c^*,h}$, the difference between the experimental values and the predicted values is smaller than 1 % for all combustion models. Therefore the lower value using the ECM model in the adiabatic case results from the higher wall heat flux. From the enthalpy corrected combustion efficiencies, the simulations predict the mixing efficiency of the injector quite well, independent of the combustion model. This study shows that the adiabatic combustion efficiency is not well suited for analyzing test cases with substantial heat loss through the combustor wall. When using the enthalpy correction introduced in section 4.3, the combus-

tion efficiency can be reduced to a quantity that is mainly related to the mixing quality produced by the injector. This makes it possible to conclude on the necessity of injector design improvements.

Table 4.6: Predicted and experimental combustion efficiencies.

	η_{c^*} [%]	$\eta_{c^*,h}$ [%]
TRC-1-2-22-30-10	92.8	98.7
ECM	87.0	98.2
FRC	92.1	98.5
PSRM	92.2	98.0

4.4.6 Combustion Modeling Conclusion

Three different combustion models were investigated as part of this thesis. The results show that while the model based on chemical equilibrium yields good results for hydrogen/oxygen combustion in conjunction with the previously described turbulence modeling settings, it significantly overpredicts the wall heat flux in the methane/oxygen test case. This, in turn, leads to a pressure level below the one observed in the experiment. This overprediction is due to strong recombination reactions in close vicinity to the combustor walls, which do not occur when including chemical kinetics using a finite rate chemistry model. The finite rate chemistry model is highly computationally expensive and does not lend itself to quick turnaround design and optimization work. Therefore, the insight gained from the high fidelity model was used to develop a tabulated chemistry model that includes chemical kinetic effects. The model is based on a perfectly stirred reactor. The model can improve the predictions for methane/oxygen combustion and gives results with reasonable ac-

curacy compared to the validation data. For hydrogen/oxygen, the model yields within a good accuracy the same results as the chemical equilibrium model (not shown here).

5 Conclusion

The present thesis deals with the numerical modeling and analysis of the fluid flow and combustion in liquid rocket engines to predict performance and heat transfer characteristics. Advanced numerical design tools have an increasing share in the development process over experimental work. They provide additional resources to gain insight into the complex physical phenomena prevailing in a rocket thrust chamber and help exploit and minimize design margins. Nevertheless, all tools need to be validated against experimental test campaigns to increase the confidence in their numerical predictions.

In the present work, the experimental data from a lab-scale single shear-coax element rocket combustor is evaluated and used as a validation benchmark for developing a numerical model. Pressure and heat flux measurements are available from hot firing tests using hydrogen/oxygen and methane/oxygen as a propellant combination. The numerical model is based on Computational Fluid Dynamics (CFD) as this promises an improved transferability to new design concepts in comparison to the legacy methods based on empirical Nusselt-type correlations.

The literature review shows that the main drivers for an accurate prediction of performance and heat transfer characteristics are turbulence and combustion modeling and the determination of thermodynamic and transport properties. All these aspects are addressed. Two critical requirements in the development of the presented model were the time frame to deliver results and the robustness of the ap-

proach. For this reason, a RANS approach was used for turbulence modeling over much more computational expensive LES methods. Different turbulence models were assessed to find the most suitable one for the combustor configuration at hand. The investigations show that models of the k-ε family give better predictions of the mixing progress driven by the shear-coax injection element than models of the k-ω family, which show high unmixedness that leads to a qualitatively different wall pressure distribution from the experimental data. In addition, the sensitivity of the numerical results to the turbulent modeling parameters Pr_t and Sc_t was analyzed. As expected from the literature review, these parameters significantly influence wall pressure and wall heat flux. For the hydrogen/oxygen test case, finding a parameter setting that gives good agreement with the experimental data using an equilibrium chemistry model using reasonable turbulence parameter values was possible. In contrast, this was not accomplished for the methane/oxygen test case due to a significant overprediction of the wall heat flux.

The cause of this overprediction lies in the fact that the validity of the chemical equilibrium assumption no longer holds in the strongly cooled boundary layer for methane/oxygen combustion due to the comparatively large chemical time scales of the recombination reactions. This phenomenon was investigated using a finite rate chemistry model, including chemical kinetics. The results show that assuming equilibrium chemistry produces high concentrations of H_2O and CO_2 in close vicinity to the combustor wall. Here H_2 & OH are recombined to H & H_2O and CO & OH to CO_2 & H_2O. This recombination is associated with a heat release. The reactions do not appear when employing a chemical kinetic scheme. In that case, the hot gas composition practically freezes as soon as the radical concentration drops below a certain threshold. A tabulated method was developed to capture the same principle physical effect by using the detailed fi-

nite rate chemistry knowledge without the additional computational expense and fragility of the fully resolved simulation. The method is based on a perfectly stirred reactor model and takes advantage of the fact that the large time scale reactions are the main driver in the recombination process. The model was validated using the available test data. The simulations show a big improvement compared to the equilibrium chemistry model while keeping the same efficiency of the tabulated approach as no additional dimensions are added to the chemistry table. The predictions are now in line with the experimental data and can be produced on a typical workstation within hours rather than days (for the full finite rate chemistry model).

Additional validation cases need to be investigated going forward to increase the confidence in the predictive capabilities of the developed numerical model. This could mean the simulation of additional operating points and different rocket combustor configurations. As an outlook for this work, potential model extensions include the use of additional transport equations for the determination of the turbulent heat conductivity and mass diffusivity or even a switch to LES for turbulence modeling. This would negate the need to use a fixed number for the turbulent modeling parameters Pr_t and Sc_t. Additionally, the combustion model can be extended by an additional time-scale dimension, which takes into account mid-term recombination effects in addition to the long-term effects. These model extensions could further increase the accuracy of the predictions and capture additional physical effects potentially prevalent in different applications. This would further increase the transferability of the model to new combustor designs. However, these extensions are associated with an increased computational expense for each simulation. Their necessity needs to be assessed in each case if the time frame to achieve results is limited by the development schedule.

Bibliography

[1] G. Schmidt. *Technik der Flüssigkeits-Raketenantriebe*. DaimlerChrysler Aerospace, Munich, Germany, 1999.

[2] J. Lin, J.S. West, R.W. Williams, P.K. Tucker, and J.D. Chenoweth. CFD Code Validation of Wall Heat Fluxes for a GO_2/GH_2 Single Element Combustor. In *Proceedings of the 41st AIAA/ASME/SAE/ASEE Joint Propulsion Conference & Exhibit*, Tucson, AZ, United States of America, 2005.

[3] O. Knab, A. Fröhlich, J. Görgen, and D. Wiedmann. Advanced Thrust Chamber Layout Tools. In *Proceedings of the 4th International Conference on Launcher Technology*, Liege, Belgium, 2002.

[4] E. Sozer. *Modeling of Gaseous Reacting Flow and Thermal Environment of Liquid Rocket Injectors*. Dissertation - University of Michigan, 2010.

[5] C. Kirchberger. *Filmkülung in Thermtest (Softwaredokumentation)*. Institute of Flight Propulsion, Technical University of Munich, Munich, Germany, 2005.

[6] D.R. Bartz. Survey of the relationship between theory and experiment for convective heat transfer from rocket combustion gases. In *Proceedings of the Agard Colloquium*, LA JOLLA, California, United States of America, 1968.

[7] G.B. Sinjarev and M.V. Dobrovolsky. *Liquid Rocket Engines - Theory and Design [in Russian].* Oborongiz Publishing, Moscow, USSR, 1955.

[8] H. Kraussold. Die Wärmeübertragung an Flüssigkeiten in Rohren bei turbulenter Strömung. *Forschung auf dem Gebiet des Ingenieurwesens A*, 4(1):39–44, 1933.

[9] C. Kirchberger. *Investigation on Heat Transfer in Small Hydrocarbon Rocket Combustion Chambers.* Dissertation - Technical University of Munich, 2014.

[10] O.J. Haidn, N. Adams, R. Radespiel, W. Schröder, C. Stemmer, T. Sattelmayer, and B. Weigand. Fundamental Technologies for the Development of Future Space Transportsystem Components under high Thermal and Mechanical Loads. In *Proceedings of the 54th AIAA/SAE/ASEE Joint Propulsion Conference*, Cincinnati, OH, United States of America, 2018.

[11] N. Adams, W. Schröder, R. Radespiel, O.J. Haidn, T. Sattelmayer, C. Stemmer, and B. Weigand. *Future Space-Transport-System Components under High Thermal and Mechanical Loads.* Springer-Verlag, Berlin/Heidelberg, Germany, 2021.

[12] S. Pal, W. Marshall, R. Woodward, and R. Santoro. Test case RCM 1: Penn state preburner combustion wall heat flux data for a GO_2/GH_2 uni-element combustor. In *Proceedings of the 3rd International Workshop Rocket Combustion Modeling*, Paris, France, 2006.

[13] P.K. Tucker, S. Menon, C.L. Merkle, and J.C. Oefelein. Validation of High-Fidelity CFD Simulations for Rocket Injector

Design. In *Proceedings of the 44th AIAA/ASME/SAE/ASEE Joint Propulsion Conference*, 2008.

[14] H. Riedmann, B. Kniesner, M. Frey, and C.D. Munz. Modeling of combustion and flow in a single element GO_2/GH_2 combustor. *CEAS Space Journal*, 6(1):47–59, 2014.

[15] Y. Daimon, H. Negishi, and N. Yamanishi. Combustion and Heat Transfer Modeling in Regeneratively Cooled Thrust Chambers (Wall Heat Flux Validation). In *Proceedings of the 46th AIAA/ASME/SAE/ASEE Joint Propulsion Conference & Exhibit*, 2010.

[16] E. Sozer, A. Vaidyanathan, C. Segal, and W. Shyy. Computational assessment of gaseous reacting flows in single element injector. In *Proceedings of the 47th AIAA Aerospace Sciences Meeting Including The New Horizons Forum and Aerospace Exposition*, 2009.

[17] E. Sozer, E.A. Hassan, S. Yun, S. Thakur, J. Wright, M. Ihme, and W. Shyy. Turbulence-chemistry interaction ans heat transfer modeling of H_2/O_2 gaseous injector flows. In *Proceedings of the 48th AIAA Aerospace Sciences Meeting Including The New Horizons Forum and Aerospace Exposition*, 2010.

[18] D. Preclik, G. Hagemann, O. Knab, L. Brummer, C. Mading, D. Wiedmann, and P. Vuillermoz. LOX/Hydrocarbon Propellant Trade Considerations for Future Reusable Liquid Booster Engines. In *Proceedings of the 41st AIAA/ASME/SAE/ASEE Joint Propulsion Conference & Exhibit*, Tucson, AZ, United States of America, 2005.

[19] D. Haeseler, A. Götz, and A. Fröhlich. Non-toxic Propellants for Future Advanced Launcher Propulsion Systems. In *Pro-

ceedings of the 36th AIAA/ASME/SAE/ASEE Joint Propulsion Conference & Exhibit, Las Vegas, NV, United States of America, 2000.

[20] O. Haidn, M. Oschwald, W. Clauss, R. Arnold, J. Sender, A. Preuss, D. Preclik, C. Mading, J. Görgen, and S. Soller. LOX/Methane Technology Efforts for Future Liquid Rocket Engines. In *Proceedings of 5th International Spacecraft Propulsion Conference & 2nd International Symposium on Propulsion for Space Transportation*, Crete, Greece, 2008.

[21] T. Markusic. *Lecture Notes - SpaceX Propulsion*. Lecture Series - Proceedings of the 46th AIAA/ASME/SAE/ASEE Joint Propulsion Conference & Exhibit, 2010.

[22] R.L. Morehead. Project Morpheus Main Engine Development and Preliminary Flight Testing. In *Proceedings of the 47th AIAA/ASME/SAE/ASEE Joint Propulsion Conference & Exhibit*, San Diego, CA, United States of America, 2011.

[23] O.J. Haidn, M. Celano, S. Silvestri, C. Kirchberger, and G. Schlieben. *Transregio SFB/TRR 40 Test Case 1*. Institute of Flight Propulsion, Technical University of Munich, Munich, Germany, 2015.

[24] A. Chemnitz, T. Sattelmayer, C. Roth, O.J. Haidn, Y. Daimon, R. Keller, P.M. Gerlinger, J. Zips, and M. Pfitzner. Numerical Investigation of Flow and Combustion in a Single-Element GCH_4/GOX Rocket Combustor: Aspects of Turbulence Modeling. In *Proceedings of the 52n AIAA/ASME/SAE/ASEE Joint Propulsion Conference & Exhibit*, Salt Lake City, UT, United States of America, 2016.

[25] D. Maestro, B. Cuenot, A. Chemnitz, T. Sattelmayer, C. Roth, O.J. Haidn, Y. Daimon, R. Keller, P.M. Gerlinger, G. Frank, M. Pfitzner, and L. Selle. Numerical Investigation of Flow and Combustion in a Single-Element GCH$_4$/GOX Rocket Combustor: Chemistry Modeling and Turbulence-Chemistry Interaction. In *Proceedings of the 52n AIAA/ASME/SAE/ASEE Joint Propulsion Conference & Exhibit*, Salt Lake City, UT, United States of America, 2016.

[26] C. Roth, O.J. Haidn, A. Chemnitz, T. Sattelmayer, G. Frank, H. Müller, J. Zips, R. Keller, P.M. Gerlinger, D. Maestro, B. Cuenot, H. Riedmann, and L. Selle. Numerical Investigation of Flow and Combustion in a Single-Element GCH$_4$/GOX Rocket Combustor. In *Proceedings of the 52n AIAA/ASME/SAE/ASEE Joint Propulsion Conference & Exhibit*, Salt Lake City, UT, United States of America, 2016.

[27] S. Silvestri, M.P. Celano, G. Schlieben, and O.J. Haidn. Characterization of a Multi-Injector GOX/CH4 Combustion Chamber. In *Proceedings of the 52nd AIAA/ASME/SAE/ASEE Joint Propulsion Conference & Exhibit*, Salt Lake City, UT, United States of America, 2016.

[28] N. Perakis, A. Sternin, C. Roth, and O.J. Haidn. Heat transfer and combustion simulation of a 7-element GOX/GCH$_4$ rocket combustor. In *Proceedings of the Summer Program 2017 of the SFB TRR 40*, Munich, Germany, 2017.

[29] D. Eiringhaus, D. Rahn, H. Riedmann, and O. Knab. Numerical Investigation of a 7-element GOX/GCH4 combustion chamber. In *Proceedings of the Summer Program 2017 of the SFB TRR 40*, Munich, Germany, 2017.

[30] Y. Daimon, H. Terashima, D. Muto, H. Tani, N. Negishi, and O. Knab. Comparison Study between GCH4/GO2 Single- and Multi-element Combustion Chamber. In *Proceedings of the Summer Program 2017 of the SFB TRR 40*, Munich, Germany, 2017.

[31] D. Suslov, B. Betti, T. Aichner, S. Soller, F. Nasuti, and O.J. Haidn. Experimental Investigation and CFD-Simulation of the Film Cooling in an O_2/CH_4 subscale Combustion Chamber. In *Proceedings of the Space Propulsion 2012*, Bordeaux, France, 2012.

[32] B. Betti, D. Bianchi, F. Nasuti, and E. Martelli. Chemical Reaction Effects on Wall Heat Flux in Liquid Rocket Thrust Chambers. In *Proceedings of the 50th AIAA/ASME/SAE/ASEE Joint Propulsion Conference & Exhibit*, Cleveland, OH, United States of America, 2014.

[33] O. Knab, M. Frey, J. Göorgen, K. Quering, D. Wiedmann, and C. Mäding. Progress in Combustion and Heat Transfer Modelling in Rocket Thrust Chamber Applied Engineering. In *Proceedings of the 45th AIAA/SAE/ASEE Joint Propulsion Conference*, Denver, CO, United States of America, 2009.

[34] L. Selle, R. Blouquin, M. Theron, and L.-H. Dorey. Prediction and Analysis of Combustion Instabilities in a Model Rocket Engine. *Journal of Propulsion and Power*, 30(4):978–990, 2014.

[35] A. Chemnitz and T. Sattelmayer. Calculation of the Thermoacoustic Stability of a Main Stage Thrust Chamber Demonstrator. *Notes on Numerical Fluid Mechanics and Multidisciplinary Design*, 146:235–247, 2021.

[36] M. Seidl, R. Keller, P. Gerlinger, and M. Aigner. Numerical Simulations of Rocket Combustion Chambers with Supercritical Injection. *High Performance Computing in Science and Engineering '16*, pages 259–268, 2017.

[37] A. Chemnitz, N. Kings, and T. Sattelmayer. Modification of eigenmodes in a cold-flow rocket combustion chamber by acoustic resonators. *Journal of Propulsion and Power*, 35(4):765–779, 2019.

[38] ANSYS Inc. *ANSYS Fluent User's Guide - Release 15.0*. ANSYS Inc., 2013.

[39] O. Knab, H. Riedmann, B. Ivancic, C. Höglauer, M. Frey, and T. Aichner. Consequences of Modeling Demands on Numerical Rocket Thrust Chamber Flow Simulation Tools. In *Proceedings of the 6th EUCASS*, Krakow, Poland, 2015.

[40] G.P. Sutton and O. Biblarz. *Rocket Propulsion Elements*. John Wiley & Sons, Hoboken, New Jersey, United States of America, 2010.

[41] D.K. Huzel and D.H. Huang. *Modern Engineering for Design of Liquid-Propellant Rocket Engines*. American Institute of Aeronautics & Astronautics, Washington, DC, United States of America, 1992.

[42] O.J. Haidn. Advanced Rocket Engines. In *Advances in Propulsion Technology for High-Speed Aircraft*, Sint-Genesius-Rode, Belgium, 2007.

[43] G. Hagemann and O. Knab. *Lecture Notes - Raumfahrtantriebe 1*. Lecture Series - Technical University of Munich, 2012.

[44] R. Stark. Flow Separation in Rocket Nozzles, a Simple Criteria. In *Proceedings of the 41st AIAA/ASME/SAE/ASEE Joint Propulsion Conference & Exhibit*, Tucson, AZ, United States of America, 2005.

[45] G. Hagemann and O. Knab. *Lecture Notes - Raumfahrtantriebe 2*. Lecture Series - Technical University of Munich, 2012.

[46] H. Riedmann. *Ein Verfahren zur Sprayverbrennungs- und Wärmeübergangssimulation in Raketenschubkammern in 3D*. Dissertation - University of Stuttgart, 2015.

[47] S. Silvestri. *Investigation on Heat Transfer and Injector Design Criteria for Methane/Oxygen Rocket Combustion Chambers*. Dissertation - Technical University of Munich, 2019.

[48] J.H. Ferziger and M. Peric. *Computational Methods for Fluid Dynamics*. Springer-Verlag, Berlin/Heidelberg, Germany, 2002.

[49] T. Poinsot and D. Veynante. *Theoretical and Numerical Combustion*. R.T. Edwards, Flourtown, PA, United States of America, 2005.

[50] P. Gerlinger. *Numerische Verbrennungssimulation*. Springer-Verlag, Berlin/Heidelberg, Germany, 2005.

[51] W.C. Jr. Gardiner and A. Burcat. *Combustion Chemistry*. Springer-Verlag, Berlin/Heidelberg, Germany, 1984.

[52] R.B. Bird, W.E. Stewart, and E.N. Lightfoot. *Transport Phenomena*. John Wiley & Sons, Hoboken, New Jersey, United States of America, 2006.

[53] B. Eisfeld. *Lecture Notes - RANS Turbulence Modelling*. Lecture Series - Deutsches Zentrum für Luft- und Raumfahrt e.V., 2008.

[54] J. Boussinesq. *Essai sur la theorie des eaux courantess.* Memoires presentes par divers savants a l'Academie des Sciences de l'Institut National de France, Paris, 1877.

[55] H.K. Versteeg and W. Malalasekera. *An Introduction to Computational Fluid Dynamics: The Finite Volume Method.* Pearson Education, London, United Kingdom, 2007.

[56] W.M. Kays. Turbulent Prandtl Number - Where Are We? *Journal of Heat Transfer*, 116(2):284–295, 1994.

[57] U.C. Goldberg, S. Palaniswamy, P. Batten, and V. Gupta. Variable Turbulent Schmidt and Prandtl Number Modeling. *Engineering Applications of Computational Fluid Mechanics*, 4(4):511–520, 2010.

[58] P. Keistler. *A Variable Turbulent Prandtl and Schmidt Number Model Study for Scramjet Applications.* Dissertation - North Carolina State University, 2009.

[59] S.B. Pope. *Turbulent Flows.* Cambridge University Press, Cambridge, United Kingdom, 2000.

[60] W.P. Jones and B.E. Launder. The Prediction of Laminarization with a Two-Equation Model of Turbulence. *International Journal of Heat and Mass Transfer*, 15(2):301–314, 1972.

[61] B.E. Launder and B.I. Sharma. Application of the Energy Dissipation Model of Turbulence to the Calculation of Flow Near a Spinning Disc. *Letters in Heat and Mass Transfer*, 1(2):131–138, 1974.

[62] M. Wolfshtein. The velocity and temperature distribution in one-dimensional flow with turbulence augmentation and pressure gradient. *International Journal of Heat and Mass Transfer*, 12(3):301–318, 1969.

[63] ANSYS Inc. *ANSYS Fluent Theory Guide - Release 15.0.* AN-SYS Inc., 2013.

[64] K. Abe, T. Kondoh, and Y. Nagano. A new turbulence model for predicting fluid flow and heat transfer in separating and reattaching flows-I. Flow field calculations. *International Journal of Heat and Mass Transfer*, 37(1):139–151, 1994.

[65] C.R. Yap. *Turbulent heat and momentum transfer in recirculating and impinging flows.* Dissertation - University of Manchester Institute of Science and Technology, 1987.

[66] B.E. Launder. Modelling Convective Heat Transfer in Complex Turbulent Flows. In *Proceedings of the 2nd International Symposium on Engineering Turbulence Modelling and Measurements*, Florence, Italy, 1993.

[67] D.C. Wilcox. Re-assessment of the scale-determining equation for advanced turbulence models. *International Journal of Heat and Mass Transfer*, 26(11):1299–1310, 1988.

[68] D.C. Wilcox. *Turbulence Modeling for CFD.* D C W Industries, La Canada, CA, United States of America, 2006.

[69] F.R. Menter. Zonal Two Equation k-ω Turbulence Models for Aerodynamic Flows. In *Proceedings of the 23rd Fluid Dynamics, Plasmadynamics, and Lasers Conference*, Orlando, FL, United States of America, 1993.

[70] F.R. Menter. Two-Equation Eddy-Viscosity Turbulence Models for Engineering Applications. *AIAA Journal*, 32(8):1598–1605, 1994.

[71] B. Ivancic, M. Frey, and O. Knab. 3D-numerical investigation of turbulent combustion and heat transfer processes in H2-O2

liquid rocket combustors. In *Proceedings of the Space Propulsion Conference*, San Sebastian, Spain, 2010.

[72] B. Ivancic, H. Riedmann, and M. Frey. Validation of Turbulent Combustion Models for 3D-Simulations of Liquid H_2/O_2 Rocket Combustors. In *Proceedings of the Space Propulsion Conference*, Bordeaux, France, 2012.

[73] N. Perakis, C. Roth, and O.J. Haidn. Development of a non-adiabatic Flamelet model for reacting flows with heat loss. In *Proceedings of the Space Propulsion 2018*, Seville, Spain, 2018.

[74] N. Peters. Laminar diffusion flamelet models in non-premixed turbulent combustion. *Progress in Energy and Combustion Science*, 10(3):319–339, 1984.

[75] N. Peters. Laminar flamelet concepts in turbulent combustion. *Twenty-first Symposium (International) on Combustion*, 21(1):1231–1250, 1988.

[76] D. Lee, S. Thakur, J. Wright, M. Ihme, and W. Shyy. Characterization of Flow Field Structure and Species Composition in a Shear Coaxial Rocket GH2/GO2 Injector: Modeling of Wall Heat Losses. In *Proceedings of the 47th AIAA/ASME/SAE/ASEE Joint Propulsion Conference & Exhibit*, San Diego, CA, United States of America, 2011.

[77] F. Proch and A.M. Kempf. Modeling heat loss effects in the large eddy simulation of a model gas turbine combustor with premixed flamelet generated manifolds. *Proceedings of the Combustion Institute*, 35(3):3337–3345, 2015.

[78] H. Wu and M. Ihme. Modeling of Wall Heat Transfer and Flame/Wall Interaction: A Flamelet Model with Heat-Loss Ef-

fects. In *Proceedings of the 9th U.S. National Combustion Meeting*, Cincinnati, OH, United States of America, 2015.

[79] G. Frank, J. Zips, and M. Pfitzner. Construction of Libraries for Non-Premixed Tabulated Chemistry Combustion Models including Non-Adiabatic Behaviour due to Wall Heat Losses. In *Annual Report SFB/TRR 40*, Munich, Germany, 2016.

[80] N. Perakis, C. Roth, and O.J. Haidn. Simulation of a single-element rocket combustor using a non-adiabatic Flamelet model. In *Proceedings of the Space Propulsion 2018*, Seville, Spain, 2018.

[81] W.H. Press, S. Teukolsky, B.P. Flannery, and W.T. Vetterling. *Numerical Recipes in C: The Art of Scientific Computing*. Cambridge University Press, Cambridge, United Kingdom, 1992.

[82] S. Gordon and B.J. McBride. *Computer Program for Calculation of Complex Chemical Equilibrium Compositions and Applications I. Analysis (NASA RP-1311)*. NASA, 1994.

[83] B.J. McBride and S. Gordon. *Computer Program for Calculation of Complex Chemical Equilibrium Compositions and Applications II. User Manual and Program Description (NASA RP-1311)*. NASA, 1996.

[84] S. Kim, H. Choi, and Y. Kim. Thermodynamic modeling based on a generalized cubic equation of state for kerosene/LOx rocket combustion. *Combustion and Flame*, 159(3):1351–1365, 2012.

[85] D.G. Goodwin, R.L. Speth L. Raymond, H.K. Moffat, and B.W. Weber. *Cantera: An Object-oriented Software Toolkit for Chemical Kinetics, Thermodynamics, and Transport Processes*. Zenodo, Online Source, 2018.

[86] R. Sankaran, E.R. Hawkes, J.H. Chen, T.F. Lu, and C.K. Law. Structure of a spatially developing turbulent lean methane-air Bunsen flame. *Proceedings of the Combustion Institute*, 31(1):1291–1298, 2007.

[87] B.J. McBride, S. Gordon, and M.A. Reno. *Coefficients for Calculating Thermodynamic and Transport Properties of Individual Species (TM-4513)*. NASA, 1993.

[88] D. R. Stull and H. Prophet. *JANAF Thermochemical Tables, Second Edition (NSRDS-NBS 37)*. NIST, 1971.

[89] B.J. McBride, M.J. Zehe, and S. Gordon. *NASA Glenn Coefficients for Calculating Thermodynamic Properties of Individual Species (NASA/TP-2002-211556)*. NASA, 2002.

[90] C.R. Wilke. A Viscosity Equation for Gas Mixtures. *The Journal of Chemical Physics*, 18(4):517–519, 1950.

[91] A. Eucken. On the thermal conductivity, the specific heat and the viscosity of gases. *Physikalische Zeitschrift*, 14(4):324–333, 1913.

[92] S. Silvestri, M.P. Celano, C. Kirchberger, G. Schlieben, O. Haidn, and O. Knab. Investigation on Recess Variation of a Shear Coax Injector for a Single Element GOX-GCH4 Combustion Chamber. volume 14, pages Pa_13–Pa_20, 2016.

[93] M. P. Celano, S. Silvestri, J. Pauw, N. Perakis, F. Schily, D. Suslov, and O. J. Haidn. Heat flux evaluation methods for a single element heat sink chamber. In *Proceedings of the 6th European Conference for Aeronautics and Space Sciences*, Krakow, Poland, 2015.

[94] N. Perakis, M.P. Celano, and O.J. Haidn. Heat flux and temperature evaluation in a rectangular multi-element GOX/GCH4 combustion chamber using an inverse heat conduction method. In *Proceedings of the 7th European Conference for Aeronautics and Space Sciences*, Milan, Italy, 2017.

[95] N. Perakis and O.J. Haidn. Inverse heat transfer method applied to capacitively cooled rocket thrust chambers. *International Journal of Heat and Mass Transfer*, 131:150–166, 2019.

[96] L. Vingert, A. Nicole, and M. Habiballah. The Mascotte single injector 60 bar hot test for code validation. In *Proceedings of the 3rd International Workshop on Rocket Combustion Modeling*, Vernon, France, 2006.

[97] D. Suslov. *Lecture Notes - Heat Transfer in Rocket Engines*. Lecture Series - Technical University of Munich, 2014.

[98] JANNAF Working Group. *JANNAF Rocket Engine Performance Prediction and Evaluation Manual*. Chemical Propulsion Information Agency, Johns Hopkins University, 1975.

[99] P.J. Roache. Perspective: A Method for Uniform Reporting of Grid Refinement Studies. *Journal of Fluids Engineering*, 116(3):405–413, 1994.

[100] L.F. Richardson. The Approximate Arithmetical Solution by Finite Differences of Physical Problems Involving Differential Equations, with an Application to the Stresses in a Masonry Dam. *Transaction Proceedings of the Royal Society of London. Series A*, 210:307–357, 1910.

[101] H. Wang. *Lecture Notes - Combustion Chemistry*. Lecture Series - 2012 Princeton-CEFRC Summer School On Combustion, 2012.

[102] Combustion Research Group, UC San Diego. The San Diego Mechanism. http://web.eng.ucsd.edu/mae/groups/combustion/ mechanism.html, 2016.

[103] Tianfeng Lu, University of Connecticut. A 13-species reduced mechanism and a 17-species skeletal mechanism for lean methane-air (flame speed only) based on GRI-Mech 1.2. http://spark.engr.uconn.edu/mechs/mechs.htm, 2007.

A Thermodynamic Property Data

The polynomial fits of the thermodynamic property data for each species at the ideal reference-state are shown in Figures A.1 to A.6. The source for the reference data is indicated in the plot legend. The sources are:

- SD: *The San Diego Mechanism* [102].

- Lu: *Tianfeng Lu* [103].

In the low temperature range the source data for the specific heat capacity c_p is extrapolated based on a C^2 continuous cubic spline interpolation of the values at neighboring grid points. In the high temperature range linear extrapolation is used. Extrapolation of the enthalpy h and entropy s is performed according to the following relations:

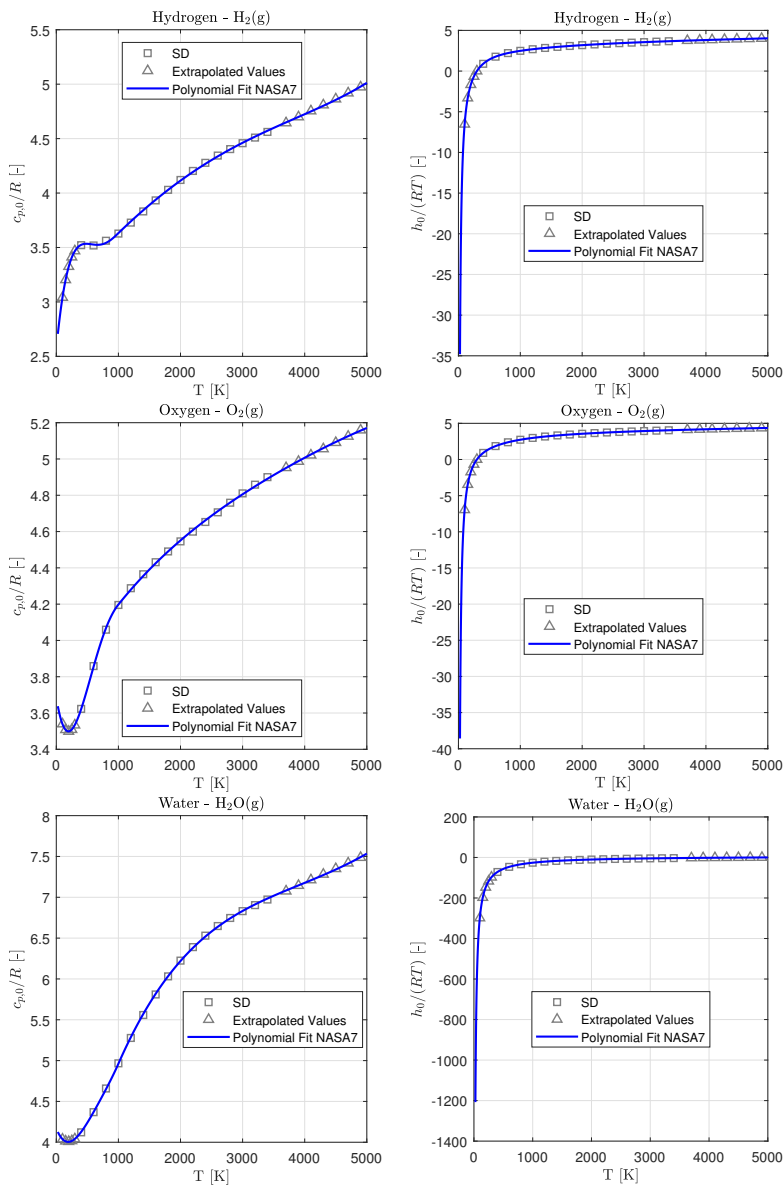$$dh = c_p dT \tag{A.1}$$

$$ds = \frac{c_p}{T} dT \tag{A.2}$$

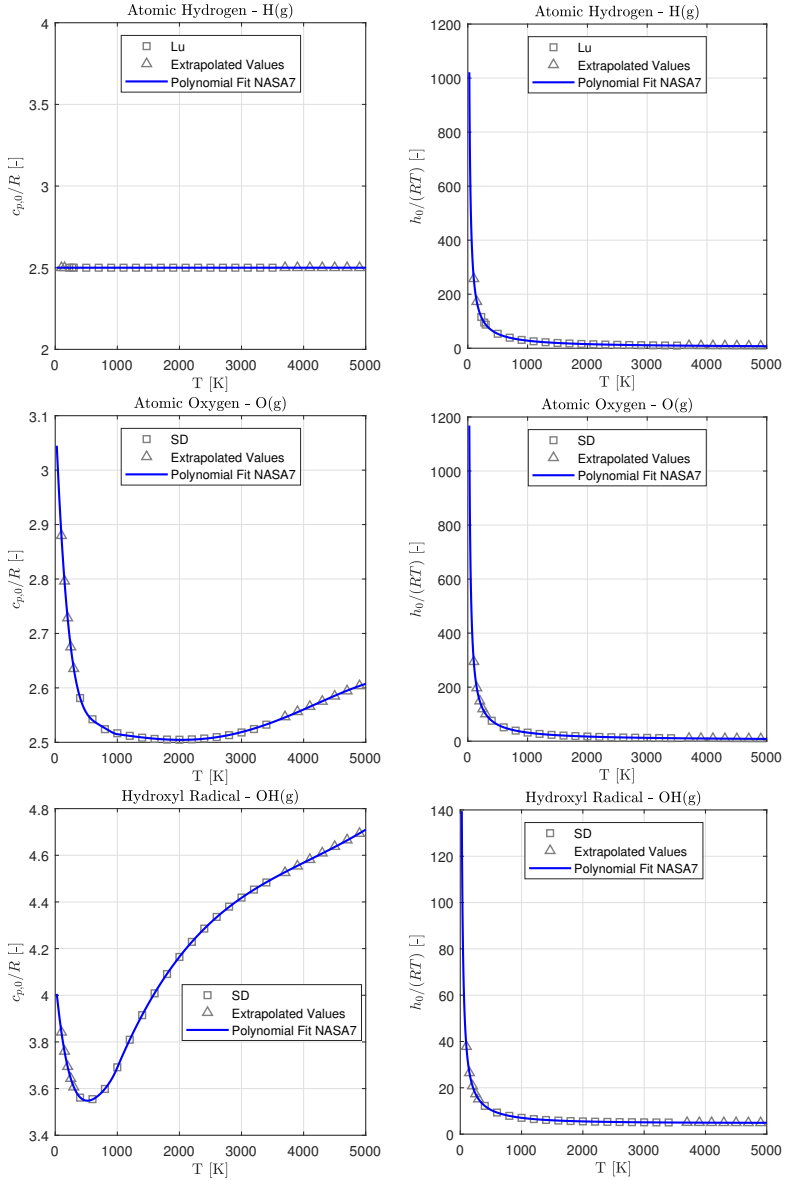**Figure A.1:** Thermodynamic property fits and reference data #1.

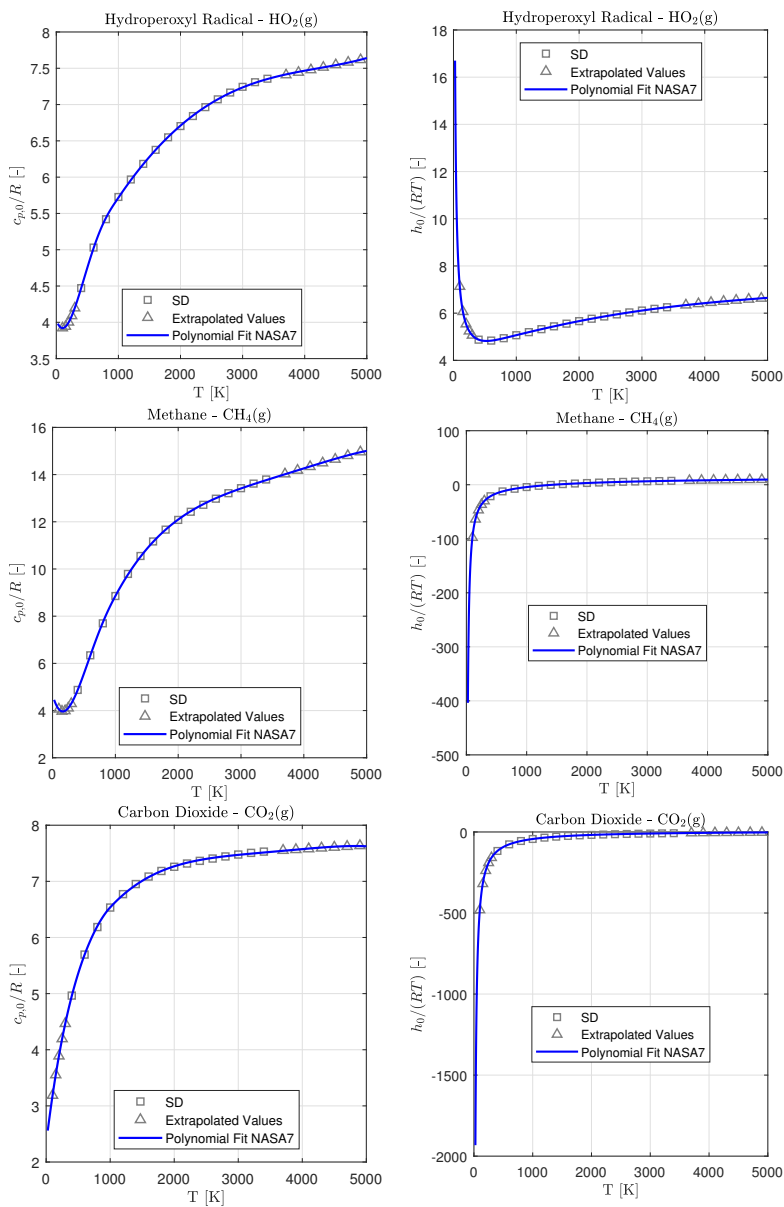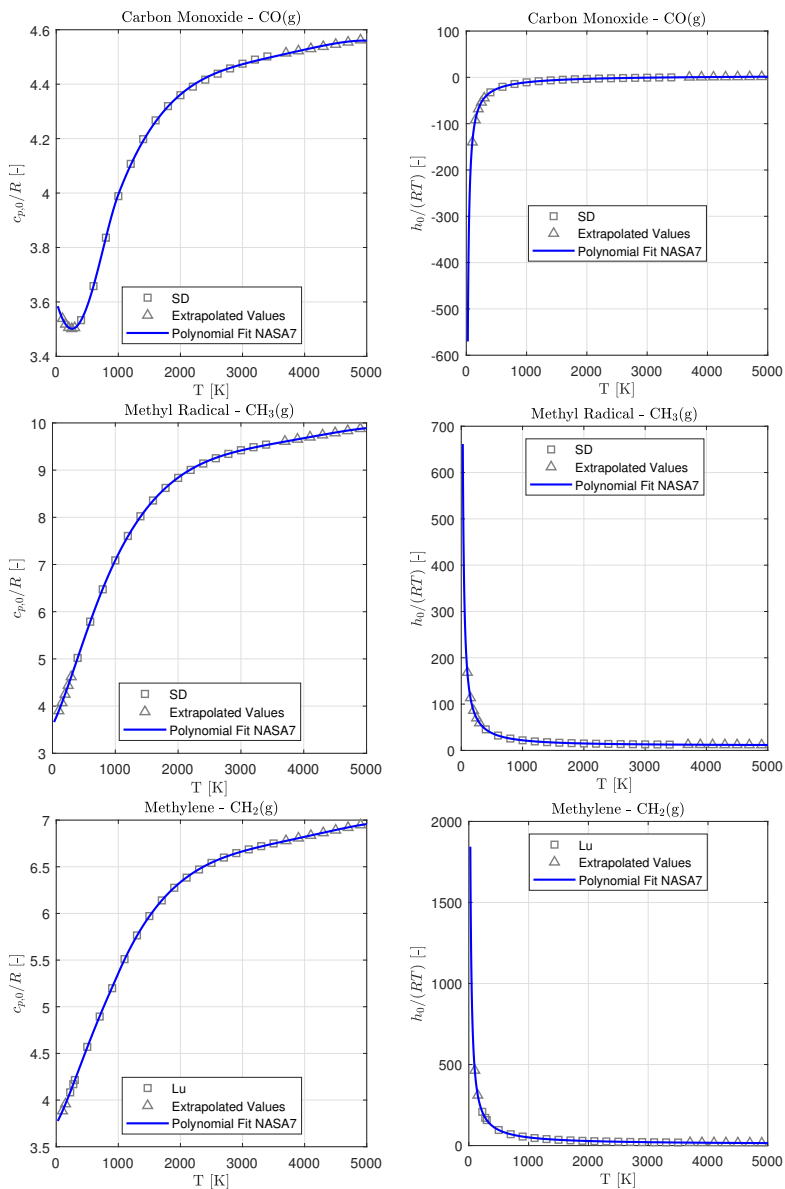**Figure A.2:** Thermodynamic property fits and reference data #2.

Figure A.3: Thermodynamic property fits and reference data #3.

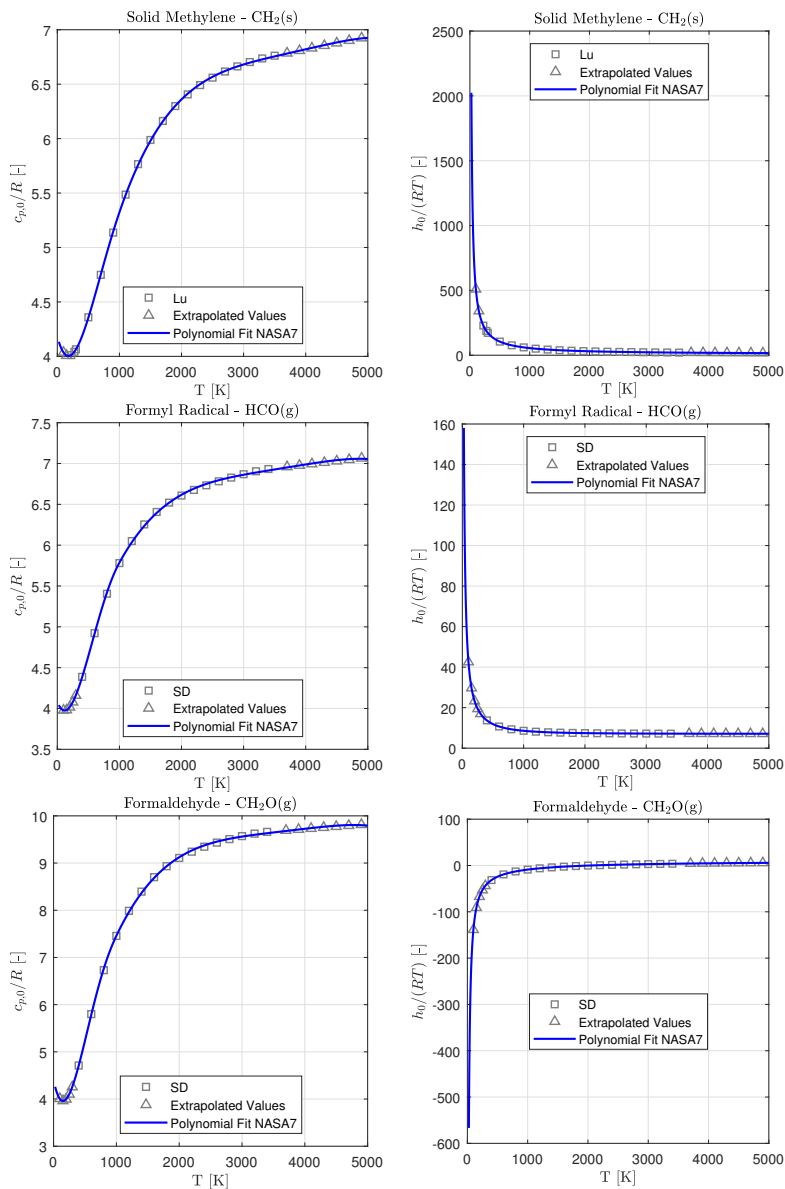**Figure A.4:** Thermodynamic property fits and reference data #4.

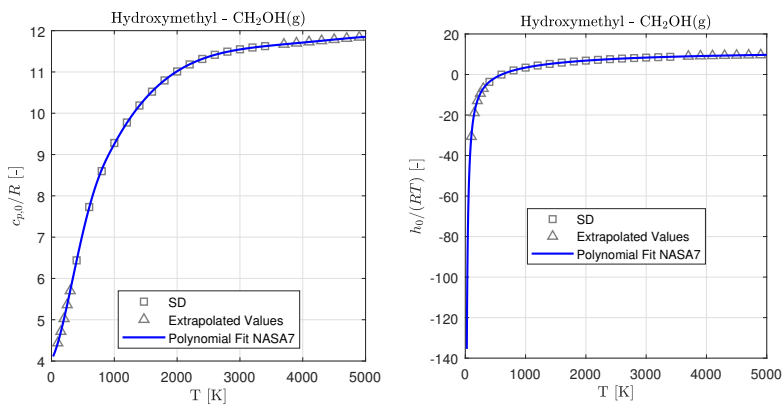**Figure A.5:** Thermodynamic property fits and reference data #5.

Figure A.6: Thermodynamic property fits and reference data #6.

B Transport Property Data

Table B.1: Transport Property Data.

Species	Geometry[1]	$\varepsilon/k_b^{2)}$	$\sigma^{3)}$	$\mu^{4)}$	$\alpha^{5)}$	$Z_{rot}^{6)}$
H2	1	38.0	2.920	0.000	0.79	280.0
O2	1	107.4	3.458	0.000	1.60	3.8
H2O	2	572.4	2.605	1.855	0.00	4.0
H	0	145.0	2.050	0.000	0.00	0.0
O	0	80.0	2.750	0.000	0.00	0.0
OH	1	80.0	2.750	0.000	0.00	0.0
HO2	2	107.4	3.458	0.000	0.00	1.0
CH4	2	141.4	3.746	0.000	2.60	13.0
CO2	1	244.0	3.763	0.000	2.65	2.1
CO	1	98.1	3.650	0.000	1.95	1.8
CH3	1	144.0	3.800	0.000	0.00	0.0
CH2	1	144.0	3.800	0.000	0.00	0.0
CH2(s)	1	144.0	3.800	0.000	0.00	0.0
HCO	2	498.0	3.590	0.000	0.00	0.0
CH2O	2	498.0	3.590	0.000	0.00	2.0
CH2OH	2	417.0	3.690	1.700	0.00	2.0

1) An integer with value 0, 1, or 2 indicating monatomic, linear, or non-linear molecular geometry.

2) The Lennard-Jones potential well depth ε/k_b in Kelvin.

3) The Lennard-Jones collision diameter σ in Angstrom.

4) The dipole moment μ in Debye.

5) The polarizability α in Angstrom.

6) The rotational relaxation collision number Z_{rot} at 298 K.